PhD-FSTM-2024-046

The Faculty of Science, Technology and Medicine

DISSERTATION

Defence held on 10/06/2024 in Luxembourg

to obtain the degree of

DOCTEUR DE L'UNIVERSITÉ DU LUXEMBOURG
EN INFORMATIQUE

by

Ahmed Abdelnaser Elsayed Murtada

Born on 09 October 1990 in Medina (Saudi Arabia)

Radar Distributed Sensors for Indoor Imaging

Dissertation Defence Committee:

Prof. Dr. Bhavani Shankar Mysore Rama Rao, Dissertation Supervisor
Assistant Professor, SnT, University of Luxembourg

Prof. Dr. Djamila Aouada, Chair
Assistant Professor, SnT, University of Luxembourg

Dr. Mohammad Alaee-Kerahroodi, Vice-Chair
Research Scientist, SnT, University of Luxembourg

Dr. Udo Schröder
Research Scientist, IEE S.A., Luxembourg

Prof. Dr. Andreas Diewald
Full Professor, Trier University of Applied Sciences, Germany

Abstract

Millimeter-wave (mmWave) radar sensors have emerged as critical monitoring devices in various indoor applications, owing to their resilience to environmental conditions, non-intrusiveness, and cost-effectiveness. This thesis presents advancements in radar signal processing techniques tailored for indoor scenarios, with a focus on enhancing two radar output representations of a scene observed by distributed sensors: spatial reflectivity images and detection point clouds.

The thesis is divided into two parts, in the first part, it addresses challenges associated with generating high-quality reflectivity images from the reflected signals measured by widely distributed radar sensors. Leveraging compressed sensing methods, novel algorithms based on the Alternating Direction Method of Multipliers (ADMM) optimization framework are proposed to reconstruct global reflectivity images. Additionally, a heuristic method to accelerate the convergence of the proposed algorithms and reduce their computational complexity is introduced. Moreover, an efficient implementation of sparsity-based image reconstruction algorithms is proposed, achieved through automatic tuning of the regularization parameters while also considering synchronization errors.

The second part is devoted to the design of statistical detectors for mmWave radar sensors, focusing on detecting aspect-dependent targets and leveraging occlusion modeling in hypothesis testing formulations. Novel formulations are proposed, leading to 1) a detector with optimum weights on the processed signals of distributed sensors to jointly and efficiently detect aspect-dependent targets and 2) a detector based on occlusion modeling which enhances detection performance at each sensor node by leveraging the sparse structure of range profiles due to occlusions. Through scenario-based simulations and model-based evaluations, the proposed detectors demonstrate improved accuracy in detecting aspect-dependent and non-occluded targets, thereby providing accurate high-resolution point clouds.

The algorithms presented in this thesis provide an enhancement of the quality of radar images aiming to facilitate the subsequent analysis using classical image processing or advanced deep-learning techniques in various indoor applications.

Acknowledgements

The successful completion of this thesis results from the invaluable support of many individuals. I express my heartfelt gratitude to all those who have walked alongside me on this journey, offering guidance, assistance, and encouragement.

First and foremost, I would like to express my sincere gratitude to my supervisor Bhavani Shankar, whose guidance has been not only attuned and empathetic but also notably tolerant. He has a remarkable ability to discern the traits of each individual and tailor his guidance accordingly. I am particularly grateful for his trust in granting me the liberty to explore various research avenues while maintaining a delicate balance of restrictions and freedom. This has allowed me to reinforce my knowledge and confidence in different topics related to my work, all while ensuring alignment with the thesis objectives.

I would also like to extend my thanks to Udo Schröder from our industrial partner, IEE. As an industrial advisor for my thesis, he spared no effort in facilitating my visits to IEE and providing all the necessary support for the experiments conducted on their premises, which inspired the work done in the second part of this thesis. Additionally, and more importantly, our regular meetings gave me valuable insights that shaped the practical aspect of my research.

Besides, I would like to express my appreciation to Mohammad Alaee-Kerahroodi. Apart from being a member of my supervision committee and offering invaluable expertise throughout the realization of this thesis, he was always approachable whenever I had doubts or questions. His in-depth knowledge of the different components of radar systems enabled him to consistently provide answers that alleviated my confusion.

At the beginning of my PhD, I had the opportunity to work closely with Ruizhi Hu on radar image reconstruction algorithms. I thank him for his support and assistance; his background and experience in the topic were instrumental in the smooth start of my research journey and equipped me with the knowledge and tools necessary to carry out the work conducted in the first part of this thesis. I also thank Moein Ahmadi for his suggestions and collaboration in the second part of the thesis. Thanks to his strong

expertise in radar detection, he was my go-to resource not only for related theoretical discussions but also for practical implications.

I extend my gratitude to my friends and colleagues from the SPARC group. Our discussions, coffee breaks, and lunches together made the difficult times more bearable. I would like to particularly thank Thomas Feuillen for his exceptional assistance, especially in the final stages of completing this work. As a supportive colleague and close friend, his constructive feedback, insightful suggestions, and unwavering encouragement were invaluable in reaching the finish line.

Throughout my PhD journey at SnT, I have made many friends—so many that I could fill at least half a page with their names. Each of them has been there to uplift me during challenging times and to celebrate achievements. I thank all of them for making my PhD time colorful and filled with unforgettable memories.

Finally, my deep gratitude and appreciation go to my wife, Shaimaa, for her constant support, patience, and tolerance during the many late nights, without her the completion of this work would not have been possible.

Preface

Support

This research was funded by the Luxembourg National Research Fund (FNR), under the FNR Industrial Fellowship Grant, grant reference [IF/15364040/RADII].

Collaboration

This work was made possible thanks to the collaboration with the industrial partner IEE S.A.

"Curiosity – the rover and the concept – is what science is all about: the quest to reveal the unknown."

Ahmed Zewail

Contents

Abstract **iii**

Acknowledgements **v**

List of Figures **xvi**

List of Tables **xvii**

Acronyms **xxii**

1 Introduction **1**

1.1 Radar Images 2

1.1.1 Radar Signal Processing Chain 4

1.1.2 Which Radar Image? 6

1.1.3 Radar Images Analysis 6

1.2 Motivation 7

1.3 Widely Distributed Radars 8

1.3.1 Challenges With Distributed Radars 9

1.4 Contributions 11

1.4.1 Thesis Organization 12

1.4.2 List of Publications 13

I Reflectivity Image Formation **17**

2 Distributed Imaging via ADMM **19**

2.1 Introduction 19

2.2 Signal Model and Background 22

2.2.1 Tomography Inspired Modeling 23

2.2.2 Distributed Radar Imaging Model 24

2.2.3 State-of-the-art Problem Formulation . . . 25
2.3 ADMM Framework for Distributed Radar Imaging . . . 26
2.3.1 Consensus ADMM (CADMM) . . . 28
2.3.2 Sharing ADMM (SADMM) . . . 30
2.3.3 Solution Techniques . . . 32
2.4 Performance Evaluation . . . 35
2.4.1 Data-Set Introduction . . . 35
2.4.2 Performance Metrics . . . 37
2.4.3 Experiments . . . 38
2.5 Conclusion . . . 49

3 Imaging Acceleration **51**
3.1 Introduction . . . 51
3.2 Signal Model . . . 52
3.3 Problem Formulation . . . 53
3.4 Accelerated ADMM Imaging . . . 54
3.4.1 Accelerated Consensus ADMM . . . 55
3.4.2 Accelerated Sharing ADMM . . . 58
3.4.3 Solution Techniques . . . 59
3.5 Numerical Results . . . 61
3.6 Conclusion . . . 63

4 Automatic Hyperparameters Tuning **67**
4.1 Introduction . . . 67
4.2 System Model . . . 69
4.3 Image Recovery . . . 72
4.3.1 Solution Model . . . 72
4.3.2 FISTA Parameters Auto-selection . . . 72
4.3.3 Reduced Complexity Implementation . . . 75
4.4 Numerical Analysis . . . 77
4.5 Conclusion . . . 80

II Point Clouds Detection **81**

5 Distributed Detection of Aspect-Dependent Targets **83**
5.1 Introduction . . . 83
5.2 System and Signal Model . . . 85

5.3 GLRT Detector Derivation 86
5.4 Numerical Analysis 89
5.5 Conclusion 93

6 Occlusion-Informed Detection **95**
6.1 Introduction 95
6.2 System Model 100
6.3 Occlusion-Informed Detector Design 102
6.3.1 Multiple Hypothesis Testing Design 102
6.3.2 Binary Hypothesis Testing Design 104
6.4 Numerical Analysis 108
6.4.1 Model-based ROC Assessment 108
6.4.2 Scenario-based Simulations 114
6.5 Conclusion 120

7 Conclusion **123**
7.1 Summary of Contributions 123
7.2 Future Work 126

Bibliography **129**

List of Figures

1.1 **Left:** An example of a SAR reflectivity image (displayed on the laptop screen) formed by a single radar sensor mounted on a moving robotic arm, **Right:** a picture of the targets imaged by the sensor. 3

1.2 Radar images in a dynamic scenario: (a) Layout of the measurement area, (b) Snapshot of the scenario with two walking humans and the sensor mounted on the wall, (c) Associated range-Doppler map, (d) Associated range-azimuth map. 3

1.3 Simulated indoor scenario: (a) Ground truth, (b) Point clouds detection image. 3

1.4 Basic radar signal processing blocks and the associated output images: (a) Range-Doppler, (b) Range-angle, (c) Reflectivity image, (d) Point clouds. 4

1.5 Detection outputs from three widely distributed sensors, highlighting the advantage of observing targets over wide angles. (Figure courtesy of Moein Ahmadi) 9

1.6 High-level radar signal processing block with an illustration of the possible schemes for fusing the signals from multiple sensors. 10

1.7 Thesis outline and the corresponding publications linked to each chapter 14

2.1 Geometry of Distributed Radar System 23

2.2 Illustration of the parallel implementation scheme of CADMM and SADMM. 35

2.3 Hyperparameters sweep for 'Jeep99' data (FVFB): **Top row:** Normalized sparsity, **Bottom row:** Image entropy. 38

2.4 Jeep image reconstruction at different sparsity levels: **Left column:** 12%, **Right column:** 5%. 41

2.5 FVFB image reconstruction at sparsity level $\approx 10\%$, $Q = 72$ clusters, bandwidth = 5.35 GHz: **Left column:** Jeep Cherokee, **Right column:** Toyota Tacoma. 42

2.6 FVLB image reconstruction at sparsity level $\approx 10\%$, $Q = 72$ clusters, bandwidth = 600 MHz: **Left column:** Jeep Cherokee, **Right column:** Toyota Tacoma. 43
2.7 Low sparsity FVLB reconstruction of Toyota Tacoma (sparsity level $\approx 15\%$). 44
2.8 LVLB image reconstruction at sparsity level $\approx 10\%$, $Q = 16$ clusters, bandwidth = 600 MHz: **Left column:** Jeep Cherokee, **Right column:** Toyota Tacoma. 46
2.9 LVLB reconstruction with different random sensors orientation: **Left column:** Jeep Cherokee, **Right column:** Toyota Tacoma. 47
2.10 LS-CS-Residual imaging results for 'Jeep99' data for the three experiments: **Left:** FVFB, **Middle:** FVLB, **Right:** LVLB. 48

3.1 Targets Radar Cross Section (RCS) vs. Aspect angle 62
3.2 Sensors orientation and their ground truth images 63
3.3 Composite ground truth image and reconstructed images with a 30 dB dynamic range using BP, CADMM, and ACADMM 64
3.4 Composite ground truth image and reconstructed images with a 30 dB dynamic range using BP, SADMM, and ASADMM 65
3.5 CADMM and ACADMM Convergence Rate 66
3.6 SADMM and ASADMM Convergence Rate 66

4.1 (a) Scenario layout; (b) Reflectivity ground-truth 77
4.2 Image reconstruction by (a) Adjoint matrix, (b) FISTA with auto-selected parameters $\hat{\lambda}$, (c) and (d) FISTA with mismatched parameters $2\hat{\lambda}$ and $\hat{\lambda}/2$, respctively. 78
4.3 ROC curves for image reconstruction using our calculated $\hat{\lambda}$ versus $1.5\hat{\lambda}$ and $\hat{\lambda}/2$ at different PSNR levels. The maximum mismatch error T_{max} is equivalent to 5 samples (Top row) and 25 samples (Bottom row). 79

5.1 ROC curves for the proposed GLRT detector compared with conventional and optimum LRT detectors where $Q = 4$, $M = 3Q$, $\text{SNR}_{post} = 13$ dB for a fluctuating target with **Top:** isotropic RCS, **Middle:** Aspect-dependent RCS with maximum variation 10 dB, **Bottom:** Aspect-dependent RCS with maximum variation 20 dB. 90
5.2 ROC curves of the proposed GLRT detector versus the number of distributed sensors, $\text{SNR}_{post} = 13$ dB, $M = 3Q$. 91

5.3 ROC curves of the proposed GLRT detector versus different values of post-processing SNR, $Q = 4$, $M = 3Q$ 92

5.4 ROC curves of the proposed GLRT detector versus the number of integrated chirps, $\text{SNR}_{post} = 13$ dB, $Q = 4$ 93

6.1 2D Range-Azimuth grid map illustrating the sparsity of range profiles relative to targets' size in an occlusion-prone sensing environment. Two targets in the scene, with one occluding part of the other, are observed by two sensors with different angular resolutions, depicted by the corresponding angular grid sizes. **Left:** Sensor with low angular resolution ($\delta\theta_1$) relative to targets' size. **Right:** Sensor with high angular resolution ($\delta\theta_2 = 0.5\ \delta\theta_1$) relative to targets' size. 97

6.2 3D Demonstration of a full occlusion scenario over a range profile in an indoor environment observed with a mmWave sensor featuring high angular resolution. **Left:** Layout of the scene with the detection grid showing the sensor's view and highlighted group of mutually occluding cells. **Middle:** Corresponding radar cube. **Right:** Expected and actual signal returns in the group of highlighted cells. 98

6.3 Illustration of signal generation in all cells under null and alternative hypotheses for a certain CUT n (highlighted with the red rectangle) given a probability model in the target space for $N = 32$, $n = 23$, $K_{MC} = 10^3$. (a) Probabilities of targets presence P_k, (b) Probabilities of receiving a signal return (marginal ρ_k, and conditioned on no return in CUT $\rho_{k|\tilde{n}}$), (c) Monte-Carlo realizations of signal return events under $\mathcal{H}_0^{(n)}$, (d) Monte-Carlo realizations of signal return events under $\mathcal{H}_1^{(n)}$. 109

6.4 ROC curves of proposed detectors compared against classic detector for $N = 128$ cells and SNR = 10 dB, for different models of the probability of targets arrival in resolution cells and different values of maximum probability of target presence p_{max} at cells. **Left column:** equal probability, **Middle column:** linearly increasing, **Right column:** linearly decreasing. **Top row:** $p_{max} = 0.1$, **Middle row:** $p_{max} = 0.5$, **Bottom row:** $p_{max} = 0.9$ 110

6.5 ROC curves of proposed ML occlusion-informed detectors compared to classic detector varying the number of mutually occluding cells $N = 16, 32, 64, 128$ (the arrows indicate the direction of increasing N) at different SNR levels. **Top:** 8 dB, **Middle:** 10 dB, **Bottom:** 13 dB. 112

6.6 ROC curves of proposed ML occlusion-informed detectors compared to classic detector varying SNR at different numbers of mutually occluding cells. **Top:** $N = 32$, **Middle:** $N = 64$, **Bottom:** $N = 128$. 113
6.7 Simulation scenario and modeling: (a) Configuration of 121×121 TX-RX antennas for the radar sensor, (b) Snapshot of a single time frame of the scenario depicting human targets modeled using triangle batches, highlighting the origin points of triangle batches with LOS, (c) Close-up view of a single human object. 114
6.8 Single time frame snapshot of point cloud detection. **Top:** Classic detector output, **Middle:** Max-ML detector output, **Bottom:** Occ-ML detector output. 118
6.9 Detection performance versus time frames. **Top:** False alarms rate. **Bottom:** Detection rate. 119

List of Tables

2.1 Summary of parameters used in the experiments and corresponding metrics 48
2.2 Relative convergence and complexity 49
2.3 Absolute computing times using proposed methods vs. LS-CS-Residual for 'Jeep99' (in minutes) 49

6.1 FMCW Radar System Parameters 116
6.2 Radar Signal Processing and Detection Parameters 117

Acronyms

A | **B** | **C** | **D** | **F** | **G** | **H** | **I** | **K** | **L** | **M** | **N** | **P** | **R** | **S** | **T** | **U** | **W**

A

ACADMM Accelerated CADMM

ADC Analog to Digital Converter

ADMM Alternating Direction Method of Multipliers

APCs Antenna Phase Centers

ASADMM Accelerated SADMM

ATR Automatic Target Recognition

B

BP Back Projection

C

CA Cell Averaging

CADMM Consensus ADMM

CFAR Constant False Alarm Rate

CG Conjugate Gradient

CNN Convolutional Neural Networks

COTS Commercial Off-The-Shelf

CPI Coherent Processing Interval

CS Compressed Sensing

CT Computed Tomography

CUT Cell User Test

CVDomes Civilian-Vehicles Dome

D

DCS Dynamic Compressed Sensing

DFT Discrete Fourier Transform

DL Deep Learning

DR Detection Rate

F

FFT Fast Fourier Transform

FISTA Fast Iterative Shrinkage-Thresholding Algorithm

FMCW Frequency-Modulated Continuous-Wave

FOV Field of View

FR False Alarm Rate

G

GLRT Generalized Likelihood Ratio Test

GT Ground Truth

H

HPC High-Performance Computing

I

IF Intermediate Frequency

K

KNN K-Nearest Neighbors

L

LASSO Least Absolute Shrinkage and Selection Operator

LFM Linear Frequency Modulation

LOS Line of Sight

LRT Likelihood Ratio Test

LS Least Squares

LSTM Long Short-Term Memory

M

MAP Maximum A Posteriori

MIMO Multiple-Input Multiple-Output

ML Maximum Likelihood

MLE Maximum Likelihood Estimation

mmWave Millimeter Wave

N

NuFFT Non-uniform Fast Fourier Transform

P

PDF Probability Density Function

PFA Probability of False Alarm

PSD Power Spectral Density

PSNR Peak Signal-to-Noise Ratio

PST Projection-Slice Theorem

R

RCS Radar Cross Section

RF Radio Frequency

ROC Receiver Operating Characteristic

ROI Region of Interest

S

SADMM Sharing ADMM

SAR Synthetic Aperture Radar

SNR Signal-to-Noise Ratio

SSC Sub-Image Selection Criterion

SVM Support Vector Machine

T

TDM Time-Division Multiplexing

U

ULA Uniform Linear Array

W

WSAR Wide-Angle Synthetic Aperture Radar

Chapter 1

Introduction

Millimeter Wave (mmWave) radar sensors are becoming essential components across a wide range of indoor applications. These applications span various domains, including healthcare, smart homes, surveillance and security, industrial safety, retail analytics, and non-destructive analysis and diagnosis [1–10]. Their emergence as indispensable tools in these fields is attributed to their unique capabilities and advantages over other sensing technologies.

Compared to LiDAR sensors and cameras, radar sensors exhibit remarkable resilience under environmental conditions such as lighting variations and dust. This resilience makes them particularly suitable for indoor environments like homes, healthcare facilities, and industrial plants, where such conditions are commonly present. Additionally, radar sensors provide less intrusive solutions, making them a preferred choice for applications where privacy is a major concern [11]. Further, being lightweight and efficient in terms of power consumption fosters their suitability for indoor applications that require continuous monitoring [12]. Moreover, radar sensors possess the unique capability of penetrating walls and light materials, facilitating non-destructive testing and analysis in different domains including industrial settings. This penetration capability enables them to detect anomalies and defects within structures without physical access, reducing inspection time and costs [9, 13].

Unlike wearable sensors that require direct contact with the body, radar sensors offer a contactless monitoring solution, which is advantageous in healthcare applications. They can monitor vital signs and movements from a distance, providing greater comfort and convenience for patients and healthcare professionals [14].

Security screening is another venue where mmWave radar scanners are widely employed. Their adoption is linked to their emission of non-ionizing radiation, making them an ideal substitute for conventional backscatter X-ray systems. This characteris-

tic addresses safety concerns frequently raised around security scanners, rendering them safer for deployment in environments with human presence, such as airports and public spaces [7, 15].

1.1 Radar Images

Processing radar signals generates output in various formats, each requiring different treatment of the signal and suitable for distinct types of analysis and interpretation. These formats include range-angle maps, range-Doppler maps, micro-Doppler signatures, reflectivity images, and point cloud detections. Traditionally, a radar image refers to a high-resolution image formed using a Synthetic Aperture Radar (SAR) which represents the reflectivity of the objects in the illuminated scene scattering back the transmitted signal. However, other representations that reveal the reflectivity of targets at specific spatial or velocity bins may also be referred to as radar images. Additionally, recent advancements in mmWave technology have enabled radar sensors to achieve high-resolution detections using multiple antennas. Consequently, high-resolution radar point cloud detections are now commonly referred to as radar images, particularly in automotive and industrial applications, as their resolution approaches that of LiDAR point clouds [16, 17].

Examples of radar images are depicted in Figures 1.1, 1.2, and 1.3. The pictures in Figure 1.1 show a setup developed at our laboratory to implement a SAR. On the left, the picture demonstrates the setup featuring a single radar sensor mounted on a robotic arm and the resulting high-resolution reflectivity image displayed on the laptop screen. On the right, the picture shows the configuration of the imaged reflectors located in front of the sensor. Figure 1.2 illustrates an instance of range-Doppler and range-angle images, showcasing human targets in motion monitored by radar sensors. These measurements were collected within the smart building measurement area established at the premises of our industrial partner, IEE S.A. The layout of this measurement area is presented in Figure 1.2.(a). Figure 1.2.(b) shows a snapshot of the scenario, highlighting the sensor mounted on the wall where the reflected signals are processed. The resulting range-Doppler and range-azimuth images are displayed in Figure 1.2.(c) and (d), respectively. Finally, a high-resolution point cloud image is depicted in Figure 1.3.(b), generated by processing simulated measurements from a radar sensor equipped with a massive array of 121 transmitting and receiving antennas. The sensor measurements are simulated based on ray tracing illuminating a scene that is modeled in 3D to contain five human targets, shown in Figure 1.3.(a).

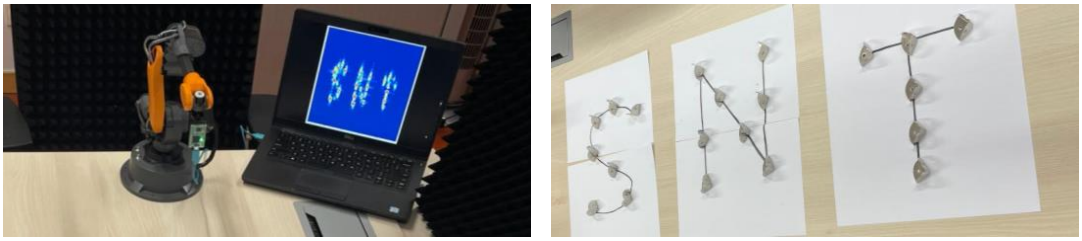

Figure 1.1: **Left:** An example of a SAR reflectivity image (displayed on the laptop screen) formed by a single radar sensor mounted on a moving robotic arm, **Right:** a picture of the targets imaged by the sensor.

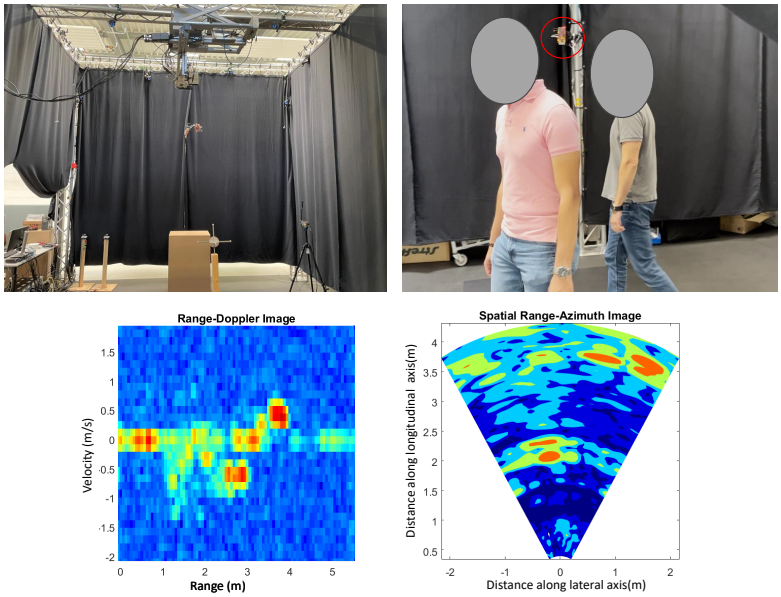

Figure 1.2: Radar images in a dynamic scenario: (a) Layout of the measurement area, (b) Snapshot of the scenario with two walking humans and the sensor mounted on the wall, (c) Associated range-Doppler map, (d) Associated range-azimuth map.

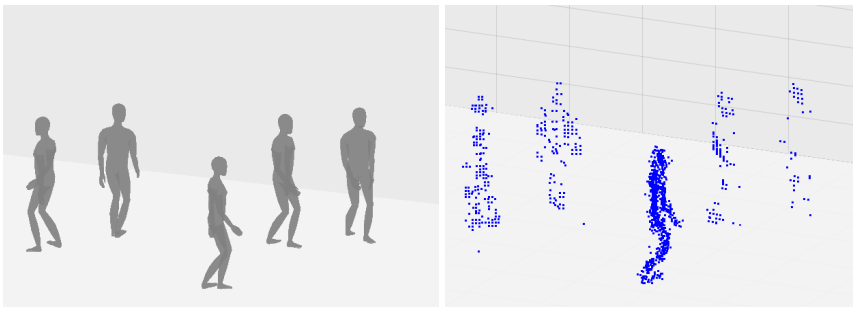

Figure 1.3: Simulated indoor scenario: (a) Ground truth, (b) Point clouds detection image.

The images displayed in the figures are produced at various stages of the radar signal processing chain. In the next section, a brief overview of the radar signal and the corresponding processing blocks will be provided.

1.1.1 Radar Signal Processing Chain

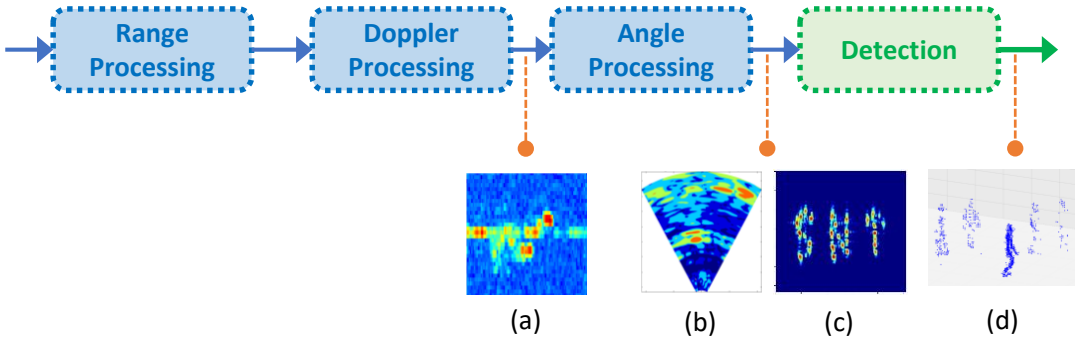

Figure 1.4: Basic radar signal processing blocks and the associated output images: (a) Range-Doppler, (b) Range-angle, (c) Reflectivity image, (d) Point clouds.

In essence, a radar sensor operates by transmitting an electromagnetic wave and subsequently capturing the back-scattered echoes from the scene, often employing multiple receiving antennas. Frequency-Modulated Continuous-Wave (FMCW) is the standard waveform utilized by mmWave sensors across various applications including indoor imaging [18, 19]. This waveform entails sweeping frequencies over the system bandwidth, with each sweep referred to as a chirp. Typically, a series of chirps are transmitted, with parameters such as sweeping time and chirp repetition interval tailored to specific application requirements. The radar receives the backscattered signals that pass through its front end which incorporates components to amplify, demodulate, and apply band-pass filtering (mixing) resulting in Intermediate Frequency (IF) signals. These IF signals are then digitized using Analog to Digital Converter (ADC) before being fed as an input to the radar signal processing block.

The digitized raw IF signals are collected over fast-time (chirp duration), slow-time (multiple chirps), and receiving antenna dimensions, and organized in a 3D data structure commonly referred to as a radar cube. Due to the mixing process, the IF signals are the sum of several sinusoids corresponding to the number of scatterers in the scene. Each sinusoidal component encapsulates details about the scattering object, with its frequency mapping to the scatterer's range, its phase difference across multiple chirps encoding velocity, and its phase difference across multiple antennas reflecting angles.

Accordingly, the IF signals are processed in order to retrieve this information about the illuminated scene resulting in the images introduced above. The basic blocks of the radar signal processing chain are depicted in Figure 1.4 and detailed below.

Range Processing is the initial stage of the radar signal processing chain which is performed to compensate for round-trip delays of the reflected signals, which result in a change of the frequency of IF signals. Accordingly, in FMCW radars, this is often achieved by applying Fast Fourier Transform (FFT) to the fast-time received signals, concentrating the signal power at frequencies corresponding to the range of scatterers, and represented by one-dimensional range-profiles.

Doppler Processing aims at retrieving the velocity information of the moving objects in the scene. This is done by considering the phase shift between consecutive chirps in received signals, caused by the motion of scatterers relative to the radar and is a function of targets' velocity. Therefore, by applying FFT on the slow-time domain after range processing, peaks form at frequencies corresponding to the target range and velocity bins, leading to the formation of a range-Doppler map as in Figure 1.4.(a).

Angle Processing follows a similar approach, accounting for phase shifts among receiving antennas caused by signal delay differences that are a function of angles of arrival. This involves compensating these phase shifts either directly through FFT or via beamforming or spatial processing techniques. Depending on the antenna array configuration, range-angle reflectivity maps can be formed in azimuth, elevation, or both. These maps are then translated into spatial maps through appropriate coordinate transformations as in Figure 1.4.(b). Additionally, Higher aperture antenna arrays result in high-resolution images, typically seen in SAR images as in Figure 1.4.(c).

Detection is the final stage of the basic radar signal processing chain. Here, the goal is to obtain a point cloud image, which can be seen as a compressed representation of previous formats. As received radar signals are often affected by noise and interference, target detection is more complex than simple peak identification. The detection block involves applying a statistical test to signals in each Cell User Test (CUT) and comparing the result with a threshold to determine the presence or absence of a scattering target. Detector design considers the statistical properties of received signals under interference, optimizing the test and threshold to achieve the desired detection performance. Applied to high-resolution spatial range-angle images, the resulting point cloud image resembles the one depicted in Figure 1.4.(d).

1.1.2 Which Radar Image?

All the aforementioned images offer valuable insights into the observed objects and their features. Accordingly, the selection of a specific radar output format over another depends largely on the particular application and the type of information necessary for the analysis.

Reflectivity images capture the intensity of back-scattered signals from objects, enabling detailed analysis of their shape and composition. This makes them a favorable representation across various domains. For example, in industrial inspection, they facilitate the identification of defects in materials or structures allowing for quality assurance in manufacturing processes. [13]. Likewise, in security screening applications, reflectivity images enable the detection of concealed threats of varying shapes and materials, giving law enforcement authorities a powerful and safe tool for threat detection [7, 8, 20].

On one hand, range-Doppler images depict the distance and velocity of objects within the radar's field of view. They serve as a fundamental representation in applications involving highly dynamic environments such as automotive applications, where the detection of moving targets like vehicles or pedestrians relies heavily on these images [21].

On the other hand, radar point clouds are often rendered in 3D, they provide a swift representation of the detected objects, facilitating localization and tracking in complex environments. This is because they present a compressed representation of the scene, enabling fast subsequent processing suitable for real-time applications [22, 23].

In the realm of human activity monitoring and recognition, the primary utilized representation is micro-Doppler images. This stems from the fact that micro-Doppler signatures capture rich information about moving objects, providing unique details regarding the movements of different parts of the body [24, 25]. However, point cloud data provides a more consistent basis for recognition that is less dependent on factors such as target's orientation and sensor parameters [18].

It is worth noting that these representations are not mutually exclusive, and a combination of different representations is often used in conjunction depending on the specific requirements of the application [4, 26].

1.1.3 Radar Images Analysis

Historically, Automatic Target Recognition (ATR) techniques have been developed to analyze radar images and extract the intended information without the intervention of a human operator. These techniques were initially implemented in military applications on SAR images and high-resolution range profiles [27, 28]. ATR algorithms analyze the

shape, size, and intensity of objects within the image to classify them into predefined categories, such as vehicles, pedestrians, or buildings. This is achieved either through model-based [29, 30] or experiment-based (training) algorithms [31, 32]. Experiment-based techniques rely on different Machine learning algorithms such as Support Vector Machine (SVM) and K-Nearest Neighbors (KNN) and eventually became widely adopted in many civilian applications [31].

In recent years, Deep Learning (DL) has become a powerful tool for radar data analysis, particularly in tasks such as classification and pattern recognition [33]. DL architectures such as Convolutional Neural Networks (CNN) and Long Short-Term Memory (LSTM) can automatically learn complex features from radar images and make accurate predictions without the need for manual feature engineering. This has led to significant improvements in the performance of extracting information from radar images, expanding the radar abilities beyond only target detection to identification and activity pattern recognition.

A significant body of the literature on DL for radar images draws from techniques and architectures initially proposed for analyzing and classifying optical images. Accordingly, they utilize radar reflectivity images, range-Doppler maps, and micro-Doppler signatures. However, recent studies are increasingly utilizing learning over point cloud images for human-pose estimation and activity recognition [34–36]. These studies rely on neural network architectures originally developed for processing LiDAR point clouds.

1.2 Motivation

Whether employing classical image processing techniques or learning algorithms to analyze radar images, it is widely acknowledged that prioritizing the acquisition of superior data is crucial. Thus, for any technique to deliver adequate performance, obtaining the highest possible image quality is of high importance. This requirement translates into obtaining high-resolution images, complete coverage of the scene of interest, and efficient detectors for point clouds.

The radar image resolution over the range dimension is achieved through the bandwidth of the transmitted wave, where the bandwidth at the mmWave band is satisfactory for many applications. However, on the angular dimension(s), the resolution is dictated by the antenna's aperture size, requiring a larger aperture for better angular resolution. In general, radar sensors operating at high frequencies, such as mmWave radar, require a relatively small aperture to achieve acceptable angular resolution, such an aperture can be realized with few antenna elements at the sensor spaced at half-wavelength. However,

in applications when a matching image resolution in all dimensions is required, a larger number of antennas and array configurations are usually employed.

Large apertures can also be realized synthetically, SAR relies on the movement of the sensor platform equipped with a single or few antennas and combining signals collected from different positions as the radar sensor moves. By processing the signals collected from multiple positions, SAR systems can effectively synthesize a larger aperture, enabling high-resolution imaging without the need for physically multiple antennas. In both cases, signals collected over the aperture are processed coherently, where a stable track of the phase of the reflected signals from the different antennas/different positions is mandatory for efficient coherent processing.

While a moving platform might be admissible or inherent for some applications such as robotics mapping, security scanners, and non-destructive material inspection [13, 20, 37], in most cases a moving radar platform is impractical, and fixed sensors are far more suitable. Alternatively, a larger aperture can be realized by multiple sensors which at the same time can bring other advantages and pose some limitations.

Accordingly, in this thesis, we aim to enhance the generation of radar images by employing distributed sensors and address some of the limitations that may impede the generation of high-quality images while building on the advantages further.

1.3 Widely Distributed Radars

Deploying a network of widely separated radar sensors offers several advantages over single-sensor configurations. Apart from the advantage of realizing a larger effective aperture by combining the signals from multiple sensors, widely separated radar networks provide spatial diversity, which is essential for capturing aspect-dependent variations in the RCS of observed targets [38, 39]. Additionally, by observing targets from multiple angles and orientations, radar networks can mitigate occlusions in the scene, both inter-object and self-occlusions, thereby enhancing the performance of target detection [40–42]. An example illustrating this and showing the detection outputs of widely distributed sensors is provided in Figure 1.5. Moreover, a network of widely separated radars offers redundancy and robustness against sensor failures. If one sensor in the network fails or is obstructed, the remaining sensors can continue to operate, ensuring continuous monitoring and coverage of the area of interest [43, 44].

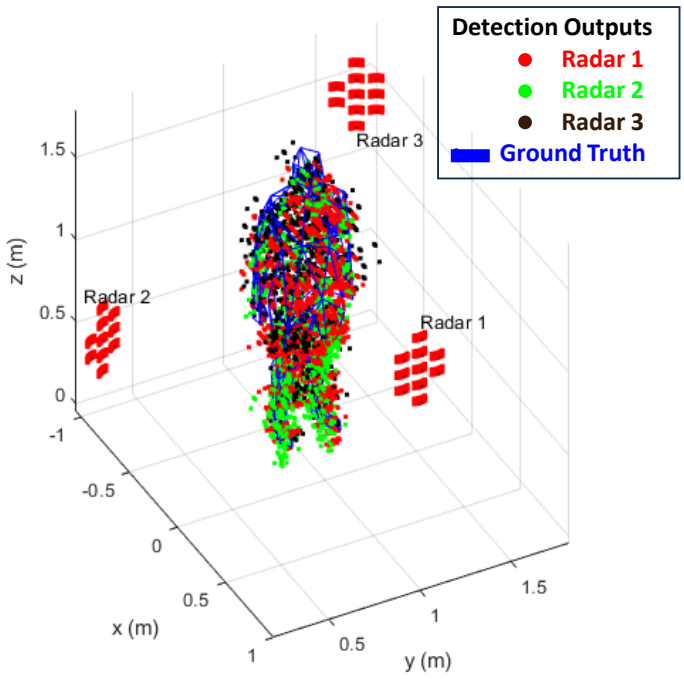

Figure 1.5: Detection outputs from three widely distributed sensors, highlighting the advantage of observing targets over wide angles. (Figure courtesy of Moein Ahmadi)

1.3.1 Challenges With Distributed Radars

When dealing with multiple sensors, the first decision to be made is how and at what level to combine or fuse their signals or outputs. Fusion of information from multiple radar sensors can occur at various levels: at the raw signal level, the processed signal level before detection, or the fusion of detection outputs [43, 44].

Dividing the signal processing chain introduced in Section1.1.1 into higher-level processing and detection blocks, Figure 1.6 illustrates the possible fusion schemes assuming a system of multiple sensors. A detailed description of each scheme and the associated challenge is provided in the sequel.

Coherent joint processing of raw signals across sensors presents two significant challenges: sensor clock synchronization and precise knowledge of sensor positions. These aspects are crucial for enabling coherent processing, as even subtle errors in either can lead to phase errors that hinder accurate joint processing [45]. Given that phase errors should be minimized to a fraction of the wavelength, these challenges are particularly pronounced in mmWave frequency bands, requiring synchronization errors on the order of picoseconds and position ambiguity in fractions of millimeters. Consequently, significant errors would impede accurate representation, thus compromising the performance

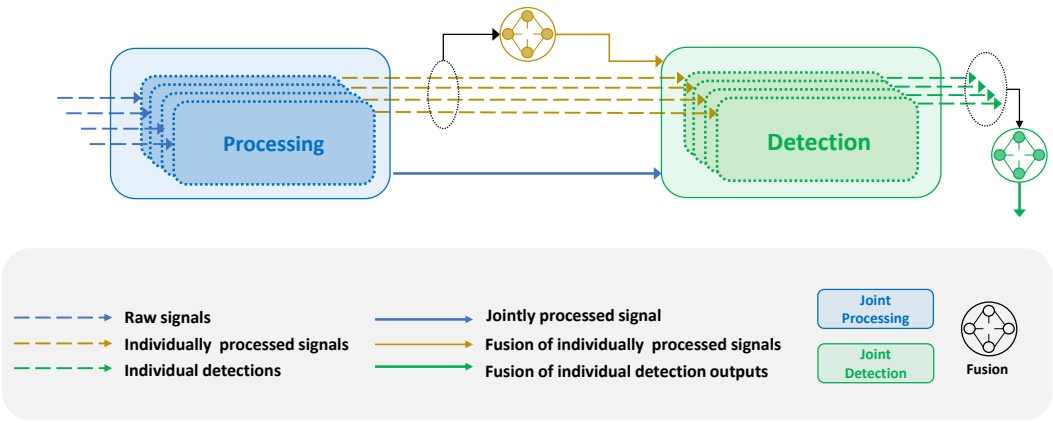

Figure 1.6: High-level radar signal processing block with an illustration of the possible schemes for fusing the signals from multiple sensors.

of subsequent image analysis. For instance, in scenarios where the intended radar output is a reflectivity image, synchronization errors can degrade image quality, resulting in blurred images. Likewise, imprecise position knowledge can produce blurry scene images, preventing correct image analysis and target recognition [46, 47]. Additionally, joint processing of raw signals necessitates transferring the signals to a central processing unit for joint processing. This is often a limiting factor for fusion at the raw signal level due to constraints on communication interfaces at the sensors and channels to a central unit.

Alternatively, distributed sensor nodes may locally process the raw signal and transmit the processed data to a central unit before detection. This approach allows for exchanging compressed data formats, requiring significantly less communication bandwidth between the sensors and a central decision or fusion unit. While this reduced complexity sacrifices coherent integration gain, it becomes suitable for many applications with simple hardware setups. The processed signal can then undergo fusion or pass through a detector block for joint detection. If the desired output is at the processed signal level, such as a reflectivity image, the images may be combined to obtain a global view of the scene. Fusion methods range from simple addition or averaging to weighted fusion, with weights determined by specific metrics based on each sensor's measurement reliability, including Signal-to-Noise Ratio (SNR), target's location, or velocity relative to the sensor. Similarly, for joint detection, signals can be non-coherently integrated while applying a detection test, which can favor one sensor's measurement over another based on similar metrics. Hence, in this scheme, identifying the optimal strategy for

fusing the processed signal can enhance performance in the subsequent analysis stage.

Lastly, fusion can occur post-detection, where the point cloud outputs from each sensor are combined. This approach is typically employed for tasks related to localization and tracking. In this scenario, the primary processes for data fusion involve clustering the point clouds and then fusing them by calculating the centroid distances of the clusters and retaining overlapping regions. Alternatively, for object tracking, fusion can occur directly at the track level using methods like covariance intersection. Both fusion methods inherently suggest that improving the quality of point cloud detections (reducing cluster spread/tracks' uncertainty/false alarms) should enhance the fusion process. This improvement can be achieved by enhancing the detection tests by considering environment modeling for example.

1.4 Contributions

This thesis does not aim to provide an exhaustive treatment of all radar signal processing blocks and output representations used in indoor applications. Instead, it focuses on enhancing the output of two specific processing blocks and their corresponding representations: reflectivity images and detection point clouds.

Reflectivity images are valued across many applications that require a comprehensive description of the targets in the scene whether static or dynamic, at a specific moment in time. Moreover, they enable immediate analysis using classical image processing methods or advanced deep learning techniques, extensively studied for optical images.

On the other hand, detection point clouds serve as a straightforward representation in scenarios where processing an image or sequence thereof is cumbersome for both sensor capabilities and subsequent analysis, such as tracking or identification tasks in applications where complex sensors are impractical. Additionally, while micro-Doppler maps are commonly used in human activity monitoring due to their ability to capture unique dynamic signatures, there is a growing interest in using detection point clouds for human activity recognition and pose estimation. This is because point clouds offer a geometrical representation of the target in the spatial domain, overcoming challenges related to sensor parameters and aspect angles encountered in micro-Doppler maps. Thus, detection point clouds present a promising avenue for leveraging transfer learning over existing neural network architectures developed for LiDAR point clouds.

Therefore, the thesis is organized into two parts, each dedicated to one of these representations. In the subsequent section, the contributions of the thesis are highlighted, along with references to the corresponding chapters providing the thesis outlines.

1.4.1 Thesis Organization

Part I: Reflectivity Image Formation This part focuses on generating high-resolution reflectivity images of scenes observed by widely distributed radar sensors. The image formation involves solving the inverse problem of reconstructing the image of the scene over a 2D grid. Leveraging Compressed Sensing (CS) methods, various algorithms are proposed to address some of the challenges outlined in Section 1.3.1. The contributions are detailed as follows

- **Chapter 2** introduces a novel approach to reconstructing a global image of an observed scene by widely distributed radar sensors, utilizing the Alternating Direction Method of Multipliers (ADMM) optimization framework. This method aims to generate a fused image of the scene without the need for a late fusion step. The chapter presents two problem formulations, namely Consensus ADMM (CADMM) and Sharing ADMM (SADMM), along with their iterative algorithms. Furthermore, it outlines explicit variable updates for each algorithm and suggests a hybrid parallel implementation scheme for distributed sensors and a central processing unit.

- **Chapter 3** proposes a heuristic approach to accelerate the convergence of the ADMM formulations introduced in the previous chapter. This acceleration is achieved by gradually eliminating already converged pixels based on a predetermined criterion. By focusing on the image portion containing scattering targets and updating sub-images accordingly, this method not only reduces running time but also computational complexity and communication costs between sensors during iterative updates.

- In **Chapter 4**, the problem of hyperparameter tuning in CS-based radar image reconstruction algorithms is addressed. A method for automatic selection of regularization parameters is proposed, enhancing the efficiency of joint reconstruction of scene images observed by partially synchronized distributed radar sensors. This method eliminates the need for empirical search and introduces an efficient implementation based on the FFT to reduce algorithm running time and memory requirements. The proposed method is implemented by modifying a Fast Iterative Shrinkage-Thresholding Algorithm (FISTA)-based algorithm existing in the literature, enabling efficient joint reconstruction of the scene image and correction of synchronization errors.

Part II: Point Clouds Detection This part delves into detector design using statistical detection theory based on hypothesis testing. It tackles two problems: joint detector design using processed signals from widely distributed radar sensors, and detector design for an individual high-resolution mmWave radar sensor incorporating modeling of occlusion over individual range profiles. The contributions related to this part are detailed in the corresponding chapters below.

- **Chapter 5** focuses on detecting fluctuating targets using distributed mmWave radar sensors. It formulates joint hypotheses leading to the design of a joint detector based on the Generalized Likelihood Ratio Test (GLRT). This detector estimates the fluctuation parameters of targets at each sensor using multiple chirps, resulting in a joint test that is a weighted sum of individual tests applied to the square law detector output of each sensor. The proposed detector accounts for variations in aspect angles and path losses for a single CUT by weighting the local SNR at each sensor. It offers improved detection performance compared to a conventional square law detector applied directly to the integrated processed signals of the sensors.

- **Chapter 6** focuses on enhancing detection performance at individual sensors, which inherently improves overall detection when fusion is performed at the point cloud level. It proposes a novel formulation of null and alternative hypotheses leveraging the sparse structure of range profiles due to cell-level occlusion occurring when sensors with high angular resolution are employed. The resulting detector aims to enhance the detection of non-occluded targets, providing accurate high-resolution point clouds. Performance evaluation includes model-based numerical simulations and scenario-based simulations, where a dynamic indoor scenario is modeled in 3D and the reflected radar signal is generated using ray-tracing.

Finally, **Chapter 7** concludes the thesis and provides insights into possible research directions building on the work presented in the thesis. All chapters in this thesis are self-contained, corresponding to the manuscripts derived from this thesis (Section 1.4.2). As such, each chapter includes the necessary background and literature review, system and signal models employed in problem formulation, as well as the adopted notation.

1.4.2 List of Publications

The research presented in this thesis has led to several peer-reviewed journal and conference papers, which are either currently published or under review. The publications associated with this thesis are provided below.

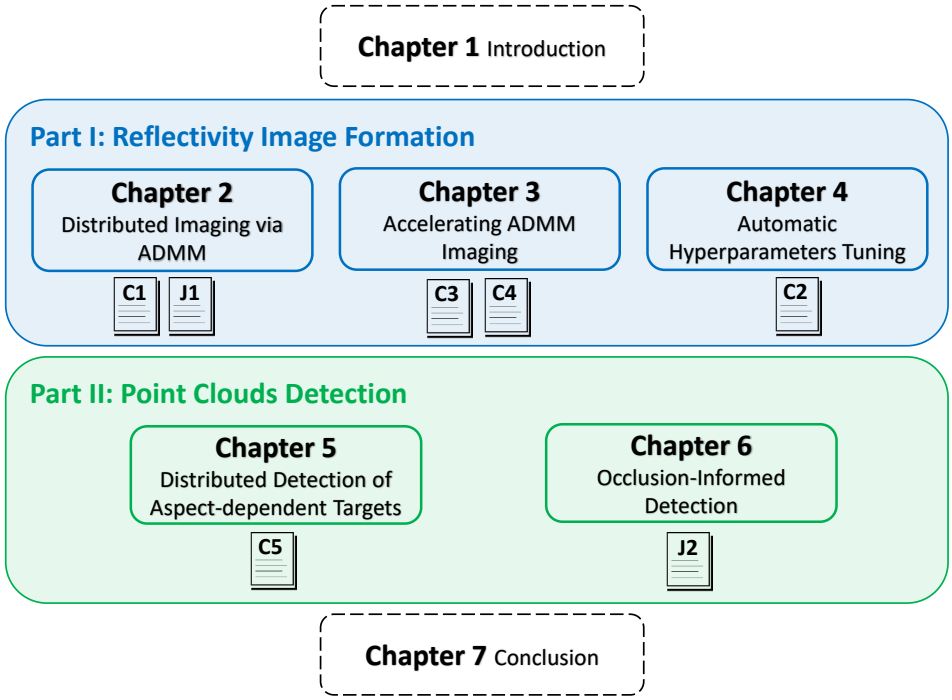

Figure 1.7: Thesis outline and the corresponding publications linked to each chapter

Journals

J1 : **A. Murtada**, R. Hu, B. S. Mysore Rama Rao, and U. Schroeder, "Widely Distributed Radar Imaging: Unmediated ADMM Based Approach", in IEEE Journal of Selected Topics in Signal Processing, vol. 17, no. 2, pp. 389-402, March 2023. DOI [48]

J2 : **A. Murtada**, B. S. Mysore Rama Rao, M. Ahmadi, and U. Schroeder, "Occlusion-Informed Radar Detection for Millimeter-Wave Indoor Sensing", IEEE Open Journal of Signal Processing. (Resubmitted on April 1st 2024)

Conferences

C1 : R. Hu, B. S. Mysore Rama Rao, **A. Murtada**, M. Alaee-Kerahroodi and B. Ottersten, "Widely-distributed Radar Imaging Based on Consensus ADMM", 2021 IEEE Radar Conference (RadarConf21), 2021, pp. 1-6. DOI [49]

C2 : **A. Murtada**, R. Hu, M. Alaee-Kerahroodi, U. Schroeder and B. S. Mysore Rama Rao, "Efficient Radar Imaging Using Partially Synchronized Distributed Sensors", 2021 IEEE Radar Conference (RadarConf21), 2021, pp. 1-6. DOI [50]

C3 : **A. Murtada**, B. S. Mysore Rama Rao, M. Alaee-Kerahroodi, R. Hu, and U.

Schroeder, “Accelerated Consensus ADMM for Widely Distributed Radar Imaging”, 2022 IEEE Radar Conference (RadarConf22), 2022, pp. 1-6. DOI [51]

C4 : **A. Murtada**, B. S. Mysore Rama Rao, and U. Schroeder, “Distributed Radar Imaging Based on Accelerated ADMM”, 2023 International Symposium on Computational Sensing (ISCS23), 2023, DOI. [52]

C5 : **A. Murtada**, B. S. Mysore Rama Rao, and U. Schroeder, “GLRT Detector for Aspect-dependent Fluctuating Targets Using Distributed mmWave MIMO Radar Sensors”, 2023 European Signal Processing Conference (EUSIPCO23), 2023, pp. 1574-1578. DOI [53]

Figure 1.7 shows the structure of the thesis and the corresponding publications linked to each chapter.

Part I

Reflectivity Image Formation

Chapter 2

Distributed Imaging via ADMM

This chapter explores the joint reconstruction of a high-resolution reflectivity image of a scene observed by widely distributed radar sensors. It introduces a novel approach to directly reconstructing a global image of the scene using the ADMM optimization framework, eliminating the need for an explicit fusion step. The problem is formulated as a constrained optimization problem in which the global image which represents the aggregate view of the sensors is a decision variable. Leveraging compressed sensing techniques for high-resolution images, the problem is designed to promote a sparse solution for the global image respecting a relationship with local images that can be reconstructed using measurements at each sensor. Two problem formulations are introduced by stipulating two different constraints of that relationship. The proposed formulations are designed according to consensus ADMM (CADMM) and sharing ADMM (SADMM), and their solutions are provided accordingly as iterative algorithms. Additionally, a scheme for hybrid parallel implementation on the distributed sensors and a central processing unit is introduced. The algorithms are validated on the Civilian Vehicles Dome dataset, showcasing their performance across various practical scenarios.

2.1 Introduction

Widely distributed radar systems are robust and fault-tolerant systems that provide high angular resolution and permit the exploitation of spatial diversity and occlusion avoidance [38]. They may also be viewed as synthesizing wide aperture in the spatial domain [54]. The emergence of Commercial Off-The-Shelf (COTS) mmWave radar modules with wide bandwidths over 4 GHz enables such a wide aperture using spatially well-separated modules. With applications in surveillance, assisted living, and health monitoring, radar systems with distributed antennas are expected to play a vi-

tal role in emerging sensing paradigms [11, 55]. Under this architecture, the observed targets feature an aspect-dependent scattering behavior restricting the employment of conventional imaging methods. The main impediment arises due to the adoption of the isotropic point scattering model of targets, thereby preventing algorithms like Back Projection (BP) from providing an adequate imaging performance [40].

The works [47, 56, 57] considered radar imaging with distributed antennas and the related issues due to ambiguity in antenna positions and clock synchronization. In these works, model-based optimization algorithms are utilized to jointly achieve the imaging task and resolve such issues. However, in these works, an isotropic scattering model, suitable when antennas are closely spaced, is assumed; this is not suitable when widely separated antennas are considered.

On the other hand, in Wide-Angle Synthetic Aperture Radar (WSAR), which bears a close resemblance to a widely distributed architecture, two approaches exist for imaging [58]. The first approach includes methods that utilize the full aperture data jointly. It encompasses the methods that are based on parametric modeling that characterizes the canonical scattering behavior of scatterers [59–62]. Correspondingly, the scene image is reconstructed through joint processing of the measurements from the whole aperture exploiting the model. Nevertheless, the imaging involves a dictionary search process that is computationally cumbersome [30]. Additionally, when sensors are widely separated, coherent processing of the scene might not be achievable due to the targets becoming non-homogeneous as they are observed from widely varying aspect angles.

The second approach is composite imaging [63–66] in which the full aperture is divided into sub-apertures within which the point scattering model holds. At first, images of each sub-aperture are formed through regularized optimization exploiting specific features such as sparsity and smoothness. Subsequently, individual images are fused to constitute an aggregate image of the scene through simple techniques such as the GLRT. This approach does not fully exploit the information from different aspects where the final image of the scene is only a fused version of the images reconstructed with sub-aperture data. Among other sub-aperture methods, Dynamic Compressed Sensing (DCS) [67–70] aims to exploit the evolution of the scattering behavior structure along with the common sparse structure of sub-aperture images. These methods estimate a sequence of images and also do not attempt to reconstruct a single image; this has been referred to as a drawback in [71]. Moreover, they are heavily reliant on the assumptions of joint sparsity with highly overlapping support among sub-apertures and a gradual change of such support [67, 69–71]. These assumptions are severely violated when views and bandwidth are limited. Additionally, since those methods require either process-

ing the entire data sequentially or jointly, an efficient parallel implementation becomes difficult to realize [58].

While we also propose a sub-aperture method, unlike composite imaging, we aim to solve the problem of widely distributed radar imaging by directly reconstructing a global image that is introduced as an aggregate view of the scene. Besides, the prior information is only imposed on the global image rather than the local images of individual sensors. Concurrently, the correspondence between the local images and the global one is defined as a constraint to the optimization problem. Our approach allows for better data exploitation by including the global image as a decision variable in the optimization problem. We then provide a solution based on the ADMM framework [72]. ADMM is a powerful distributed optimization regime suitable for systems that incorporate a collection of measurements through a distributed architecture. In [73] and [74], ADMM has been introduced as a fast reconstruction method for generic imaging inverse problems. Further, in [75] it is applied to reconstruct complex SAR images with enhanced features in particular and to perform imaging with under-sampled measurements in the presence of phase errors in [76].

While in these works ADMM has been mainly utilized to facilitate the solution of a non-constrained optimization problem by the virtue of variable splitting, we employ its constrained formulation directly in the interest of exploiting the system architecture and implementing parallelizable image reconstruction algorithms. Accordingly, we establish two problem formulations inspired by CADMM and SADMM. The first formulation comes as a generalization of the method in [49], in which CADMM is utilized to mitigate the layover artifacts in widely distributed radar imaging by considering sub-aperture measurements from different elevations. While CADMM imposes a consensus on all sub-images, albeit under an anisotropic setting, we present CADMM as a low-complexity initial work that introduces the association between sub-aperture images and the global image and reconstructs the image of the scene without restriction on data viewing angles. Moreover, by stipulating the more relaxed sharing association in the constraints, we introduce the second problem formulation based on SADMM. The different association introduced by SADMM formulation enables another exploitation of the relationship between the data collected by the sub-apertures. Additionally, it provides an alternative realization of the system architecture through the ensuing unalike solution. We provide the solutions as iterative algorithms with a recommendation of a parallel implementation paradigm. Finally, the Civilian Vehicles Dome dataset [77] is used to realize three experiments that comprise different practical use cases. Through them, we validate our algorithms and show the performance of CADMM and SADMM, where the latter is

found to provide an enhanced imaging performance in most of the scenarios.

The contribution of this chapter lies in the introduction of a parallelizable distributed optimization framework to reconstruct an image of a scene observed by widely distributed radar apertures without the need for an explicit later fusion step. The proposed framework allows the adoption of any prior information about the observed scene in addition to giving the liberty to stipulate the relation between the global image and the measurements collected by individual apertures. Moreover, validate the proposed approach by exploiting the prior information on the sparsity of the global image and establishing the consensus and sharing relationships between global and local images. Our proposed approach is well-adapted for implementation on various architectures including WSAR and radar systems with collocated antennas.

Throughout this chapter, vectors are denoted in lowercase bold font, while matrices are in uppercase bold. $\mathbf{I}_L$ is the identity matrix of size $L \times L$ and $\mathbf{1}_N$ is a vector of all ones of size $N \times 1$. The superscripts $(.)^T$ and $(.)^H$ denote, respectively, the transpose and the complex conjugate transpose of a vector or a matrix. On the other hand, superscripts in parentheses denote the iteration count. The symbol $\otimes$ is used for the Kronecker product.

2.2 Signal Model and Background

In this section, we present the considered distributed architecture, introduce the adopted signal model, and provide background about the imaging problem formulation in the literature.

Considering the system geometry illustrated in Figure 2.1, a group of red crossed circles constitutes a cluster of Antenna Phase Centers (APCs). The figure shows the case we consider in this chapter where each of the Q sensors forms a single cluster at identical elevation angles. We consider a mono-static configuration where each sensor receives the reflections due to its own illumination of the scene and does not process the reflections induced by transmissions from others. Accordingly, our proposed algorithms can be applied to architectures that are formed either by a synthetic or a real aperture. At each cluster, the isotropic scattering model of the targets in the scene is assumed. This way, the problem of aspect-dependent scattering behavior can be relaxed and Q local images can be formed by processing the measurements of individual clusters. The local images can then be appropriately combined at a central node, or the fusion center, to generate the image of the entire scene. The fusion center can subscribe to different combining methodologies, e.g., averaging or pixel-wise maximum, some of which will be

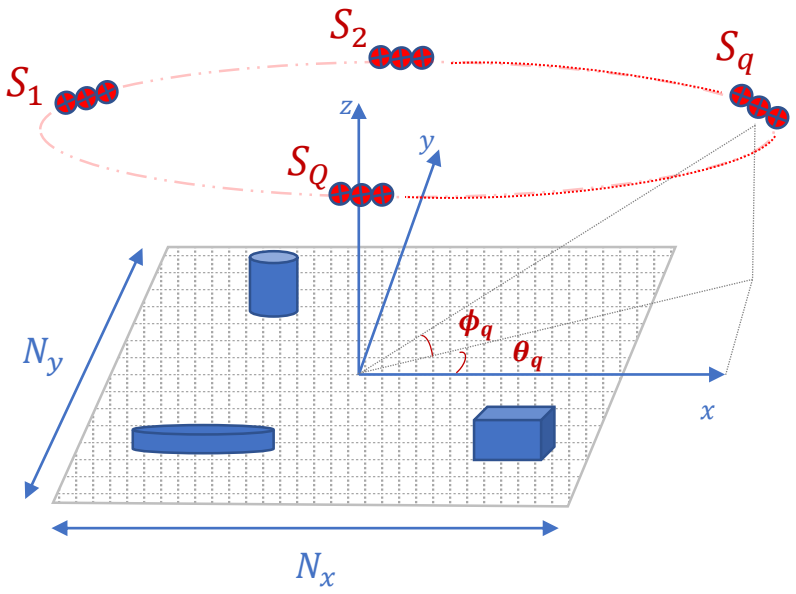

Figure 2.1: Geometry of Distributed Radar System

explored in the sequel.

2.2.1 Tomography Inspired Modeling

Since the system comprises distributed sensors stationed at a diverse range of aspect angles and our goal is to form a 2D reflectivity image of the scene, we adopt the tomographic radar imaging framework [78] to describe the signal model. The tomographic model relies on the Projection-Slice Theorem (PST), a foundational result Computed Tomography (CT) where a cross-section of an internal body part is imaged by detecting the attenuation of traversing X-rays. In a CT scan, the subject is exposed to a parallel beam of X-rays at a wide range of angles. At each angle, a row of detectors at the opposite side measures the attenuation by forming a projection profile of the intensity function of the imaged part along the emitting direction. PST (also known as Fourier-Slice Theorem) states that the one-dimension (spatial) Fourier transform of a projection profile at an angle θ is equivalent to the 2D Fourier transform of the intensity function evaluated at a slice (line) that lies at the same angle θ in the spatial frequency domain. This result allows for direct inversion of the measured projections after taking a Fourier transform to reconstruct the desired intensity image.

Similarly, radar imaging systems having a geometry that favors spatial diversity, have adopted the tomographic signal model for simpler interpretation and direct applicability of efficient tools such as the FFT. Such systems include Spotlight-SAR and Circular-SAR, in addition to custom multistatic geometries [79]. However, the application of

PST in radar imaging differs in some aspects with respect to CT due to the differences in both the acquisition method and the nature of the scattering to be recovered. In Radar imaging, the measured signal is a transformed version of a transmitted waveform, which is delayed in time and shifted in phase due to the location and proprieties of the scattering target. As a result, the measured quantity is not the projection of the scattering of the target as the case in CT *per-se*. Consequently, some restrictions, which are governed by the transmitted signal bandwidth, are imposed on the available spatial frequency samples. The frequency samples are located on an annulus centered around the carrier frequency with a width proportional to the signal bandwidth. However, effective image reconstruction from these limited portions is still possible using the frequency content of these sectors [80]. We refer the readers to [78–81] for additional background about the tomographic modeling of Radar imaging including its advantages and limitations.

2.2.2 Distributed Radar Imaging Model

We consider the sensors to transmit the commonly used Linear Frequency Modulation (LFM) waveform with a chirp rate ν. Consequently, they receive a scaled and time-shifted version of the transmitted waveform as a reflection from the scene. According to the aforementioned tomographic model, the discrete phase history received at the m^{th} antenna of the q^{th} sensor after dechirping and low-pass filtering follows

$$\begin{aligned} y_q^m(k) &= \iint\limits_{\Omega} \tilde{x}_q\left(x,y\right) \exp\left\{-j\frac{4\pi f_k}{c}\Delta R_q^m(x,y)\right\} dx\ dy \\ \Delta R_q^m(x,y) &= \cos\varphi_q\left(x\cos\theta_{q,m} + y\sin\theta_{q,m}\right), \end{aligned} \tag{2.1}$$

where $\Delta R_q^m(x,y)$ is the difference of the distances from the sensors to the scene center and to a ground target located at coordinates (x,y) assuming far-field scenario, $m = 1,\ldots,M$ is the index of antenna elements within each cluster, $q = 1,\ldots,Q$ is the index of a sensor/cluster, $k = 1,\ldots,K$ is the index of fast-time samples, Ω is the ground footprint, which is assumed to be the same for all antennas, $\tilde{x}_q\left(x,y\right)$ indicates the complex reflectivity coefficient of a ground target at coordinates (x,y) with respect to the q^{th} cluster, $f_k = (f_c + 2\nu k T_s)$ denotes the linear transmitted frequency where f_c is the carrier frequency and T_s is the fast-time sampling period, c is the speed of light, φ_q is the elevation angle of the q^{th} cluster, and $\theta_{q,m}$ is the azimuth angle of the m^{th} antenna element of the q^{th} cluster.

By discretizing the scene with a uniform grid of $N = N_x \times N_y$ pixels $\{(x_n, y_n)\}_{n=1}^{N}$

and stacking $\left\{\left\{y_q^m(k)\right\}_{k=1}^{K}\right\}_{m=1}^{M}$ into a vector $\mathbf{y}_q$, the phase history measurements can be written in a matrix form as

$$\mathbf{y}_q = \mathbf{A}_q\tilde{\mathbf{x}}_q + \mathbf{w}_q \in \mathbb{C}^{KM\times 1}, \tag{2.2}$$

where $\mathbf{A}_q = \left[\boldsymbol{\alpha}_q^1, \boldsymbol{\alpha}_q^2, \cdots, \boldsymbol{\alpha}_q^N\right] \in \mathbb{C}^{KM\times N}$ is the system model based forward operator that its columns $\boldsymbol{\alpha}_q^n \in \mathbb{C}^{KM\times 1}$ take the form

$$\boldsymbol{\alpha}_q^n = \begin{bmatrix} \exp\left\{-j4\pi f_1 \cos\varphi_q/c\left(x_n\cos\theta_{q,1} + y_n\sin\theta_{q,1}\right)\right\} \\ \exp\left\{-j4\pi f_2 \cos\varphi_q/c\left(x_n\cos\theta_{q,1} + y_n\sin\theta_{q,1}\right)\right\} \\ \vdots \\ \exp\left\{-j4\pi f_K \cos\varphi_q/c\left(x_n\cos\theta_{q,1} + y_n\sin\theta_{q,1}\right)\right\} \\ \vdots \\ \exp\left\{-j4\pi f_1 \cos\varphi_q/c\left(x_n\cos\theta_{q,M} + y_n\sin\theta_{q,M}\right)\right\} \\ \exp\left\{-j4\pi f_2 \cos\varphi_q/c\left(x_n\cos\theta_{q,M} + y_n\sin\theta_{q,M}\right)\right\} \\ \vdots \\ \exp\left\{-j4\pi f_K \cos\varphi_q/c\left(x_n\cos\theta_{q,M} + y_n\sin\theta_{q,M}\right)\right\} \end{bmatrix}, \tag{2.3}$$

$\tilde{\mathbf{x}}_q \in \mathbb{C}^{N\times 1}$ is the vector containing the complex scattering coefficients of the entire scene with respect to the q^{th} cluster, and $\mathbf{w}_q \in \mathbb{C}^{KM\times 1}$ summarizes all errors including receiver and measurement noise as well as model imperfections.

2.2.3 State-of-the-art Problem Formulation

Composite imaging algorithms obtain local images utilizing the signal received at each cluster and subsequently fuse them into a global image. The scene size is usually much larger than the number of measurements $N >> KM$ and the imaging task is the inverse problem of (2.2) which, consequently, becomes ill-posed. Compressed sensing methods are commonly used to solve this inverse problem. Particularly, local images are obtained by solving Q regularized least square optimization problems for each cluster of the form

$$\hat{\mathbf{x}}_q = \arg\min_{\tilde{\mathbf{x}}_q}\left\{\left\|\mathbf{y}_q - \mathbf{A}_q\tilde{\mathbf{x}}_q\right\|_2^2 + h(\tilde{\mathbf{x}}_q)\right\}, \tag{2.4}$$

where $\hat{\mathbf{x}}_q$ is the estimated local image using the measurements $\mathbf{y}_q$ for $q = 1, \ldots, Q$ and $h(\cdot)$ is a regularization function that imposes apriori information about local images.

Different choices of regularization function $h(\cdot)$ exist to enhance some image features such as sparsity and smoothness, among others. When $h(\cdot)$ is a separable function (e.g. l_1-norm), the Q problems can be represented as a single optimization problem in Q variables since the least squares term is naturally separable. Explicitly, the problem can be written as

$$\left\{\hat{\mathbf{x}}_1, \ldots, \hat{\mathbf{x}}_Q\right\} = \min_{\tilde{\mathbf{x}}_1, \tilde{\mathbf{x}}_2, \cdots, \tilde{\mathbf{x}}_Q} \sum_{q=1}^{Q} \left\{ \left\| \mathbf{y}_q - \mathbf{A}_q \tilde{\mathbf{x}}_q \right\|_2^2 + \left\| \tilde{\mathbf{x}}_q \right\|_1 \right\}. \tag{2.5}$$

The problem in (2.5) is an unconstrained regularized optimization problem that has been tackled through different optimization techniques in the literature. Finally, the image of the scene is obtained through a fusion step of the Q reconstructed images which can be as simple as a pixel-wise maximization among the Q local images.

As mentioned in the introduction, we alternatively reconstruct the global image of the scene by introducing its variable in the objective function and imposing the l_1-norm on it directly for a sparsity-driven solution. Simultaneously, the relationship between the global image and local images is defined as a constraint for our optimization problem. In the next section, based on the ADMM framework, we provide two alternative problem formulations along with their solutions.

2.3 ADMM Framework for Distributed Radar Imaging

ADMM is a powerful framework that renders itself amenable to optimization problems of a distributed nature. It is a suitable tool to be utilized in a distributed radar system especially when the component sensors are equipped with some computation power capabilities. Although this computation power might be limited, it can be exploited to process some information in order to reduce the communication overhead and the computational burden at the central node. It also reduces latency as certain operations can already be performed in parallel at the nodes. Here, we first give a brief introduction of general ADMM formulation followed by our proposed reformulations of the problem in (2.5) according to the ADMM framework.

Consider the following constrained optimization problem with linear constraints over two separable functions in two variables $\mathbf{u}$ and $\mathbf{z}$

$$\begin{aligned} &\arg\min_{\mathbf{u},\mathbf{z}} f(\mathbf{u}) + g(\mathbf{z}) \\ &s.t. \quad \mathbf{G}\mathbf{u} + \mathbf{H}\mathbf{z} = \mathbf{c}, \end{aligned} \tag{2.6}$$

where $\mathbf{G}$, $\mathbf{H}$, and $\mathbf{c}$ are the matrices and vectors of appropriate dimensions that establish the constraints on the variables $\mathbf{u}$ and $\mathbf{z}$. The augmented Lagrangian function of the above problem becomes

$$\mathcal{L}\left(\mathbf{u},\mathbf{z},\boldsymbol{\sigma}\right)=\left\{f(\mathbf{u})+g(\mathbf{z})+\langle\boldsymbol{\sigma},\mathbf{G}\mathbf{u}+\mathbf{H}\mathbf{z}-\mathbf{c}\rangle+\quad\frac{\beta}{2}\left\|\mathbf{G}\mathbf{u}+\mathbf{H}\mathbf{z}-\mathbf{c}\right\|_2^2\right\} \tag{2.7}$$

where $\boldsymbol{\sigma}$ is the dual variable, β is the augmented Lagrangian parameter, and $\langle\cdot,\cdot\rangle$ denotes the inner product of vectors.

The ADMM solution to the above problem is obtained by iteratively minimizing the augmented Lagrangian function with respect to both the variables $\mathbf{u}$ and $\mathbf{z}$ in an alternating fashion in addition to updating the dual variable each iteration. Accordingly, after the k^{th} iteration, the ADMM variable updates consist of [72]

$$\begin{aligned}\mathbf{u}^{(k+1)}&:=\arg\min_{\mathbf{u}}\mathcal{L}\left(\mathbf{u},\mathbf{z}^{(k)},\boldsymbol{\sigma}^{(k)}\right)\\ \mathbf{z}^{(k+1)}&:=\arg\min_{\mathbf{z}}\mathcal{L}\left(\mathbf{u}^{(k)},\mathbf{z},\boldsymbol{\sigma}^{(k)}\right)\\ \boldsymbol{\sigma}^{(k+1)}&:=\boldsymbol{\sigma}^{(k)}+\beta\left(\mathbf{G}\mathbf{x}^{(k+1)}+\mathbf{H}\mathbf{z}^{(k+1)}-\mathbf{c}\right)\end{aligned} \tag{2.8}$$

Embracing the ADMM framework, we propose two different formulations as alternatives to (2.5). Towards introducing the new formulations, we introduce the global image, which is a unified entity representative of the scene; this refers to the output of the fusion step mentioned in Section 2.2. This global image can be interpreted and utilized based on the application. For example, for ATR tasks, the global image provides a strong means to identify and classify targets. Similarly, the global image serves to detect occluded targets or parts of the same target that are prone to self-occlusion.

By introducing a new variable $\mathbf{x}_{\mathbf{G}}\in\mathbb{R}^{N\times 1}$ representing the magnitude of the global image, both the formulations will have the same objective function of minimizing the sum of the least square terms with respect to local images, in addition to minimizing the l_1 norm of the global image. The formulations differ in the constraints which define the relationship between the global and local images. The optimization in imaging can be carried out on real variables by decoupling complex images into their corresponding magnitude and phase [64, 82]. Consequently, we consider the magnitude of the images as our optimization variables assuming that the phases are estimated in a previous step. Specifically, we assume that we have estimated $\boldsymbol{\Theta}_q\in\mathbb{C}^{N\times N}$, the diagonal matrix containing the phase of all pixels of local image over its diagonal such that $\tilde{\mathbf{x}}_q=\boldsymbol{\Theta}_q\mathbf{x}_q$. For ease of notation, from now on we will consider the matrix $\boldsymbol{\Theta}_q$ included in the measurement matrix $\mathbf{A}_q$. The details regarding the estimation of $\boldsymbol{\Theta}_q$ will be discussed

in the next section. Accordingly, with reference to (2.6), our first variable is $\mathbf{x} \in \mathbb{R}^{QN\times 1}$ containing the magnitude of all local images $\mathbf{x} = \{\mathbf{x}_q\}_{q=1}^{Q}$, and the second variable represents the magnitude of the global image $\mathbf{x_G}$. Consequently, our objective function contains $f(\mathbf{x}) = \sum_{q=1}^{Q} \left\|\mathbf{y}_q - \mathbf{A}_q\mathbf{x}_q\right\|_2^2$ and $g(\mathbf{x_G}) = \|\mathbf{x_G}\|_1$.

In the sequel, we will provide our proposed aforementioned formulations and their solutions in terms of variable updates according to (2.8).

2.3.1 Consensus ADMM (CADMM)

As the name suggests, by posing the problem according to this formulation, we pursue a solution that, at optimum, provides a sparse global image on which all clusters reach a consensus. While this chapter considers a scene that contains anisotropic targets, CADMM is presented as an initial work toward introducing distributed optimization for imaging applications. Consequently, the constraints, in this case, are defined to impose this relationship between the global and local images. Additionally, as mentioned earlier and by following [49], we impose the l_1-norm function to promote a sparse global image solution. The problem becomes

$$\begin{aligned} \underset{\mathbf{x},\mathbf{x_G}}{\arg\min} \quad & \sum_{q=1}^{Q} \frac{\mu}{2} \left\|\mathbf{y}_q - \mathbf{A}_q\mathbf{x}_q\right\|_2^2 + \lambda \left\|\mathbf{x_G}\right\|_1 \\ s.t. \quad & \mathbf{x}_q - \mathbf{x_G} = \mathbf{0} \quad \forall q. \end{aligned} \tag{2.9}$$

where λ and μ are positive hyperparameters set to penalize less sparse global image solutions and trade-off the data fidelity term, respectively. Note that the Q constraints in (2.9) can be written in the form of the constraint in (2.6) by having $\mathbf{G} = \mathbf{I}_{QN}$, $\mathbf{u} = \mathbf{x}$, $\mathbf{H} = -[\mathbf{I}_N, \mathbf{I}_N, \cdots \mathbf{I}_N]^T$ of the size $QN \times N$, $\mathbf{z} = \mathbf{x_G}$, and $\mathbf{c} = \mathbf{0}$ of size $QN \times 1$.

As indicated in (2.8), the solution of (2.9) can be obtained by alternately minimizing its associated augmented Lagrangian with respect to $\mathbf{x}$, $\mathbf{x_G}$, and the dual variable $\boldsymbol{\sigma}$. The augmented Lagrangian is

$$\mathcal{L}\left(\mathbf{x}, \mathbf{x_G}, \boldsymbol{\sigma}\right) = \sum_{q=1}^{Q} \left\{ \frac{\mu}{2} \left\|\mathbf{y}_q - \mathbf{A}_q\mathbf{x}_q\right\|_2^2 + \left\langle \boldsymbol{\sigma}_q, \mathbf{x}_q - \mathbf{x_G} \right\rangle \right\} + \frac{\beta}{2} \left\|\mathbf{x}_q - \mathbf{x_G}\right\|_2^2 + \lambda \|\mathbf{x_G}\|_1, \tag{2.10}$$

where $\boldsymbol{\sigma}_q \in \mathbb{R}^{N\times 1}$ is the sub-vector of the dual variable $\boldsymbol{\sigma} \in \mathbb{R}^{QN\times 1}$ which corresponds to the local image $\mathbf{x}_q$. The resulting updates of each variable according to CADMM formulation are provided hereinafter in detail.

Update of x (Local Images)

Let $\mathbf{x_G}^{(k)}$ and $\boldsymbol{\sigma}^{(k)}$ denote the values of $\mathbf{x_G}$ and $\boldsymbol{\sigma}$ after the k^{th} iteration. Since $\mathcal{L}(\mathbf{x}, \mathbf{x_G}, \boldsymbol{\sigma})$ in (2.10) is decomposable with respect to $\mathbf{x}_q$, the updated $\mathbf{x}^{(k+1)}$ can be obtained by updating all local images $\mathbf{x}_q^{(k+1)}$ for $q = 1, \ldots, Q$ in parallel as

$$\begin{aligned}\mathbf{x}_q^{(k+1)} &= \arg\min_{\mathbf{x}_q} \mathcal{L}\left(\mathbf{x}_q; \mathbf{x_G}^{(k)}, \boldsymbol{\sigma}_q^{(k)}\right) \\ &= \arg\min_{\mathbf{x}_q} \left\{ \frac{\mu}{2} \left\|\mathbf{y}_q - \mathbf{A}_q\mathbf{x}_q\right\|_2^2 + \boldsymbol{\sigma}_q^{(k)^T}\mathbf{x}_q + \frac{\beta}{2}\left\|\mathbf{x}_q - \mathbf{x_G}^{(k)}\right\|_2^2 \right\},\end{aligned} \tag{2.11}$$

The problem in (2.11) is differentiable with respect to $\mathbf{x}_q$ and the $(k+1)^{\text{th}}$ update can be obtained in a closed-form by letting $\nabla_{\mathbf{x}_q}\mathcal{L} = \mathbf{0}$ resulting in

$$\mathbf{x}_q^{(k+1)} = \left(\mu\mathbf{A}_q^H\mathbf{A}_q + \beta\mathbf{I}_N\right)^{-1}\left(\mu\mathbf{A}_q^H\mathbf{y}_q + \beta\mathbf{x_G}^{(k)} - \boldsymbol{\sigma}_q^{(k)}\right), \tag{2.12}$$

Note that the inverse in (2.12) is possible since $\left(\mu\mathbf{A}_q^H\mathbf{A}_q + \beta\mathbf{I}_N\right)$ is a positive definite matrix.

Update of $\mathbf{x_G}$ (Global Image)

For the global image update, following the ADMM framework, we consider the following

$$\begin{aligned}\mathbf{x_G}^{(k+1)} &= \arg\min_{\mathbf{x_G}} \mathcal{L}\left(\mathbf{x_G}; \mathbf{x}^{(k+1)}, \boldsymbol{\sigma}^{(k)}\right) \\ &= \arg\min_{\mathbf{x_G}} \left\{ \lambda\left\|\mathbf{x_G}\right\|_1 + \sum_{q=1}^{Q}\boldsymbol{\sigma}_q^{(k)^T}\mathbf{x_G} + \frac{\beta}{2}\sum_{q=1}^{Q}\left\|\mathbf{x}_q^{(k+1)} - \mathbf{x_G}\right\|_2^2 \right\}.\end{aligned} \tag{2.13}$$

This objective function above involves information from all Q clusters and is not decomposable with respect to $\mathbf{x_G}$. It further involves a non-differentiable function $\|\mathbf{x_G}\|_1$. Thus, it can neither be parallelized nor solved in a closed form like (2.11). As a result, it is more suitable for the global image update to be carried out in a central processor after collecting local updates calculated at the distributed clusters. Moreover, for the subsequent update of local images, the global image needs to be broadcast to all the clusters. Alternatively, if the global image update were to be carried out at distributed clusters, a fully meshed communication network would be needed to exchange all local updates among the Q clusters. Later in Section 2.3.3, we will show how to solve (2.13) in the central node.

Update of $\boldsymbol{\sigma}$ (Dual Variable)

After updating the global image, the dual variable can be updated by

$$\boldsymbol{\sigma}^{(k+1)} = \boldsymbol{\sigma}^{(k)} + \beta \left(\mathbf{x}^{(k+1)} - \mathbf{1}_Q \otimes \mathbf{x}_{\mathbf{G}}^{(k+1)} \right), \tag{2.14}$$

The Kronecker product is used to replicate the global image to the same size as the vectors $\mathbf{x}$ and $\boldsymbol{\sigma}$. Since (2.14) is decomposable, it can be carried out in parallel as well as local images' updates. Instead, it is more convenient for the dual variable to be updated in the central node subsequent to the update of global images. Then, both updates are broadcast to the distributed clusters for the next update of local images.

2.3.2 Sharing ADMM (SADMM)

Under this formulation, we impose a different constraint on the optimization problem to explore a different relationship between the local images and the global image. The constraint is set such that the reconstructed global image is the sparse average of all local images. Accordingly, the problem becomes

$$\begin{aligned} \underset{\mathbf{x},\mathbf{x_G}}{\arg\min} \quad & \sum_{q=1}^{Q} \frac{\mu}{2} \left\| \mathbf{y}_q - \mathbf{A}_q \mathbf{x}_q \right\|_2^2 + \lambda \left\| \mathbf{x_G} \right\|_1 \\ s.t. \quad & \bar{\mathbf{x}} - \mathbf{x_G} = \mathbf{0} \end{aligned} \tag{2.15}$$

where $\bar{\mathbf{x}} = \sum_{q=1}^{Q} \mathbf{x}_q$ contains the sum of magnitudes of local images. Note that the size of constraints is reduced to the size of a single image instead of Q images in the consensus formulation. The nomenclature stems from the constraint above since the global image is considered a shared combination of all local images. We can again write the constraint of (2.15) in the form of the constraint in (2.6) by having $\mathbf{G} = [\mathbf{I}_N, \mathbf{I}_N, \cdots \mathbf{I}_N]$ of size $N \times QN$, $\mathbf{u} = \mathbf{x}$, $\mathbf{H} = -\mathbf{I}_N$, $\mathbf{z} = \mathbf{x_G}$, and $\mathbf{c} = \mathbf{0}$.

The augmented Lagrangian of (2.15) can then be written as

$$\mathcal{L}\left(\mathbf{x}, \mathbf{x_G}, \boldsymbol{\sigma}\right) = \left\{ \sum_{q=1}^{Q} \frac{\mu}{2} \left\| \mathbf{y}_q - \mathbf{A}_q \mathbf{x}_q \right\|_2^2 + \lambda \left\| \mathbf{x_G} \right\|_1 + \langle \boldsymbol{\sigma}, \bar{\mathbf{x}} - \mathbf{x_G} \rangle + \frac{\beta}{2} \left\| \bar{\mathbf{x}} - \mathbf{x_G} \right\|_2^2 \right\}. \tag{2.16}$$

Note that since the number of constraints is reduced, the dual variable $\boldsymbol{\sigma}$ has a size $N \times 1$ instead of $QN \times 1$ as in CADMM. Next, we provide the variable updates according to the SADMM formulation.

Update of x (Local Images)

Unlike the consensus case, the augmented Lagrangian function (2.16) is not directly decomposable into Q terms because of the variable $\bar{\mathbf{x}}$ inside the augmented quadratic term which contains the sum of local images. However, we show here that it is still possible to solve for each local image variable $\mathbf{x}_q$ in parallel. Similar to (2.11), we use the values of $\mathbf{x}_{\mathbf{G}}^{(k)}$ and $\boldsymbol{\sigma}_q^{(k)}$ in order to solve for $\mathbf{x}_q$ at the $(k+1)^{\text{th}}$ iteration. However, since we have also $\bar{\mathbf{x}}$ in (2.16), we keep the values of all other local images ($\mathbf{x}_i^{(k)}\ \forall i \neq q$) fixed. Let $\bar{\mathbf{x}}_q^{(k)} = \sum_{(i\neq q)} \mathbf{x}_i^{(k)} = \bar{\mathbf{x}}^{(k)} - \mathbf{x}_q^{(k)}$. Consequently, the q^{th} local image update can be obtained by

$$\begin{aligned}
\mathbf{x}_q^{(k+1)} &= \arg\min_{\mathbf{x}_q} \mathcal{L}\left(\mathbf{x}_q; \bar{\mathbf{x}}_q^{(k)}, \mathbf{x}_{\mathbf{G}}^{(k)}, \boldsymbol{\sigma}^{(k)}\right) \\
&= \arg\min_{\mathbf{x}_q} \left\{ \frac{\mu}{2} \left\| \mathbf{y}_q - \mathbf{A}_q \mathbf{x}_q \right\|_2^2 + \boldsymbol{\sigma}^{(k)^T} \mathbf{x}_q + \frac{\beta}{2} \left\| \mathbf{x}_q + \bar{\mathbf{x}}_q^{(k)} - \mathbf{x}_{\mathbf{G}}^{(k)} \right\|_2^2 \right\} \\
&= \arg\min_{\mathbf{x}_q} \left\{ \frac{\mu}{2} \left\| \mathbf{y}_q - \mathbf{A}_q \mathbf{x}_q \right\|_2^2 + \boldsymbol{\sigma}^{(k)^T} \mathbf{x}_q + \frac{\beta}{2} \left\| \mathbf{x}_q + \bar{\mathbf{x}}^{(k)} - \mathbf{x}_q^{(k)} - \mathbf{x}_{\mathbf{G}}^{(k)} \right\|_2^2 \right\}
\end{aligned} \tag{2.17}$$

Now similar to (2.11), the problem in (2.17) is fully differentiable with respect to $\mathbf{x}_q$ and the $(k+1)^{\text{th}}$ update can be obtained in the closed-form

$$\mathbf{x}_q^{(k+1)} = \left(\mu \mathbf{A}_q^H \mathbf{A}_q + \beta \mathbf{I}_N\right)^{-1} \left(\mu \mathbf{A}_q^H \mathbf{y}_q + \beta \left(\mathbf{x}_{\mathbf{G}}^{(k)} - \bar{\mathbf{x}}_q^{(k)}\right) - \boldsymbol{\sigma}^{(k)}\right). \tag{2.18}$$

From (2.18), we can observe that in SADMM, the q^{th} local image update requires the previous state $\mathbf{x}_q^{(k)}$, the sum of the previous updates of all other local images $\bar{\mathbf{x}}^{(k)}$, the global image update $\mathbf{x}_G^{(k)}$, and the dual variable update $\boldsymbol{\sigma}_q^{(k)}$. This suggests the need for extra memory with respect to CADMM to track the previous state at each cluster. Additionally, the distributed clusters will need to receive each other updates. This can be broadcast by the central node subsequent to the update of the global image and dual variables. The central node will have such values regardless since they are needed for the global image update. Although the exchanged information between the central node and the distributed clusters in SADMM seems to be more than CADMM, the size of those variables to be exchanged is still less than CADMM by a factor of $(Q+2)/3$ due to the reduced size of the dual variable in SADMM. This significantly reduces communication bandwidth requirements between the central node and the sensors, especially for a large number of distributed sensors.

Update of $\mathbf{x_G}$ (Global Image)

Similar to the global image update in Section 2.3.1, after collecting the updates of the local image from the distributed sensors, the global image update for the sharing formulation is obtained by minimizing the augmented Lagrangian with respect to $\mathbf{x_G}$ as follows

$$\mathbf{x}_{\mathbf{G}}^{(k+1)} = \arg\min_{\mathbf{x_G}} \left\{ \lambda \left\| \mathbf{x_G} \right\|_1 + \frac{\beta}{2} \left\| \mathbf{x_G} - \bar{\mathbf{x}}^{(k+1)} \right\|_2^2 + \boldsymbol{\sigma}^{(k)^T} \mathbf{x_G} \right\}. \tag{2.19}$$

Again, we here assume that both the global image and the dual variable are calculated at the central node. As a result, the sum of the local images $\bar{\mathbf{x}}^{(k)}$ is calculated directly at the central node following the local updates collection needed for the global image update. The solution of (2.19) will be detailed in Section 2.3.3.

Update of $\boldsymbol{\sigma}$ (Dual variable)

The dual variable update then is a straightforward step of the ADMM algorithm which is

$$\boldsymbol{\sigma}^{(k+1)} = \boldsymbol{\sigma}^{(k)} + \beta \left(\bar{\mathbf{x}}^{(k+1)} - \mathbf{x}_{\mathbf{G}}^{(k+1)} \right) \tag{2.20}$$

Deferring the study of the imaging performance of each formulation to the next section, it suffices to summarize that SADMM provides an alternative processing architecture with respect to CADMM in which: 1) extra memory is needed at the distributed clusters for local image updates, 2) communication overhead between the distributed clusters and the central node is reduced by a factor of $(Q+2)/3$ due to the difference in the size of the constraints. In both CADMM and SADMM, local images can be updated in parallel at each cluster node and communicated back to the central node. The central node in turn updates both the global image and the dual variable. Subsequently, both the global image and dual variable updates are broadcast back to the distributed clusters in the case of CADMM in addition to the sum of the previous local images in the case of SADMM in order to calculate the next local image updates. Other comparisons and performance metrics such as image reconstruction quality and convergence rate will be provided later in Section 2.4.

2.3.3 Solution Techniques

Considering the above formulations, in this section, we provide the techniques used to solve the sub-problems for local images and global image updates. Additionally, we provide the stopping criteria adopted to terminate both algorithms. Lastly, we show

how to obtain the phases of complex-valued local images prior to ADMM iterations.

Variable Updates

The updates of local images (2.12) and (2.18), employ a matrix inversion in a closed-form solution. However, due to the large size of the problem, it needs to be solved iteratively using a numerical procedure. In particular, we carry out the inversion in the local update using the Conjugate Gradient (CG) method [83]. Being a numerical method, the output of CG is a complex-valued image since both the measurements $\mathbf{y}_q$ and the forward model $\mathbf{A}_q$ are complex. However, the optimization is carried out over the real-valued magnitude of the images where the phase of the images is included in the measurement matrix. Therefore, subsequent to the update of the local image using CG, a projection of the resulting complex image on the real positive orthant is applied to obtain the magnitude of the local image. This projection implicitly states that the phase of the complex-valued output of CG is regarded as a numerical phase error.

On the other hand, global image updates, (2.13) and (2.19), require solving a Least Absolute Shrinkage and Selection Operator (LASSO)-like optimization problem which can be solved using a proximal gradient method. In our numerical experiments, we used the accelerated proximal gradient [84] to calculate the global image updates.

Stopping Criteria

Variable updates are repeated until termination which is decided upon comparing the values of the primal and dual residuals with their corresponding feasibility tolerances ϵ_{pri} and ϵ_{dual}, respectively.

Following the definitions of the residuals and the stopping criteria brought up in [72], let $\boldsymbol{\eta}_{pri}$ and $\boldsymbol{\eta}_{dual}$ denote the primal and dual residuals, respectively. The dual residual is defined over the subsequent updates of the global image variable. Hence, it is the same for both CADMM and SADMM. Accordingly, at the k^{th} iteration, the dual residual for both formulations is given by

$$\boldsymbol{\eta}_{dual}^{(k)} = \beta \left(\mathbf{x}_{\mathbf{G}}^{(k+1)} - \mathbf{x}_{\mathbf{G}}^{(k)} \right). \tag{2.21}$$

On the other hand, the primal residual measures the constraint satisfaction and takes a different form in the two formulations. For CADMM, the primal residual is given by

$$\boldsymbol{\eta}_{pri}^{(k)} = \mathbf{x}^{(k+1)} - \mathbf{1}_Q \otimes \mathbf{x}_{\mathbf{G}}^{(k+1)}. \tag{2.22}$$

Similarly, in SADMM the primal residual is

$$\boldsymbol{\eta}_{pri}^{(k)} = \bar{\mathbf{x}}^{(k+1)} - \mathbf{x}_{\mathbf{G}}^{(k+1)}. \tag{2.23}$$

The feasibility tolerances can be chosen based on an absolute tolerance ϵ_{abs} and a relative tolerance ϵ_{rel}. Similar to the primal and dual residuals, the feasibility tolerances indicate non-identical definitions depending on the formulation due to the different constraints. In CADMM, they are given by

$$\begin{aligned} \epsilon_{pri} &= \sqrt{QN}\ \epsilon_{abs} + \epsilon_{rel}\ \max\left\{ \left\|\mathbf{x}^{(k)}\right\|_2, \sqrt{Q}\left\|\mathbf{x}_{\mathbf{G}}^{(k)}\right\|_2 \right\} \\ \epsilon_{dual} &= \sqrt{QN}\ \epsilon_{abs} + \epsilon_{rel}\left\|\boldsymbol{\sigma}^{(k)}\right\|_2. \end{aligned} \tag{2.24}$$

Likewise, for SADMM, feasibility tolerances are:

$$\begin{aligned} \epsilon_{pri} &= \sqrt{N}\ \epsilon_{abs} + \epsilon_{rel}\ \max\left\{ \left\|\bar{\mathbf{x}}^{(k)}\right\|_2, \left\|\mathbf{x}_{\mathbf{G}}^{(k)}\right\|_2 \right\} \\ \epsilon_{dual} &= \sqrt{N}\ \epsilon_{abs} + \epsilon_{rel}\left\|\boldsymbol{\sigma}^{(k)}\right\|_2. \end{aligned} \tag{2.25}$$

Lastly, for both CADMM and SADMM, the algorithm is terminated either when a defined maximum number of iterations is reached or when both the ensuing inequalities are satisfied

$$\begin{aligned} \left\|\boldsymbol{\eta}_{pri}^{(k)}\right\|_2 &\leqslant \epsilon_{pri} \\ \left\|\boldsymbol{\eta}_{dual}^{(k)}\right\|_2 &\leqslant \epsilon_{dual}, \end{aligned} \tag{2.26}$$

where the variables in the above inequalities are calculated according to the definitions of the corresponding quantities (2.21)-(2.25).

Phase Matrix $\boldsymbol{\Theta}$

As mentioned earlier, we assume that the phase of local images is already provided prior to carrying out the optimization algorithms. Our proposed imaging methods can be considered partially non-coherent imaging methods since the phases are only used within the data-fidelity term in the objective function. Thus, a coarse estimated phase of local images is sufficient for our algorithms to perform satisfactorily. Therefore, we use the phase of the images obtained by backprojection for each cluster as an estimate of the phase of local images. Accordingly, for each cluster q, the diagonal matrix containing

the phase of all pixels of its local image is constructed as

$$\mathbf{\Theta}_q = \mathrm{diag}\left\{\exp\left(j[\angle(\mathbf{A}_q^H \mathbf{y}_q)]\right)\right\}. \tag{2.27}$$

Finally, a summary of the steps of CADMM and SADMM in addition of a schematic to depict the parallel implementation scheme are reported in Algorithm 1 and Figure 2.2, respectively.

Figure 2.2: Illustration of the parallel implementation scheme of CADMM and SADMM.

2.4 Performance Evaluation

In this section, we validate and evaluate the performance of the algorithms proposed in Section 2.3 to reconstruct radar images using distributed sensor clusters. To achieve this goal, we use the publicly available Civilian-Vehicles Dome (CVDomes) dataset which offers simulated scattering data of civilian vehicle facet models. Although the dataset is originally intended to simulate circular synthetic aperture radars, a particular configuration of WSAR, it can also be used to simulate a mono-static distributed radar sensors system.

First, we give a brief introduction to the dataset and its parameters. Consequently, we define the performance metrics used in our evaluation to compare both algorithms. Finally, we evaluate our algorithms on three different scenarios of practical relevance for several applications. The scenarios are realized by different combinations of full/limited views and full/limited bandwidth measurements as we will show later in this section.

2.4.1 Data-Set Introduction

CVDomes dataset contains simulated electromagnetic high-frequency scattering data of ten civilian vehicles. For each model, an X-band mono-static scattering is simulated

Algorithm 1 Widely Distributed Radar Imaging using CADMM and SADMM

Input:

- The measurement matrices $\left\{\mathbf{A}_q\right\}_{q=1}^{Q}$
- Measured echos signal $\left\{\mathbf{y}_q\right\}_{q=1}^{Q}$
- Hyperparameters μ and β
- Absolute and relative tolerances ϵ_{abs} and ϵ_{rel}

Initialize:

- Local images $\left\{\hat{\mathbf{x}}_q^{(0)} = \mathbf{0}\right\}_{q=1}^{Q}$
- Global image $\hat{\mathbf{x}}_{\mathbf{G}}^{(0)} = \mathbf{0}$
- Dual variable $\boldsymbol{\sigma}^{(0)} = \mathbf{0}$
- The iteration counter $k = 0$

while stopping criterion (2.26) not satisfied **do**

1. Update $\left\{\hat{\mathbf{x}}_q^{(k+1)}\right\}_{q=1}^{Q}$ locally in parallel
   - CADMM $\rightarrow$ (2.12)
   - SADMM $\rightarrow$ (2.18)
2. Update $\hat{\mathbf{x}}_{\mathbf{G}}^{(k+1)}$ in central node
   - CADMM $\rightarrow$ (2.13)
   - SADMM $\rightarrow$ (2.19)
3. Update $\left\{\boldsymbol{\sigma}_q^{(k+1)}\right\}_{q=1}^{Q}$ in central node
   - CADMM $\rightarrow$ (2.14)
   - SADMM $\rightarrow$ (2.20)
4. $k \leftarrow k + 1$.

end while

Output: $\hat{\mathbf{x}}_{\mathbf{G}}$

in a far-field scenario. Scattered waves are simulated with full polarization over an azimuth extent of 360° where 16 viewing angles per degree of azimuth are considered. Similarly, data are simulated over the range of elevation angles from 30° to 60°. For each tuple of azimuth and elevation viewing angles, 512 frequency samples of complex-valued scattering coefficients centered at 9.6 GHz and spanning a bandwidth of approximately

5.35 GHz are provided. The range information of those frequency measurements is compressed already resulting in what is usually referred to as phase history.

2.4.2 Performance Metrics

As discussed in the previous section, the difference in problem formulation between CADMM and SADMM has induced slightly different system implementation features in terms of memory requirements and communication bandwidth. Additionally, to compare the performance of the proposed algorithms, the following aspects are considered.

1. Convergence rate: it can be assessed by the number of iterations needed to reach the stopping criteria that is defined identically for both algorithms.

2. Computational complexity: the main computational burden of both algorithms lies in the local image updates (2.12) and (2.18), where the matrix inversion term is present. Due to their large size, the measurement matrices $\mathbf{A}_q$ are realized through matrix operators based on two-dimensional non-uniform Fast Fourier transform (2D Non-uniform Fast Fourier Transform (NuFFT)) [85]. Moreover, the inversion step is carried out numerically using CG as mentioned earlier. Thus, while the complexity of both algorithms seems to be equivalent, the convergence of CG highly depends on the other variables in the update formulas (2.12) and (2.18). As a result, the comparison solely in terms of the number of iterations is not indicative since a single iteration in each of the algorithms may realize a different cost. Accordingly, computational complexity can be measured by calculating the total processing time spent until termination.

3. Image reconstruction quality: the dataset does not contain a reference image with which a comparison can be made in order to evaluate the quality of reconstructed images. Correspondingly, we use image entropy as a quantitative metric to assess the image quality as a measure of its sharpness or constituent randomness. The smaller the image entropy the sharper the reconstructed image and vice versa. After clipping the image intensity values which are beyond a certain dynamic range in the dB scale, the image is translated to the grayscale so the entropy is calculated in bits. Consequently, a randomly generated image would have an entropy equal to or close to 8 bits. Additionally, as a subjective measure of image quality, the images reconstructed utilizing full aperture and full bandwidth measurement could act as a visual reference for the other scenarios when the aperture and/or the bandwidth measurements are reduced.

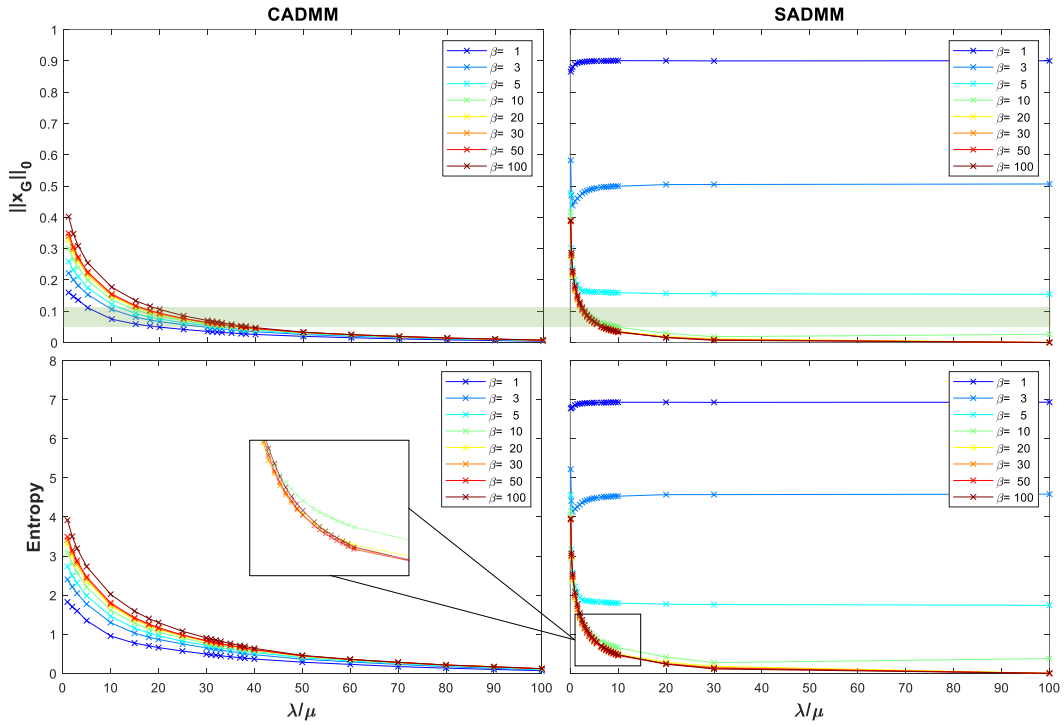

Figure 2.3: Hyperparameters sweep for 'Jeep99' data (FVFB): **Top row:** Normalized sparsity, **Bottom row:** Image entropy.

2.4.3 Experiments

In this subsection, we demonstrate the imaging results of CADMM and SADMM using the simulated data of two different vehicle models differing in type and geometry. The first is of a Jeep Cherokee (SUV) 'Jeep99', while the second is of a Toyota Tacoma (Pick-up) 'Tacoma'. We consider image reconstruction utilizing the dataset according to the following scenarios:

1. Full aperture views measurements: for a general validation of both algorithms, the full 360° aperture measurements of the entire available bandwidth are considered.

2. Full views and limited bandwidth measurements: limited frequency samples of the full aperture measurements are considered for image reconstruction realizing a typical use case of WSAR imaging.

3. Limited views and limited bandwidth measurements: assuming a distributed system of radar sensors illuminating the scene according to a Time-Division Multiplexing (TDM) scheme, limited frequency samples of limited aperture measurements are considered for image reconstruction.

For all experiments, measurements are taken at a fixed elevation angle of 30° and with 'HH' polarization. Moreover, all measurements are impaired with a white Gaussian noise realizing a SNR of 15 dB. A fine grid of 256 cells in both range and cross-range directions (7 meter-long each) is used resulting in a total number of $N = 65536$ pixels. Additionally, images are reconstructed considering an elevated image plane at 1 meter from the ground level. This renders the projection of layover-ed elements to be mostly contained within the vehicle's outlines and permits a better visual interpretation.

The choice of μ, β, and λ for both CADMM and SADMM is made through a parameter sweep guided by normalized image sparsity and image entropy as performance metrics. The normalized sparsity considered is the percentage of the non-zero pixels in the image. Hyperparameters used to reconstruct the illustrated images throughout this section are those that guarantee a similar degree of sparsity for both CADMM and SADMM images at a lower entropy value. Also, we tried to pick the parameters where β is as close as possible in both methods for a fair comparison of convergence rates. Given the considered scene size and typical dimensions of a vehicle, a sparsity level around the range of $5\% - 10\%$ is considered in our experiments based on the scenario and the vehicle. Needless to say, parameter sweep analysis is conducted separately for each dataset and each scenario. It is worth mentioning that, for a given β, the ratio λ/μ can be automatically selected given the desired sparsity range as will be discussed in Chapter 4. However, since an empirical search for β is needed at almost exact sparsity levels for both CADMM and SADMM, a parameter sweep would facilitate finding more accurate parameters for the sake of comparison. An example of image sparsity and image entropy versus different parameters is shown for the first scenario. For later experiments, such analysis will be omitted for brevity. CADMM and SADMM are run for a maximum number of 100 iterations while the feasibility tolerances ϵ_{abs} and ϵ_{rel} are both set to 10^{-2}. Scenario-specific parameters and reconstructed images of all the aforementioned experiments are provided and discussed in the sequel.

Full Views - Full Bandwidth (FVFB)

Using the full 360° azimuth extent and the full bandwidth of the dataset (approximately equal to 5.35 GHz), we reconstruct the images of the two vehicles to validate our proposed methods and show their superior reconstruction quality with respect to the conventional BP method. The reconstructed images in this experiment can also be used as a reference for subsequent scenarios when images are reconstructed using limited views and/or limited bandwidth measurements. As mentioned previously, to avoid anisotropic scattering over the large angular azimuth extent, it is divided into

sub-apertures (clusters) at which the isotropic scattering assumption is valid. The angular width of a cluster has a double-faced effect on the imaging performance trading-off between angular resolution and homogeneous target scattering. The wider the cluster the better the resolution while the scattering becomes anisotropic. Therefore, in this experiment, the cluster width is chosen to maximize the imaging performance in a balanced manner. We use a cluster width of 5° within which we assume the targets exhibit isotropic scattering.

As anticipated earlier, we perform a hyperparameter sweep over different values of β and λ/μ to obtain the values that provide good reconstruction quality given the image sparsity level. The sparsity level is decided based on the assumed dimensions of the observed targets relative to the scene dimensions. They are set separately for each scenario due to the dissimilarities of aperture size and signal bandwidth utilized, hence images exhibit a different resolution in each scenario. Figure 2.3 shows the normalized sparsity level and entropy of the reconstructed image of the 'Jeep99' dataset versus the varying parameters of β and λ/μ for both SADMM and CADMM. The desired sparsity level range is highlighted with a light green color in the figure. As expected, the higher the ratio λ/μ, the more sparse the reconstructed images for both the algorithms and naturally the lower the entropy. This is true except for some values of β for which SADMM optimization does not converge to a sparse solution. Such divergence for those parameters can be seen from the corresponding entropy values which indicate the reconstruction of random images. Moreover, beyond those values of β, reconstructed images using the same λ/μ ratio exhibit similar sparsity levels and attain close values for entropy as shown in the magnified part of Figure 2.3.

To first demonstrate the performance of both methods, CADMM and SADMM images reconstructed considering two different sparsity levels are shown for the 'Jeep99' dataset in Figure 2.4. The left column images have a normalized sparsity degree of 12% versus 5% for the images in the right column. For lower sparsity images, CADMM shows a sharp high-intensity reconstruction of the strong features of the vehicle such as edges and ceiling structure, and a lower-intensity reconstruction of the weaker features such as the projection of the tire wheels. On the other hand, SADMM images manifest an average intensity of the different parts of the vehicle resulting in less sharp images. While the behavior is maintained for the images at higher sparsity, the weaker features are further suppressed in the images of both methods. Moreover, the images of both methods at a similar sparsity level have similar entropy values. This behavior is again confirmed by the reconstructed images of the 'Tacoma' vehicle. At a sparsity level of 10%, the reconstructed images of the two vehicles are shown in Figure 2.5 in addition to

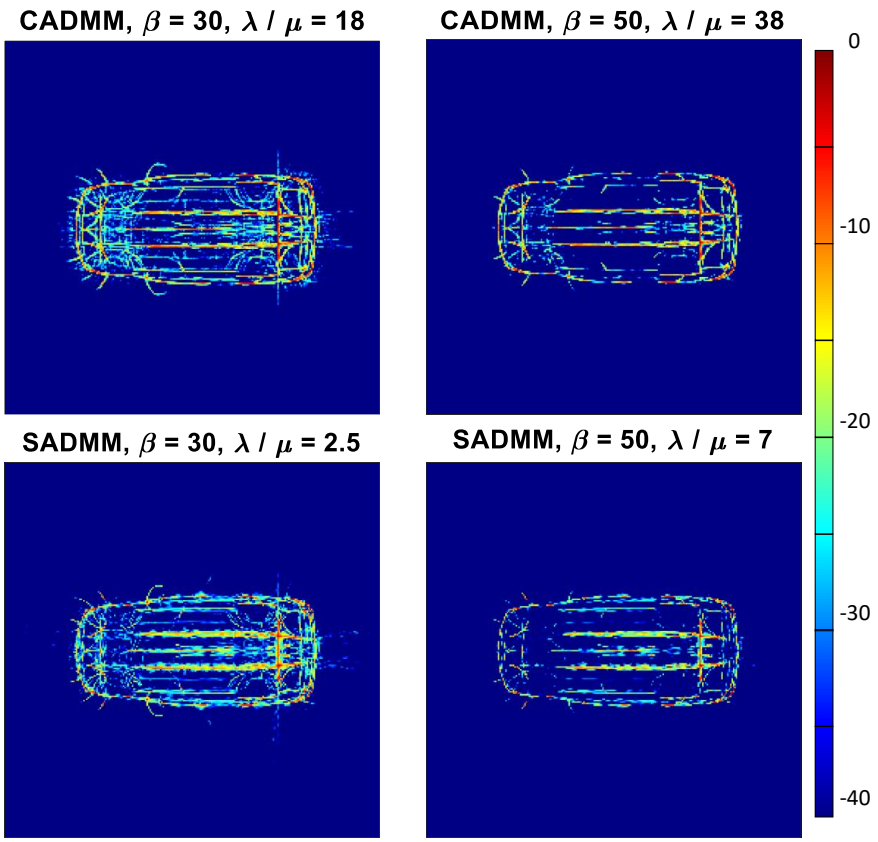

Figure 2.4: Jeep image reconstruction at different sparsity levels: **Left column:** 12%, **Right column:** 5%.

the images reconstructed through conventional back-projection averaged over all clusters. The red dots on the images show the angular aperture views which cover 360° in this experiment. Note that due to the abundance of the available bandwidth and the full aperture measurements, both CADMM and SADMM images have very high resolution and show the detailed structure of the imaged objects.

Additionally, the processing time until termination in SADMM is higher than CADMM. The numerical values of the parameters used in image reconstruction and the corresponding metrics are reported in Table 2.1 while the ratio between SADMM and CADMM processing time and number of iterations are reported in Table 2.2.

Full Views - Limited Bandwidth (FVLB)

In practice, the signal bandwidth of a SAR system is usually an order of magnitude less than the available bandwidth of the dataset. Thus, analyzing the performance of our proposed algorithms considering fewer bandwidth samples is of high interest and

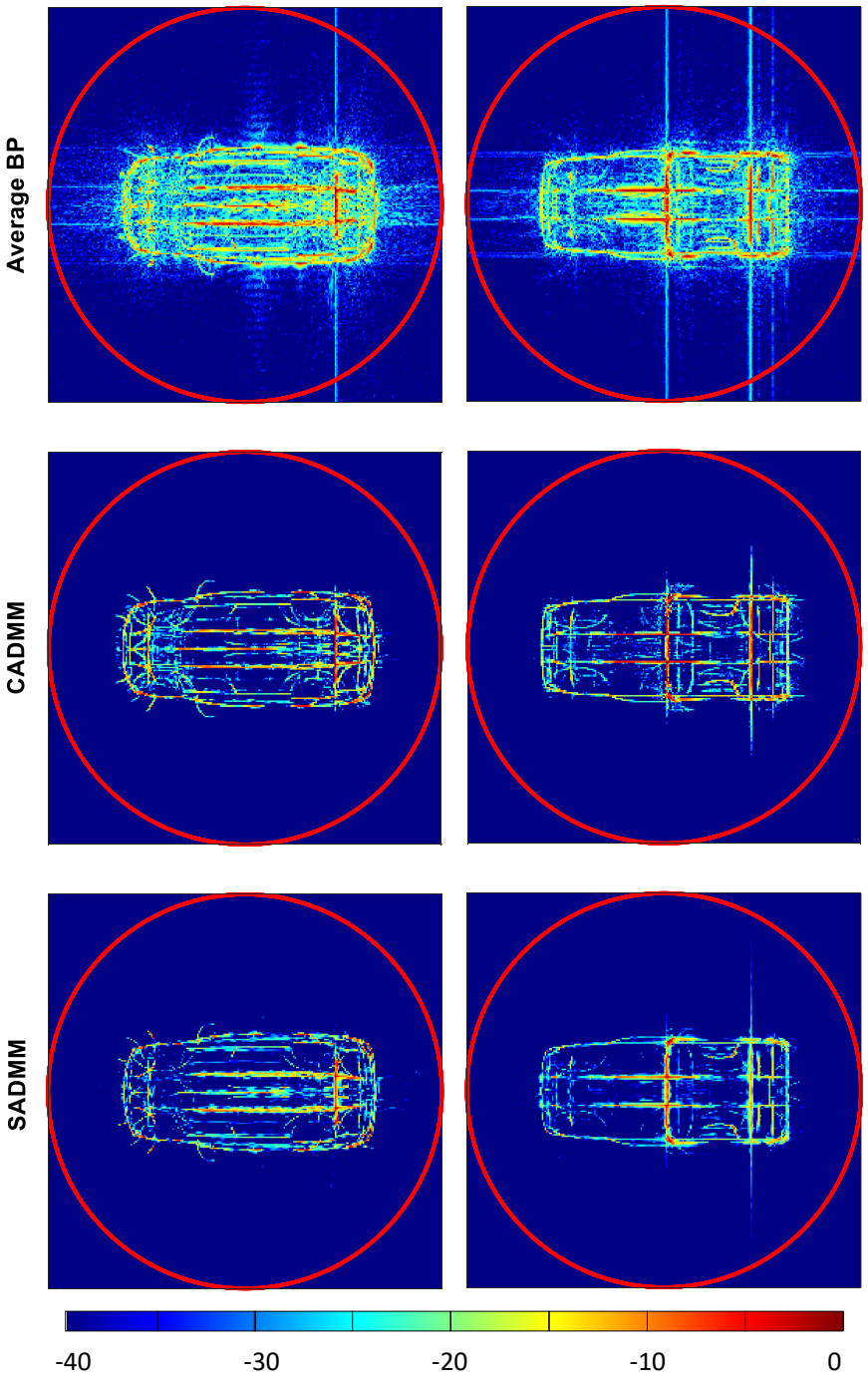

Figure 2.5: FVFB image reconstruction at sparsity level $\approx 10\%$, $Q = 72$ clusters, bandwidth $= 5.35$ GHz: **Left column:** Jeep Cherokee, **Right column:** Toyota Tacoma.

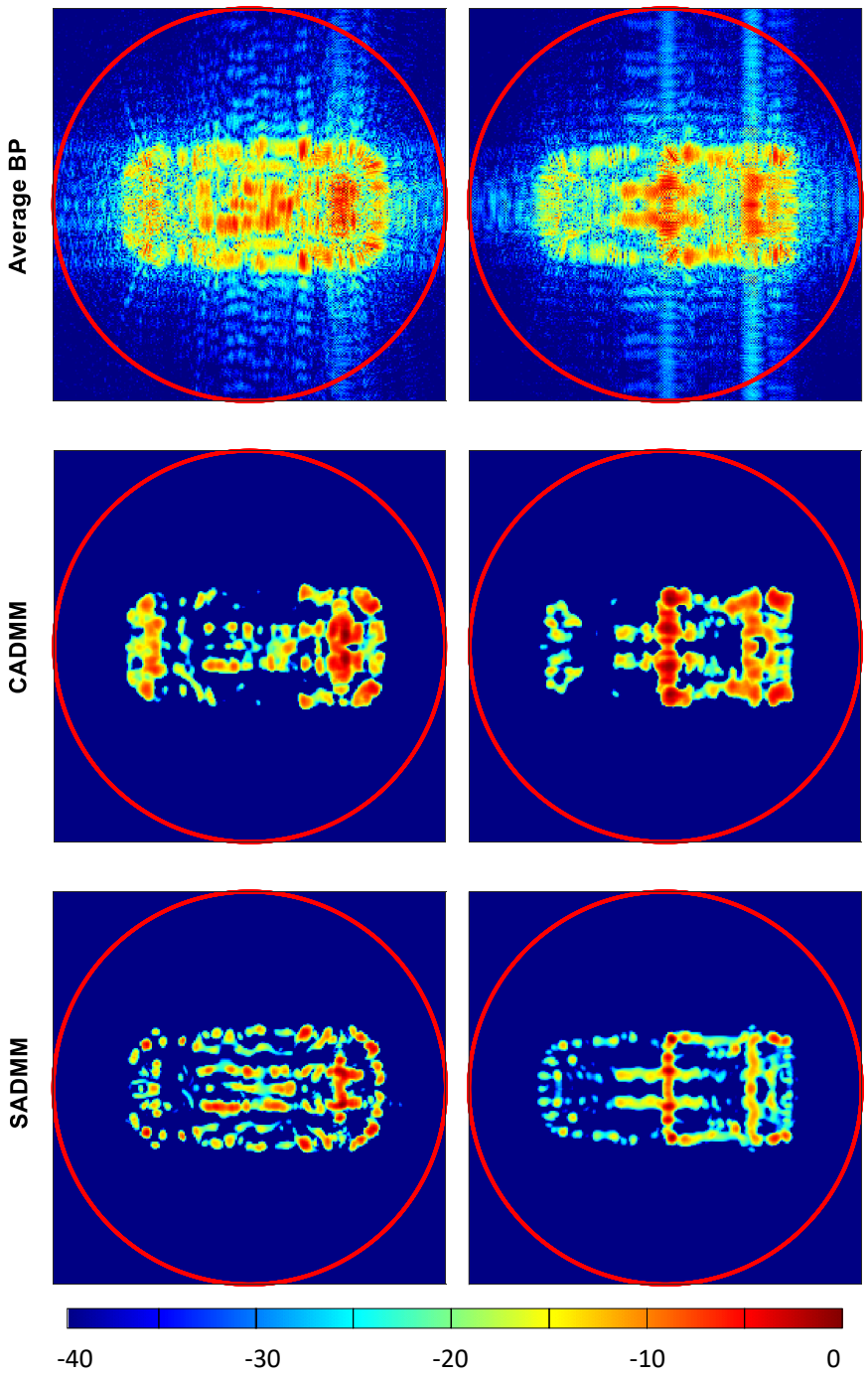

Figure 2.6: FVLB image reconstruction at sparsity level $\approx 10\%$, $Q = 72$ clusters, bandwidth $= 600$ MHz: **Left column:** Jeep Cherokee, **Right column:** Toyota Tacoma.

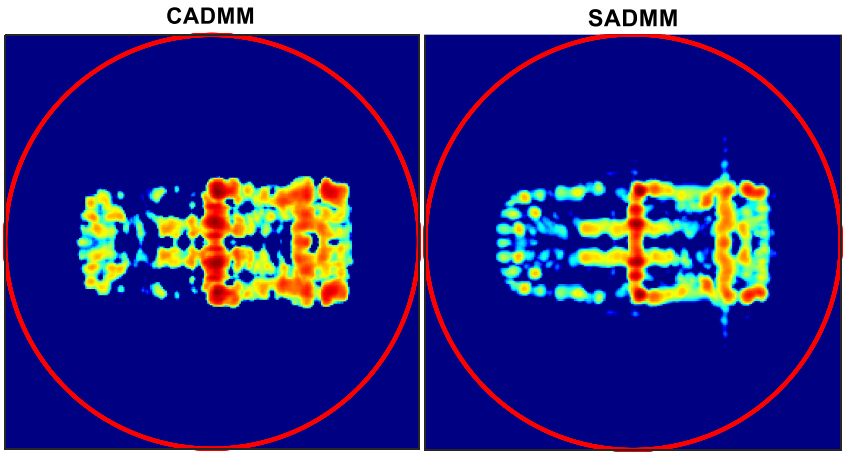

Figure 2.7: Low sparsity FVLB reconstruction of Toyota Tacoma (sparsity level $\approx 15\%$).

is a relevant use case in WSAR imaging. To realize a limited bandwidth measurement scenario, we utilized an equivalent of 600 MHz samples around the center frequency from the samples of phase history. In this experiment as well, SADMM images exhibit the property of higher averaging than that of concentrated intensity resulting from CADMM images as shown in Figure 2.6. This peculiarity makes it capable of capturing the true structure of the vehicles even with low bandwidth measurements when referring to the images in Figure 2.5 of the FVFB experiment. On the other hand, images reconstructed using CADMM have higher intensity around the strong reflectors and weaker or no intensity of the poorly reflective components of the vehicles; this is evident in the reconstructed images of both vehicles in Figure 2.6. For example, the crossing of the beams in the rear part of the 'Jeep99' data is localized and well identified with strong intensity in the SADMM image, while in the CADMM image, the same area exhibits only a strong intensity in a wider region. Similarly, in 'Tacoma' images, CADMM fails to capture the outline of the vehicle at this sparsity level and the strong trunk dominates the image. On the other hand, in the SADMM image, the vehicle outline appears while the trunk is being better identified. The depicted images have a sparsity level approximately equal to 10%. Note that by considering lower sparsity, images of both algorithms will increase the background intensity around the strong features without capturing the general structure of the object differently. An example is shown in Figure 2.7 where the images of the 'Tacoma' vehicle are reconstructed at a lower normalized sparsity level of about 15%. In summary, although CADMM images have similar entropy values as their SADMM counterparts at the same sparsity level, the latter provides a higher capability of capturing the structure of the observed targets given relatively low bandwidth measurements. The exact values of sparsity and entropy

for each image are reported in Table 2.1.

The superior performance of SADMM comes at the cost of increased computational complexity to reach convergence. This complexity is manifested through the higher number of iterations and the longer processing time required for SADMM to reconstruct the shown images. The ratio of these two quantities for SADMM and CADMM is depicted in Table 2.2.

Limited views - Limited Bandwidth (LVLB)

A mono-static distributed sensing scenario can be realized by considering far-field illumination with limited and narrow views of the full aperture measurements. In this experiment, we consider using the dataset to realize a system of distributed radar sensors in which the TDM scheme is used to illuminate the scene of interest where a single cluster transmits at a time. Consequently, in addition to the limited bandwidth measurements of 600 MHz introduced in the previous experiment, we further consider limited aperture measurements representing the views of distributed sensors. In particular, 16 clusters of 1° width each are uniformly distributed around the scene and considered as the viewing angles of the sensors. This number of clusters makes a realistic choice for the number of sensors where they cover only a span of about 4.4% of the full aperture measurements.

For this experiment, the reconstructed images of the two vehicles are shown in Figure 2.8. Similar to the previous experiment, SADMM captures both vehicles' structures better than CADMM. However, due to the limited aperture measurements, the artifacts present in the images of both methods are stronger. Increasing the sparsity would eliminate the artifacts but limit the reconstruction of the entire outline of the vehicles.

Of course, reconstructed images are view-dependent. However, the performance of both methods is the same when the different orientation of the sensors is considered. For example, the images reconstructed using another random orientation of views are shown in Figure 2.9. The images confirm the capability of SADMM to retain the original structure of the imaged target while CADMM has a better ability to diminish the artifacts. Similar to previous experiments, processing times for imaging using SADMM are higher than the time needed for CADMM. Finally, the parameters used to reconstruct the images in Figure 2.8 and the corresponding values of entropy and sparsity are reported in Table 2.1 while processing time and the number of iterations ratios are reported in Table 2.2.

Finally, to provide an additional comparison with the state-of-the-art, we reconstructed the images of 'Jeep99' using Least Squares (LS)-CS-Residual composite imaging [70]. Figure 2.10 depicts the performance of the LS-CS-Residual composite imaging

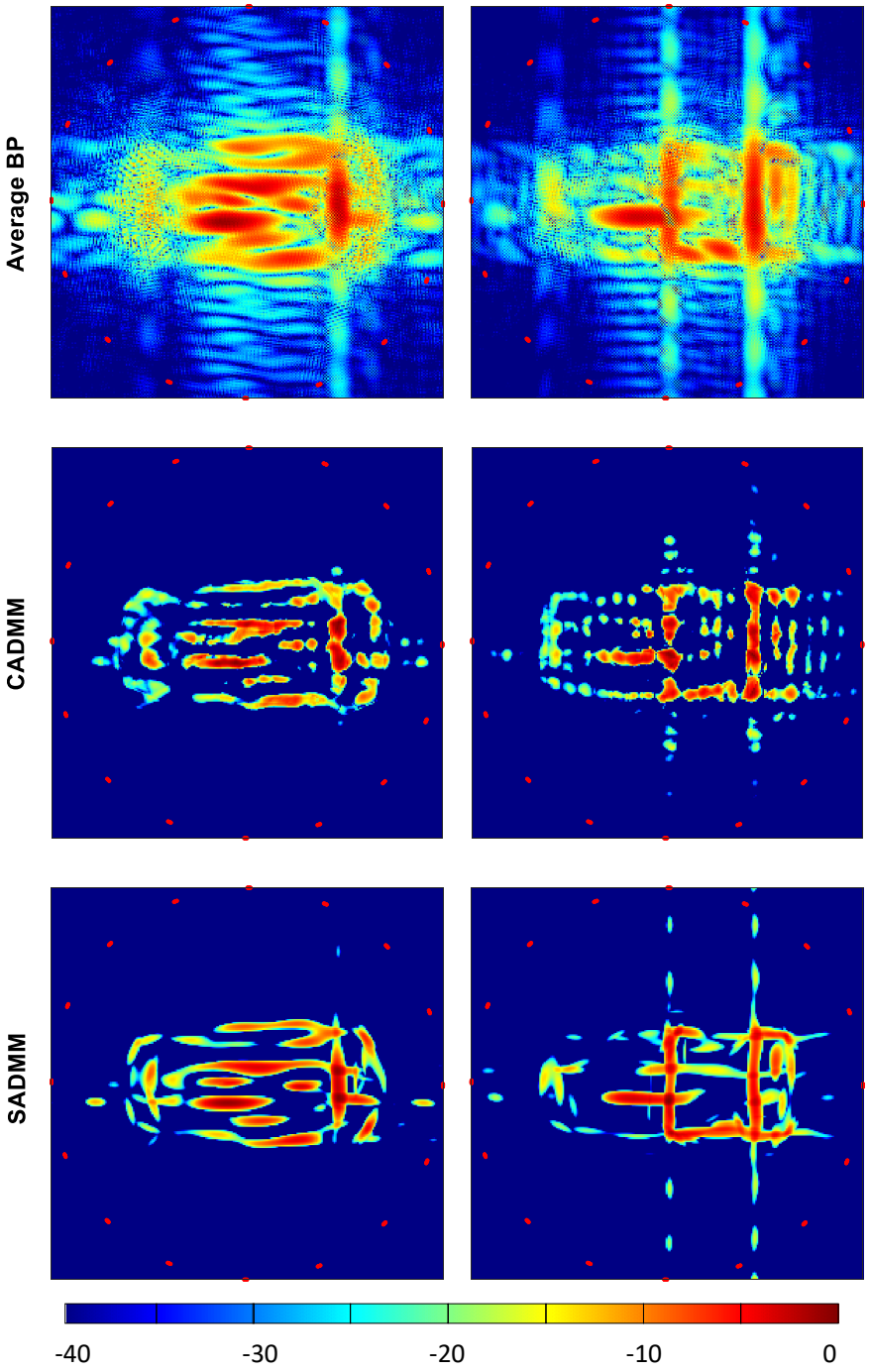

Figure 2.8: LVLB image reconstruction at sparsity level $\approx 10\%$, $Q = 16$ clusters, bandwidth $= 600$ MHz: **Left column:** Jeep Cherokee, **Right column:** Toyota Tacoma.

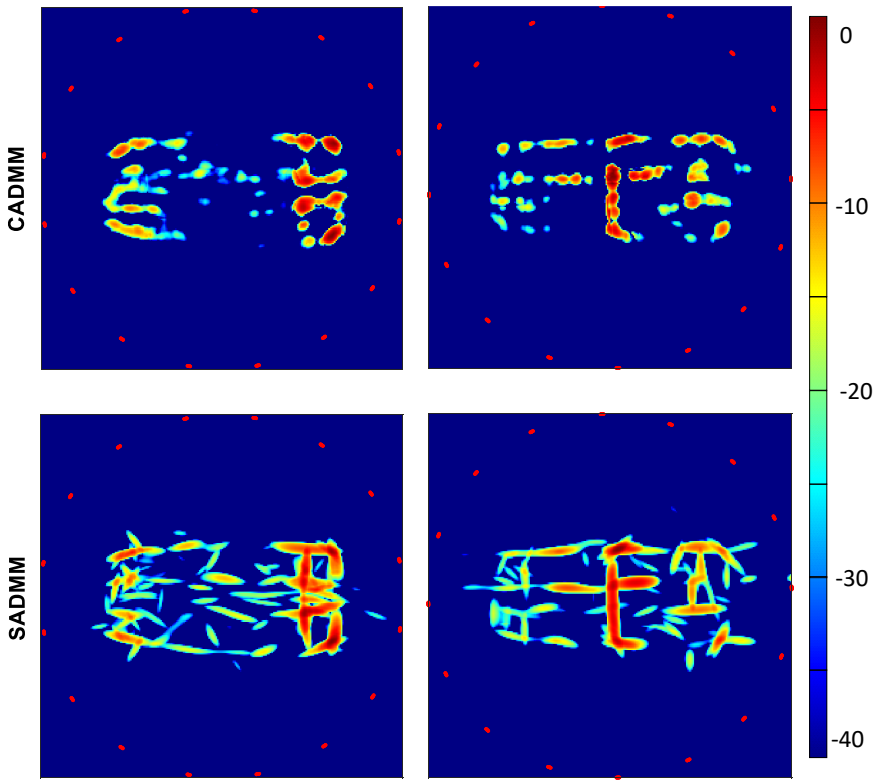

Figure 2.9: LVLB reconstruction with different random sensors orientation: **Left column:** Jeep Cherokee, **Right column:** Toyota Tacoma.

in the three scenarios combining different aperture and bandwidth ranges. Comparing with the results of CADMM and SADMM in Figs. 2.5, 2.6 and 2.8, shows the limitations of using the methods of DCS and/or methods that rely on the evolution of RCS when the support of the underlying image sequence is not highly overlapped as the case of the dataset we use. This is particularly evident in the scenarios of limited views and/or limited bandwidth, where LS-CS-Residual imaging almost fails completely.

Additionally, since the update of each local image depends on the estimate of the preceding image in the sequence in LS-CS-Residual imaging, the implementation is forced to be sequential. This is another advantage of our proposed methods where local images can be updated in parallel at each iteration. This is further highlighted by the significantly contrasted computing times of our proposed method versus LS-CS-Residual which are reported in Table 2.3. The reported values serve also as an indication of the absolute computing time of our proposed methods, in addition to the relative values reported in Table 2.2. All numerical experiments were carried out on a node of the High-Performance Computing (HPC) facility at the University of Luxembourg [86].

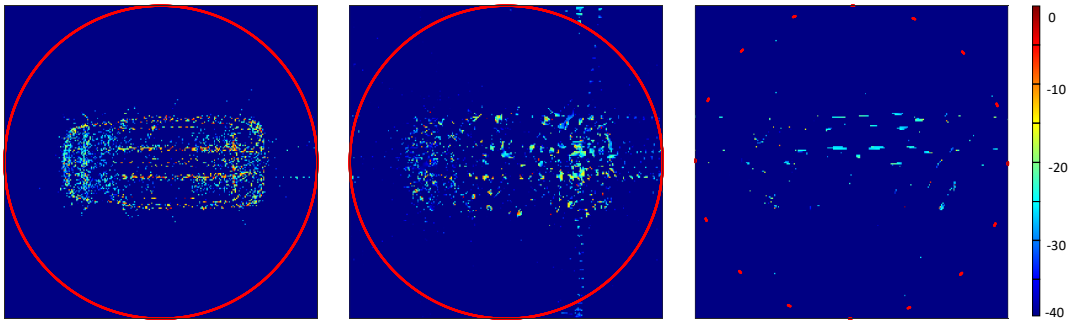

Figure 2.10: LS-CS-Residual imaging results for 'Jeep99' data for the three experiments: **Left:** FVFB, **Middle:** FVLB, **Right:** LVLB.

The node utilized has an AMD EPYC 7H12 64-Core processor CPU at 2.6 GHz and 256 GB of physical memory and is running a MATLAB Version: R2021a. By leveraging a multi-core processor, we implemented both CADMM and SADMM to run local updates in parallel but were not able to realize a similar implementation for LS-CS-Residual composite imaging.

Table 2.1: Summary of parameters used in the experiments and corresponding metrics

		FVFB		FVLB		LVLB	
		CADMM	SADMM	CADMM	SADMM	CADMM	SADMM
(β, λ/μ)	Jeep	(30,18)	(30,2.5)	(30,16)	(30,1.4)	(10,1.25)	(20,0.4)
	Tacoma	(30,25)	(30,2.5)	(30,24)	(50,1.8)	(10,1.75)	(20,0.65)
Sparsity	Jeep	0.100	0.102	0.104	0.102	0.100	0.098
	Tacoma	0.096	0.10	0.097	0.098	0.099	0.103
Entropy	Jeep	1.24	1.25	1.27	1.26	1.25	1.22
	Tacoma	1.19	1.24	1.20	1.21	1.24	1.26

To summarize, in the first experiment where a plenitude of measurements in both aperture and bandwidth is available, both CADMM and SADMM are capable of reconstructing detailed and super-resolution images of the observed targets far surpassing the conventional methods. On the other hand, in the latter experiments where measurements are limited in aperture and/or bandwidth, SADMM exhibits superior performance over CADMM in terms of capturing the structure of the target and reconstructing smoother images. Although they have similar entropy in all cases, the depicted images reconstructed by both algorithms show a clear visual advantage of SADMM by reference to the images of full measurements. Such higher quality comes at the expense of higher

Table 2.2: Relative convergence and complexity

	FVFB		FVLB		LVLB	
Ratio SADMM/CADMM	Iterations	Time	Iterations	Time	Iterations	Time
Jeep	1.41	1.46	3.45	2.11	1.45	2.19
Tacoma	1.41	1.52	3.13	2.06	1.51	2.04

Table 2.3: Absolute computing times using proposed methods vs. LS-CS-Residual for 'Jeep99' (in minutes)

	FVFB	FVLB	LVLB
CADMM	5.1562	1.2264	0.4066
SADMM	7.5389	2.5879	0.8902
LS-CS-Residual	21.1528	16.1970	3.9681

computational costs. Surprisingly, in terms of convergence and complexity, SADMM fell behind the most in the second experiment where the full aperture measurements with limited bandwidth are considered. This can be owed to the fact that SADMM has fewer degrees of freedom than CADMM which with the full aperture measurements requires less than a third of SADMM iterations to reach convergence.

2.5 Conclusion

In this chapter, we introduced a novel approach for widely distributed radar imaging based on the ADMM framework. We imposed a sparsity prior on a defined global image, assumed to represent an aggregate view of the scene. Subsequently, we designed two formulations based on CADMM and SADMM to mathematically stipulate the relationship between the images of individual sensors and the defined global image. We provided solutions to these formulations as iterative algorithms, which are flexible and amenable to implementation on a distributed architecture.

Through several experiments, we demonstrated the performance of the proposed algorithms and showcased their significant edge over conventional methods in terms of reconstructed image quality. Furthermore, we illustrated that SADMM outperforms CADMM, especially under limited measurements, yielding images that better highlight the structure and shape of observed objects. However, this advantage comes with slower convergence and longer processing times.

As demonstrated in the experiments, the presented algorithms are applicable in many

scenarios of distributed radar systems and WSAR imaging. The proposed approach paves the way for various formulations and further developments. These formulations could involve imposing different priors on the global image or establishing alternative associations with the images of individual sensors to further enhance the image quality depending on the intended application.

Chapter 3

Imaging Acceleration

In this chapter, a heuristic approach aimed at accelerating the convergence of the ADMM formulations presented in Chapter 2 is introduced. The method is based on gradually eliminating already converged pixels according to a predetermined criterion. In addition to reducing running time, this accelerated implementation offers decreased computational complexity and lower communication costs between sensors during iterative updates. By gradually learning the scene support throughout the iterative reconstruction, the proposed method focuses on the image portion containing scattering targets and updates the sub-images accordingly.

3.1 Introduction

In Chapter 2, we proposed ADMM-based algorithms to reconstruct the image of a scene observed by widely distributed radar sensors. ADMM optimization framework gives a distributed processing regime for measurements collected through a distributed architecture. Additionally, different from the composite imaging methods, the proposed algorithms jointly reconstruct and fuse the images of each sub-aperture into one global image of the scene. Nevertheless, when high reconstruction accuracy is considered, ADMM methods may suffer a noticeable slow convergence [72]. This is also evident from the computational complexity and running time values reported in Tables 2.3 and 2.2. To overcome this issue, in this chapter, we propose modified versions of CADMM and SADMM that further leverage the scene sparsity and gradually learn the approximate support of the scene. This allows reducing the size of the problem during optimization by focusing the reconstruction on the sub-images containing the scene support. Such adjustable size reduction lowers the problem complexity and significantly decreases its running time in addition to accelerating the convergence rate.

In contrast to other methods that rely on the partial known support of the scene [65, 70], we adaptively learn the support of the scene during the iterations of the algorithm starting from the full scene size. This differs from the methods used in these works which initially threshold the BP image to acquire knowledge about the scene support and consequently remain tight with it throughout the image reconstruction process.

3.2 Signal Model

We consider a system where Q radar sensors are distributed around a scene of interest. Each radar sensor is equipped with a Uniform Linear Array (ULA) comprising M antenna elements. All antenna elements are utilized for receiving the reflected echo, while the transmission is conducted through a single element. A mono-static configuration is assumed, employing a TDM scheme among the sensors. Specifically, each sensor receives the reflected echo from the scene only during the slot associated with its own transmission time. During its transmission, each sensor's transmitting antenna emits a LFM chirp of rate α and a bandwidth BW to illuminate the scene. Subsequently, the reflected echo is received by the multiple receiving antenna elements on that sensor.

In a non-widely distributed architecture, the sensors observe the scene within a rather narrow angular extent. Thus, the isotropic scattering model of scene reflectivity is usually adopted; this permits modeling the scene reflectivity with a single variable for all sensors. Moreover, it allows the imaging task to be carried out using the measurements from all sensors jointly and obtain a reflectivity image of the scene. However, in our case where the sensors are widely separated, the scene is observed over a large angular extent. Consequently, the isotropic scattering assumption cannot be satisfied across all the sensors. Accordingly, the isotropic assumption is only considered within a single sensor (sub-aperture) which leads to a system model that comprises Q reflectivity images. As a result, individual treatment of each sensor's measurements is usually considered necessitating a fusion-embraced imaging algorithm or sub-aperture-aware joint imaging algorithm for a global reflectivity image reconstruction.

Under the above-mentioned model and assumption, we denote with the subscript q a single sensor where $q = 1 \dots Q$ and with the superscript m a single antenna element where $m = 1 \dots M$. When considering a 2D scene discretized into N pixels where each pixel is assumed to contain a single reflective target, the frequency domain reflected echo

y_q^m after demodulating and de-chirping can be modeled as

$$y_q^m(\omega) = \sum_{n=1}^{N} x_{q,n} a_{q,n} \delta\left(\omega - \Delta\omega_{n,q}\right) e^{\left(-j\frac{2\pi f_c}{c} d_q (m-1)\sin\theta_{q,n}\right)}, \tag{3.1}$$

where $x_{q,n}$ is the complex reflectivity coefficient of the n^{th} pixel, $a_{q,n}$ is the propagation coefficient, ω is the angular frequency, $\Delta\omega_{n,q} = \frac{4\pi\beta}{c} R_{q,n}$ is the angular frequency shift due to the scattering by a target at the n^{th} pixel located at a distance $R_{q,n}$ from the q^{th} sensor, $\theta_{n,q}$ is the aspect angle of the n^{th} pixel with respect to the q^{th} sensor, f_c is the center frequency of the transmitted signal, and d_q is the intra-element spacing between the antenna elements of the q^{th} sensor. The signal model in (3.1) assumes that a pixel is located at the same distance and angle from all the antennas belonging to the same sensor and its reflectivity coefficient is frequency independent. By uniformly sampling the echo signal at K frequency bins, the matrix form of (3.1) is given by

$$\begin{aligned}
&\mathbf{y}_q^m = \mathbf{A}_q^m \tilde{\mathbf{x}}_q + \mathbf{n}_q^m \in \mathbb{C}^{K\times 1},\\
&\mathbf{A}_q^m = [\boldsymbol{\alpha}_1^m, \boldsymbol{\alpha}_2^m, \cdots, \boldsymbol{\alpha}_N^m] \in \mathbb{C}^{K\times N},\\
&\boldsymbol{\alpha}_n^m = \begin{bmatrix}
a_{q,n}\delta\left(\omega_1 - \Delta\omega_{n,q}\right) e^{\left(-j\frac{2\pi f_c}{c}(m-1)d_q\sin\theta_{q,n}\right)}\\
a_{q,n}\delta\left(\omega_2 - \Delta\omega_{n,q}\right) e^{\left(-j\frac{2\pi f_c}{c}(m-1)d_q\sin\theta_{q,n}\right)}\\
\vdots\\
a_{q,n}\delta\left(\omega_K - \Delta\omega_{n,q}\right) e^{\left(-j\frac{2\pi f_c}{c}(m-1)d_q\sin\theta_{q,n}\right)}
\end{bmatrix},
\end{aligned} \tag{3.2}$$

where $\boldsymbol{\alpha}_n^m \in \mathbb{C}^{K\times 1}$, $\tilde{\mathbf{x}}_q$ is the vector contains the scene reflectivity coefficients with respect to the q^{th} sensor, $\mathbf{A}_q^m$ is the measurement matrix for the m^{th} antenna element of the q^{th} sensor, $\mathbf{n}_q^m$ denotes the additive noise, error from model imperfections, measurement error, etc. After a vertical stacking of $\left\{\mathbf{y}_q^m\right\}_{m=1}^{M} \rightarrow \mathbf{y}_q$, $\left\{\mathbf{A}_q^m\right\}_{m=1}^{M} \rightarrow \mathbf{A}_q$, and $\left\{\mathbf{n}_q^m\right\}_{m=1}^{M} \rightarrow \mathbf{n}_q$, the whole measurement vector for the q^{th} sensor is given by

$$\mathbf{y}_q = \mathbf{A}_q \tilde{\mathbf{x}}_q + \mathbf{n}_q \in \mathbb{C}^{KM\times 1}. \tag{3.3}$$

3.3 Problem Formulation

On-grid radar imaging usually involves a scene with a number of pixels much larger than the number of measurements i.e. $N >> KM$. Due to that and especially when sub-aperture methods are considered, where each sensor's echo is processed separately, the inverse problem of (3.3) becomes severely ill-posed. A reasonable solution can be ob-

tained through regularized least square estimation leveraging prior knowledge about the scene such as sparsity or smoothness. Following the formulations presented in Chapter 2, the problem of reconstructing the image of the scene was posed as the minimization of the sum of quadratic data fidelity terms for the local images across all sensors plus the l_1-norm of a global image subject to the consensus and sharing constraints. Below we provide again the proposed CADMM and SADMM formulations for completeness.

CADMM Formulation:

$$\begin{aligned} \min_{\mathbf{x}_1,\mathbf{x}_2,\cdots,\mathbf{x}_Q,\mathbf{x}_\mathbf{G}} \quad & \sum_{q=1}^{Q} \frac{\mu}{2} \left\|\mathbf{y}_q - \mathbf{A}_q\mathbf{x}_q\right\|_2^2 + \lambda \left\|\mathbf{x}_\mathbf{G}\right\|_1 \\ s.t. \quad & \mathbf{x}_\mathbf{G} - \mathbf{x}_q = 0 \quad q = 1 \dots Q, \end{aligned} \tag{3.4}$$

SADMM Formulation:

$$\begin{aligned} \min_{\mathbf{x},\mathbf{x}_\mathbf{G}} \quad & \sum_{q=1}^{Q} \frac{\mu}{2} \left\|\mathbf{y}_q - \mathbf{A}_q\mathbf{x}_q\right\|_2^2 + \lambda \left\|\mathbf{x}_\mathbf{G}\right\|_1 \\ s.t. \quad & \bar{\mathbf{x}} - \mathbf{x}_\mathbf{G} = \mathbf{0} \end{aligned} \tag{3.5}$$

where $\mathbf{x}_\mathbf{G}$ is defined as the magnitude of the global image, $\mathbf{x}_q$ is the magnitude of the complex local image of the q^{th} sensor, $\bar{\mathbf{x}} = \sum_{q=1}^{Q} \mathbf{x}_q$ contains the sum of magnitudes of local images, μ and λ are hyperparameters to trade-off the data fidelity and regularization terms.

The problems in (3.4) and (3.5) are solved by iteratively updating the local images and the global image in an alternating fashion according to ADMM iterative steps [72], as presented in Sections 2.3.1 and 2.3.2. While our proposed methods proved effective in reconstructing high-resolution scene images and reducing artifacts, they suffer from slow convergence and high computational complexity. In the subsequent section, we introduce modified versions of these algorithms, referred to as Accelerated CADMM (ACADMM) and Accelerated SADMM (ASADMM). These modified versions maintain similar image reconstruction quality to the original algorithms but exhibit improved convergence rates and lower computational complexity.

3.4 Accelerated ADMM Imaging

Given the assumption of scene sparsity, a reflected echo is essentially a linear combination of a small subset of columns from the measurement matrix. Therefore, in addition to regularization, further exploitation of scene sparsity may be achievable by adaptively reconstructing sub-images of the scene during ADMM iterations. In both CADMM and

SADMM, the primal residual, which measures constraint satisfaction, tends to converge faster than the dual residual, which reflects the residual of successive iterations of the global image. This observation implies that local images converge over the scene support more rapidly than the convergence of the global image. Consequently, we can initially reconstruct the full scene and then concentrate on regions containing targets based on the convergence of the primal residual. The selection of the focus region can be determined by a criterion that tracks the convergence of individual pixels, calculating the relative error across past iterations, and focusing on regions with errors below a defined tolerance threshold.

To this end, we introduce Q matrices $\{\mathbf{P}_q\}_{q=1}^{Q}$ with dimensions $N_q \times N$, acting as selector operators at the q^{th} sensor to extract a sub-image containing N_q pixels from the full scene image. $\mathbf{P}_q$ are binary matrices constructed such that each row selects a single element (pixel) of the scene. Therefore, the rows represent element selector vectors $\mathbf{e}_j^T \in \{0,1\}^N$ defined as $\left[\mathbf{e}_j\right]_i = \delta_{j-i}$ and $j \in \{1,\ldots,N\}$.

Initially, when considering the full scene at the algorithm's outset, all Q matrices are the identity matrix $\mathbf{I}_N$, with $Nq = N$. Each pixel is selected only once within each sensor's sub-image, meaning that for two distinct rows j and l in $\mathbf{P}_q$ where $j \neq l$, the corresponding vectors $\mathbf{e}_j^T$ and $\mathbf{e}_l^T$ select the j^{th} and l^{th} pixels of the scene, respectively.

With these defined operators, the modified problem formulations are presented in the following sections.

3.4.1 Accelerated Consensus ADMM

After considering sub-image selector matrices, the problem in (3.4) becomes

$$\begin{aligned} \min_{\mathbf{x}_1,\mathbf{x}_2,\cdots,\mathbf{x}_Q,\mathbf{x}_\mathbf{G}} \quad & \sum_{q=1}^{Q} \frac{\mu}{2} \left\| \mathbf{y}_q - \mathbf{A}_q \tilde{\mathbf{P}}_q \mathbf{x}_q \right\|_2^2 + \lambda \left\| \mathbf{x}_\mathbf{G} \right\|_1 \\ s.t. \quad & \tilde{\mathbf{P}}_q(\mathbf{x}_\mathbf{G} - \mathbf{x}_q) = 0 \qquad q = 1 \ldots Q, \end{aligned} \tag{3.6}$$

where $\tilde{\mathbf{P}}_q = \mathbf{P}_q^T \mathbf{P}_q$ is an identity matrix of size $N \times N$ with some zero elements on the diagonal. The formulation in (3.6) suggests joint reconstruction of a global image of the scene imposing a consensus constraint among the different sub-images reconstructed by each sensor and the corresponding global sub-image. The augmented Lagrangian function of (3.6) is given by

$$\mathcal{L}\left(\{\mathbf{x}_q\}_{q=1}^{Q}, \mathbf{x_G}, \{\boldsymbol{\sigma}_q\}_{q=1}^{Q}\right) = \lambda\|\mathbf{x_G}\|_1 + \sum_{q=1}^{Q} \frac{\mu}{2}\left\|\mathbf{y}_q - \mathbf{A}_q\tilde{\mathbf{P}}_q\mathbf{x}_q\right\|_2^2 + \boldsymbol{\sigma}_q{}^T\tilde{\mathbf{P}}_q\left(\mathbf{x}_q - \mathbf{x_G}\right) + \frac{\beta}{2}\left\|\mathbf{x}_q - \mathbf{x_G}\right\|_{\tilde{\mathbf{P}}_q}^2, \tag{3.7}$$

where $\boldsymbol{\sigma}_q$ is the dual variable, β is the augmentation penalty parameter, and $\|.\|_{\mathbf{P}}$ denotes the weighted norm induced by a semidefinite matrix $\mathbf{P}$.

Similar to CADMM, we solve (3.6) by iteratively alternating the updates between local images $\{\mathbf{x}_q\}_{q=1}^{Q}$, global image $\mathbf{x_G}$, and the dual variables $\{\boldsymbol{\sigma}_q\}_{q=1}^{Q}$. However, since we consider an adaptive sub-image focusing during the algorithm, an update step for the matrices $\{\mathbf{P}_q\}_{q=1}^{Q}$ is introduced in our implementation. The update of each variable is discussed in detail here in the sequel.

Update of Local Images

As mentioned earlier, we consider the full scene initially in our variable updates, focusing gradually on sub-images containing the scattering targets. Initially, all $\{\mathbf{P}_q\}_{q=1}^{Q}$ are set to the identity matrix $\mathbf{I}_N$. Further, let $\hat{\mathbf{x}}_q = \mathbf{P}_q\mathbf{x}_q$ be the local image variable referring to the sub-image to be updated at the current iteration. Similarly, $\hat{\mathbf{A}}_q = \mathbf{A}_q\mathbf{P}_q^T$ is the measurement matrix containing the corresponding columns, and $\hat{\boldsymbol{\sigma}}_q = \mathbf{P}_q\boldsymbol{\sigma}_q$ is the dual variable of the corresponding sub-image. Having a decomposable augmented Lagrangian function with respect to local variables $\mathbf{x}_q$ allows for a parallel update of the local images. Accordingly, the q^{th} local sub-image update at the k^{th} iteration is obtained as

$$\begin{aligned}\hat{\mathbf{x}}_q^{(k+1)} &= \arg\min_{\mathbf{x}_q} \mathcal{L}\left(\mathbf{x}_q; \mathbf{x}_{\mathbf{G}}^{(k)}, \boldsymbol{\sigma}_q^{(k)}\right) \\ &= \arg\min_{\mathbf{x}_q}\left\{\frac{\mu}{2}\left\|\mathbf{y}_q - \mathbf{A}_q\tilde{\mathbf{P}}_q\mathbf{x}_q\right\|_2^2 + \hat{\boldsymbol{\sigma}}_q^{(k)^T}\hat{\mathbf{x}}_q + \frac{\beta}{2}\left\|\mathbf{x}_q - \mathbf{x}_{\mathbf{G}}^{(k)}\right\|_{\tilde{\mathbf{P}}_q}^2\right\}.\end{aligned} \tag{3.8}$$

The updated local images can be obtained in a closed form since the Lagrangian function is fully differentiable with respect to $\mathbf{x}_q$. Accordingly, $\hat{\mathbf{x}}_q^{(k+1)}$ in (3.8) can be obtained explicitly by setting $\nabla_{\mathbf{x}_q}\mathcal{L} = \mathbf{0}$, which gives

$$\hat{\mathbf{x}}_q^{(k+1)} = \left(\mu\hat{\mathbf{A}}_q^H\hat{\mathbf{A}}_q + \beta\mathbf{I}_{N_q}\right)^{-1}\left(\mu\hat{\mathbf{A}}_q^H\mathbf{y}_q + \beta\mathbf{P}_q\mathbf{x_G}^{(k)} - \hat{\boldsymbol{\sigma}}_q^{(k)}\right). \tag{3.9}$$

Update of Global Image

Following a collection of the updated local images (or sub-images), the global image update is obtained by minimizing the Lagrangian function (3.7) with respect to $\mathbf{x_G}$.

Accordingly, the update is achieved by solving the following problem

$$\begin{aligned}\mathbf{x_G}^{(k+1)} &= \arg\min_{\mathbf{x_G}} \mathcal{L}\left(\mathbf{x_G}; \{\hat{\mathbf{x}}_q^{(k+1)}\}_{q=1}^{Q}, \{\hat{\boldsymbol{\sigma}}_q^{(k)}\}_{q=1}^{Q}\right) \\ &= \arg\min_{\mathbf{x_G}} \left\{ \lambda \left\|\mathbf{x_G}\right\|_1 + \sum_{q=1}^{Q} \hat{\boldsymbol{\sigma}}_q^{(k)^T} \mathbf{P}_q \mathbf{x_G} + \frac{\beta}{2} \sum_{q=1}^{Q} \left\| \mathbf{x}_q{}^{(k+1)} - \mathbf{x_G} \right\|_{\tilde{\mathbf{P}}_q}^2 \right\}. \end{aligned} \tag{3.10}$$

Update of Dual Variables

After updating the global image, dual variables can also be updated at the central node since it already has all the updates of local images. Let $\boldsymbol{\sigma}$ and $\mathbf{x}$ denote the vectors stacking all the scaled dual variables $\boldsymbol{\sigma}_q$ and local images updates $\mathbf{x}_q^{(k+1)}$ for $q = 1, \ldots, Q$, respectively. The dual variable update can be obtained as:

$$\boldsymbol{\sigma}^{(k+1)} = \boldsymbol{\sigma}^{(k)} + \beta \left(\mathbf{x}^{(k+1)} - \mathbf{1}_Q \otimes \mathbf{x}_{\mathbf{G}}^{(k+1)} \right). \tag{3.11}$$

Update of Sub-image Selection Operators

ACADMM is based on adaptively reducing the scene size in the reconstruction process, focusing on sub-images containing targets while excluding regions devoid of scatterers. Each iteration considers a sub-image defined by the matrix $\mathbf{P}_q$ for each local image. As previously discussed, we assume that sparse areas of the scene converge faster than regions containing scattering targets, with convergence determined by the primal residual as defined in (2.22). Furthermore, this convergence can be monitored by tracking the relative error of each pixel individually. Accordingly, to update the matrix $\mathbf{P}_q$, we introduce a Sub-Image Selection Criterion (SSC) based on the average pixel relative error ζ over K_p previous iterations. For an updated local image $\mathbf{x}_q^{(k+1)}$ at the k^{th} iteration, ζ is defined as

$$\zeta(\{\mathbf{x}^{(i)}\}_{i=k_i}^{k}) = \frac{1}{K_p} \sum_{i=k_i}^{k} |\mathbf{x}^{(i)} - \mathbf{x}^{(i-1)}|, \tag{3.12}$$

where k_i is calculated as $\max(1, k - K_p)$. Consequently, ζ becomes a vector of the same size as the scene, containing the average pixel-wise relative errors over the previous K_p iterations. The sub-image for the next iteration is determined by comparing elements of ζ with a defined tolerance ϵ_p. Pixels corresponding to ζ elements above ϵ_p define the support of the image to be focused on in the next iteration, denoted by the set $\{J\}$, where its cardinality dictates the dimension of the sub-image N_q. Based on the elements of $\{J\}$, the matrix operator $\mathbf{P}_q$ is updated accordingly by activating the row selector vectors correspond to the indices in $\{J\}$.

Algorithm 2 provides a summary of the steps to execute the update of the selector matrices $\{\mathbf{P}_q\}_{q=1}^{Q}$. It is worth mentioning that according to the criterion in Algorithm 2, once a pixel gets out of the focused region, it is not considered again. Accordingly, updated $\mathbf{P}_q$ either keeps the same previous dimensions or gets smaller at each successive iteration.

Algorithm 2 *SSC* subroutine for $\mathbf{P}_q$ update

Input: $\left\{\mathbf{x}_q^{(i)}\right\}_{i=K_p}^{k}$, and ϵ_p

if $\left\|\boldsymbol{\eta}_{pri}^{(k)}\right\|_2 \leq \epsilon_{pri}$

1. $\zeta_q^k = \zeta(\{\hat{\mathbf{x}}_q^{(i)}\}_{i=K_p}^{k})$
2. $\{J\} \leftarrow \text{supp}(\zeta_q^k \geq \epsilon_p)$, $|J| = N_q$
3. $\mathbf{P}_q \leftarrow [\mathbf{e}_{J\{1\}}^T \mathbf{e}_{J\{2\}}^T \cdots \mathbf{e}_{J\{N_q\}}^T]^T$

end if
Output: $\mathbf{P}_q$

3.4.2 Accelerated Sharing ADMM

Similar to ACADMM, we utilize the selector operators $\{\mathbf{P}_q\}_{q=1}^{Q}$ to formulate the accelerated version of SADMM. Accordingly, the problem becomes the following

$$\begin{aligned} \underset{\mathbf{x}_1,\mathbf{x}_2,\cdots,\mathbf{x}_Q,\mathbf{x}_\mathbf{G}}{\arg\min} \quad & \sum_{q=1}^{Q} \frac{\mu}{2} \left\|\mathbf{y}_q - \mathbf{A}_q \tilde{\mathbf{P}}_q \mathbf{x}_q\right\|_2^2 + \lambda \left\|\mathbf{x}_\mathbf{G}\right\|_1 \\ s.t. \quad & \mathbf{x}_\mathbf{G} - \textstyle\sum_{q=1}^{Q} \tilde{\mathbf{P}}_q \mathbf{x}_q = \mathbf{0} \end{aligned} \tag{3.13}$$

where μ and λ are hyper-parameters to trade-off the data fidelity and l_1 regularization terms and $\tilde{\mathbf{P}}_q = \mathbf{P}_q^T \mathbf{P}_q$.

Following the same approach introduced in Section 3.4.1, the variable updates can be obtained by minimizing the augmented Lagrangian function in addition to updating the sub-image selector operators. Consequently, at the k^{th} iteration the variable updates are the following

Update of Local Images

$$\hat{\mathbf{x}}_q^{(k+1)} = \left(\mu \hat{\mathbf{A}}_q^H \hat{\mathbf{A}}_q + \beta \mathbf{I}_{N_q}\right)^{-1} \left(\mu \hat{\mathbf{A}}_q^H \mathbf{y}_q + \beta \left(\hat{\mathbf{x}}_\mathbf{G}^{(k)} - \sum_{q=1}^{Q} \mathbf{P}_q^{(k)} \hat{\mathbf{x}}_q^{(k)}\right) - \hat{\boldsymbol{\sigma}}^{(k)}\right) \tag{3.14}$$

Update of Global Image

$$\mathbf{x}_{\mathbf{G}}^{(k+1)} = \arg\min_{\mathbf{x_G}} \left\{ \lambda \left\| \mathbf{x_G} \right\|_1 + \frac{\beta}{2} \left\| \mathbf{x_G} - \bar{\mathbf{x}}^{(k+1)} \right\|_2^2 + \hat{\boldsymbol{\sigma}}^{(k)^T} \mathbf{x_G} \right\} \tag{3.15}$$

Update of Dual Variables

$$\hat{\boldsymbol{\sigma}}^{(k+1)} = \hat{\boldsymbol{\sigma}}^{(k)} + \beta \left(\bar{\mathbf{x}}^{(k+1)} - \mathbf{x}_{\mathbf{G}}^{(k+1)} \right) \tag{3.16}$$

Update of Sub-image Selection Operators

$$\mathbf{P}_q^{(k+1)} = SSC(\{\mathbf{x}_q^{(i)}\}_{i=K_p}^{k}, \epsilon_p) \tag{3.17}$$

where β is the augmented penalty parameter, $\hat{\mathbf{x}}_q = \mathbf{P}_q \mathbf{x}_q$, $\hat{\mathbf{A}}_q = \mathbf{A}_q \mathbf{P}_q^T$, $\hat{\boldsymbol{\sigma}}$ is the dual variable with the support of the average of all sub-images $\bar{\mathbf{x}}$, and SSC_S is the subroutine to obtain the updates of the selector matrices detailed in Algorithm 2 where K_p and ϵ_p are input parameters for testing convergence that are the number of previous iterations considered and tolerance error, respectively.

3.4.3 Solution Techniques

The local image updates in (3.9) and (3.9) involve a matrix inversion that can be carried out directly or iteratively through methods like conjugate gradient descent algorithm [83] in case the problem size is large. Local updates can be carried out in parallel in the distributed sensors exploiting the computation capability that is usually available at these sensors. Additionally, since only a sub-image is being updated in subsequent iterations, the dimension of this matrix is reduced from $N \times N$ to $N_q \times N_q$ hence a complexity reduction by a factor of $(N/N_q)^3$ is achieved.

On the other hand, since the global image updates in (3.10) and (3.14) involves the non-differentiable term $\lambda \left\| \mathbf{x_G} \right\|_1$, its solution cannot be found in a closed form and is obtained using methods such as accelerated proximal gradient [84] which is used in our implementation. Carrying out the global image update in a central processing node is the only plausible choice for the system architecture since the collection of all local updates is needed and an iterative method is used.

Note that $\boldsymbol{\eta}_{pri}$ is the primal residual and ϵ_{pri} is the feasibility tolerance that are obtained based on the user-defined relative and absolute tolerances ϵ_{abs} and ϵ_{rel}, respectively. The reader may refer to Section 2.3.3 for the detailed calculations of these parameters.

With the accelerated versions provided in this section not only the computational complexity is reduced, but also the communication cost. It is owed to the fact that after

Algorithm 3 Widely Distributed Imaging using Accelerated ADMM

Input:

- Measurement matrices $\left\{\mathbf{A}_q\right\}_{q=1}^{Q}$
- Measured echo signals $\left\{\mathbf{y}_q\right\}_{q=1}^{Q}$
- Hyperparameters μ, λ and β
- Absolute and relative tolerances ϵ_{abs} and ϵ_{rel}
- Pixel convergence tolerance ϵ_p and pixel tracking iterations K_p

Initialize:

- Local images $\left\{\mathbf{x}_q^{(0)}\right\}_{q=1}^{Q} = \mathbf{0}$
- Global image ${\mathbf{x}_\mathbf{G}}^{(0)} = \mathbf{0}$
- Dual variable $\boldsymbol{\sigma}^{(0)} = \mathbf{0}$
- Sub-image selectors $\left\{\mathbf{P}_q\right\}_{q=1}^{Q} = \mathbf{I}_N$
- Iteration counter $k = 0$

while stopping criterion (2.26) not satisfied **do**

1. Update $\left\{\hat{\mathbf{x}}_q^{(k+1)}\right\}_{q=1}^{Q}$
   ACADMM $\rightarrow$ (3.9)
   ASADMM $\rightarrow$ (3.14)
2. Update ${\mathbf{x}_\mathbf{G}}^{(k+1)}$
   ACADMM $\rightarrow$ (3.10)
   ASADMM $\rightarrow$ (3.15)
3. Update $\boldsymbol{\sigma}^{(k+1)}$
   ACADMM $\rightarrow$ (3.11)
   ASADMM $\rightarrow$ (3.16)
4. Update $\left\{\mathbf{P}_q\right\}_{q=1}^{Q}$
   ACADMM $\rightarrow$ Algorithm 2
   ASADMM $\rightarrow$ Algorithm 2
5. $k \leftarrow k + 1$.

end while
Output: $\mathbf{x}_\mathbf{G}$

selecting sub-images, the communication exchange to the central node is necessitated only for sub-images updates with their corresponding index on the full scene while the remaining image parts are fixed and stored. A summary of accelerated ADMM image reconstruction steps is provided in Algorithm 3.

3.5 Numerical Results

In this section, we validate the performance of ACADMM and ASADMM on a simulated scene and compare them to CADMM and SADMM, respectively, in terms of image reconstruction quality and convergence rate. We run our simulations considering a synthetic radar scene that contains static targets of different shapes. We considered different targets geometry (point, line, cross) hence they manifest different scattering behavior over the viewing angles. To model the spatial diversity, targets are assumed to have their RCS as a function of the viewing angle. The aspect dependency functions for each target are illustrated in Figure 3.1. Using a fine grid with cells of size 0.05 m $\times$ 0.05 m, our scene is a region consisting of $Nc = 64 \times 64 = 4096$ pixels. To observe the scene, $Q = 4$ radar sensors with $M = 4$ receiving antennas are distributed around the scene; one per each side. Given the aspect-dependent behavior of targets, Figure 3.2 shows sensor orientation with respect to the scene and the Ground Truth (GT) image for each sensor. Individual GT images demonstrate the limitation of observing all targets by all sensors. Considering a single sensor transmitting at a time, a LFM with a sweeping bandwidth BW = 4 GHz around the center frequency $f_c = 60$ GHz is used for transmission at all sensors. The received signal is sampled at the Nyquist frequency and corrupted with white Gaussian noise where a SNR of 15 dB is considered.

For image reconstruction, we simulated both CADMM and ACADMM with hyperparameters $\mu = 5$, $\beta = 100$, and $\lambda = 200$ while the absolute and relative tolerance values are set as $\epsilon_{abs} = 10^{-4}$ and $\epsilon_{rel} = 10^{-2}$, respectively. $K_p = 5$ iterations are considered for ζ calculations and $\epsilon_p = 10^{-4}$ is set as threshold for Sub-Image Selection Criterion (SSC) in ACADMM implementation.

Reconstructed images using CADMM and ACADMM are shown in Figure 3.3 along with BP reconstruction and the composite GT image. The composite GT is defined as the sum of individual GT images; hence it represents the maximum attainable reconstruction. Images obtained by CADMM and ACADMM show the capability of both algorithms to reconstruct high-quality images of the scene with a slightly lower quality for the latter in terms of ghost targets and missed detection. However, as it can be seen from Figure 3.5, ACADMM requires almost half of the iterations needed for CADMM

to satisfy the same stopping criteria conditions. Moreover, ACADMM running time is found to be approximately 80% less than it is of CADMM due to the complexity reduction induced by updating only sub-images of the scene. The maximum sub-image size considered by ACADMM at each iteration is also reported in the background of Figure 3.5 where the values are normalized to the full scene size.

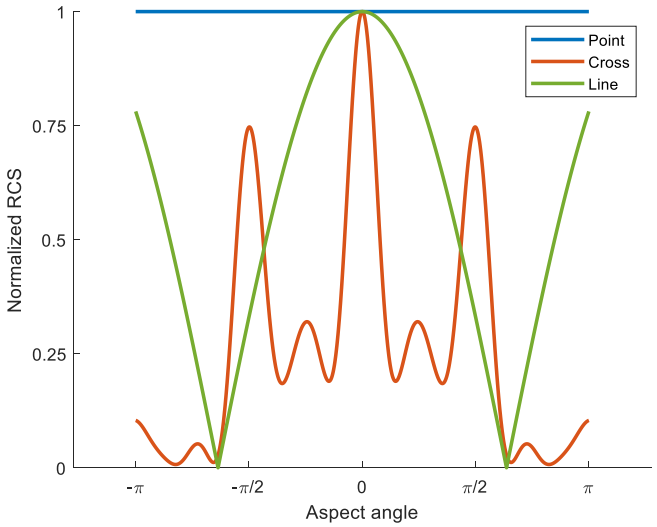

Figure 3.1: Targets RCS vs. Aspect angle

Similarly, for SADMM and ASADMM, we set the hyperparameters values as $\mu = 3$, $\beta = 100$, and $\lambda = 20$ while the absolute and relative tolerance values are set as $\epsilon_{abs} = 10^{-4}$ and $\epsilon_{rel} = 10^{-2}$, respectively. $K_p = 5$ iterations and $\epsilon_p = 10^{-5}$ error tolerance are considered for the subroutine SSC in ASADMM implementation.

Reconstructed images using SADMM and ASADMM are shown in Figure 3.4 along with BP reconstruction and the composite GT image. The composite GT is defined as the sum of individual GT images; hence it represents the maximum attainable reconstruction. Figure 3.4 shows the capability of both algorithms to reconstruct high-quality images of the scene with very similar performance. However, as it can be seen from Figure 3.6, ASADMM requires fewer iterations than needed for SADMM to satisfy the same stopping criteria conditions. Moreover, ASADMM running time is found to be approximately 80% less than SADMM due to the complexity reduction induced by updating only sub-images of the scene. The maximum sub-image size considered by ASADMM at each iteration is also reported in the background of Figure 3.6 where the values are normalized to the full scene size.

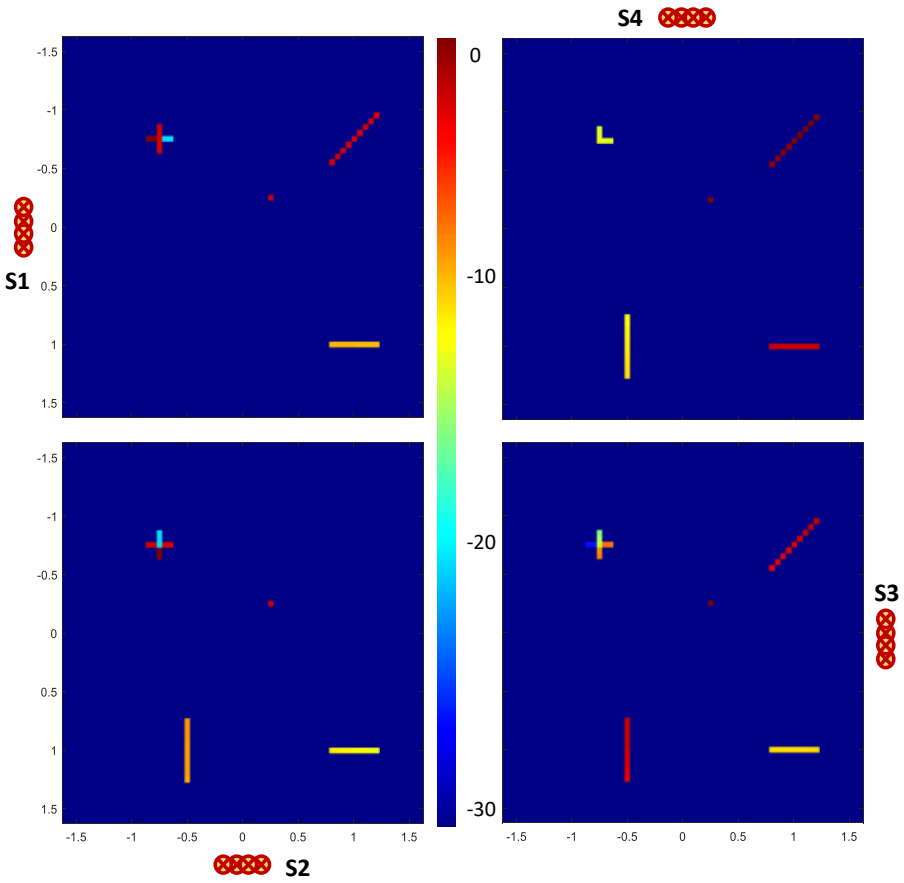

Figure 3.2: Sensors orientation and their ground truth images

3.6 Conclusion

In this chapter, we introduced a modified accelerated version of the ADMM algorithm tailored for radar imaging with widely distributed radar sensors. Our proposed algorithms, namely ACADMM and ASADMM, exhibit similar imaging performance to CADMM and SADMM, respectively. They effectively suppress artifacts and reconstruct high-quality images of the scene. Additionally, they offer significant complexity reduction, resulting in considerably shorter running times compared to the original versions. This reduction in complexity stems from adaptive scene focusing during the iterative reconstruction process. The accelerated algorithms gradually learn the support of the image portion containing the scattering targets and concentrate on that region during subsequent iterations. Simulation results have confirmed the efficacy of the accelerated methods on synthetic simulated scenes.

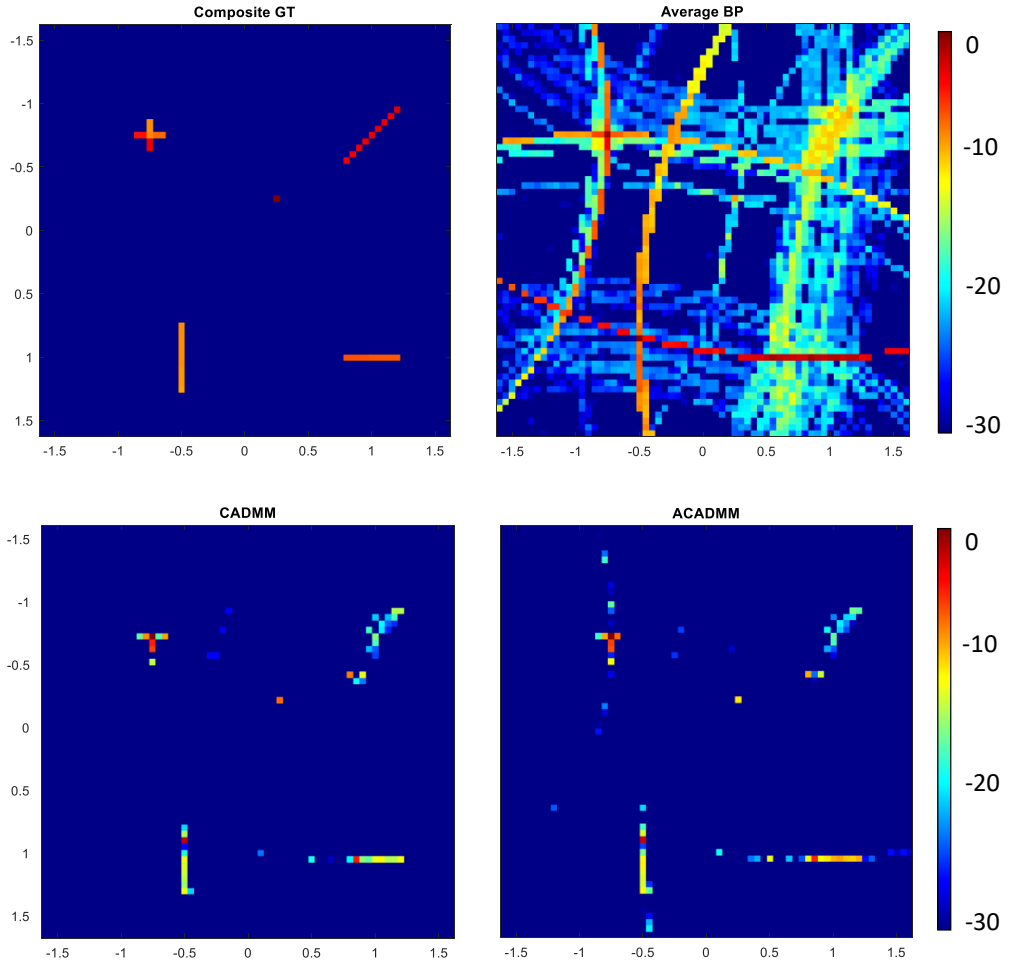

Figure 3.3: Composite ground truth image and reconstructed images with a 30 dB dynamic range using BP, CADMM, and ACADMM

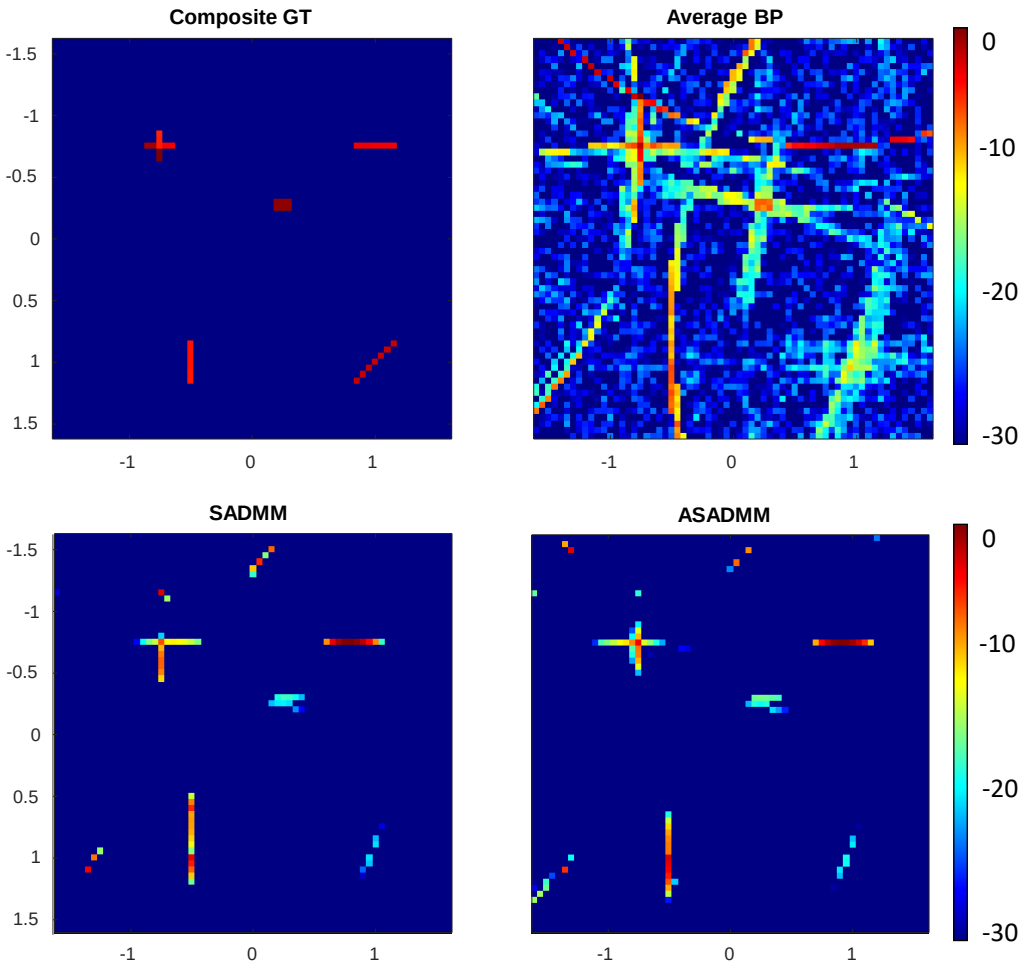

Figure 3.4: Composite ground truth image and reconstructed images with a 30 dB dynamic range using BP, SADMM, and ASADMM

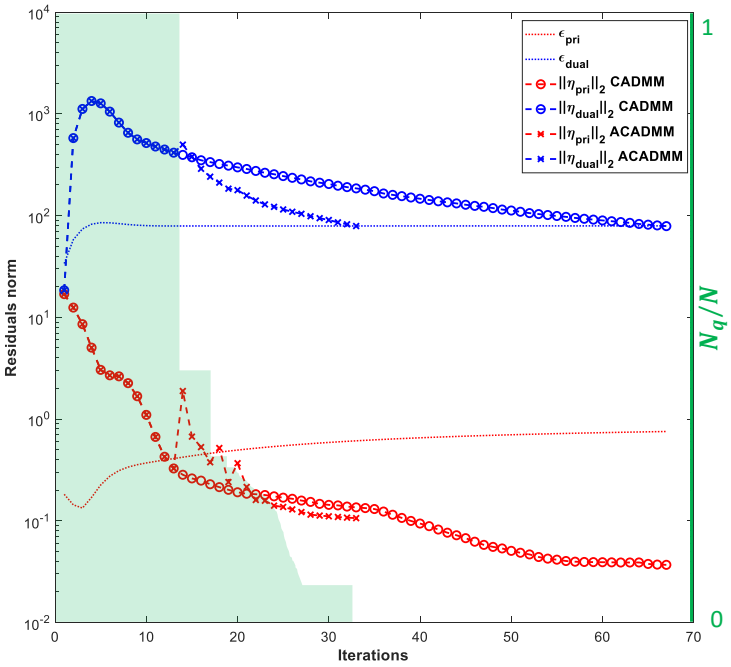

Figure 3.5: CADMM and ACADMM Convergence Rate

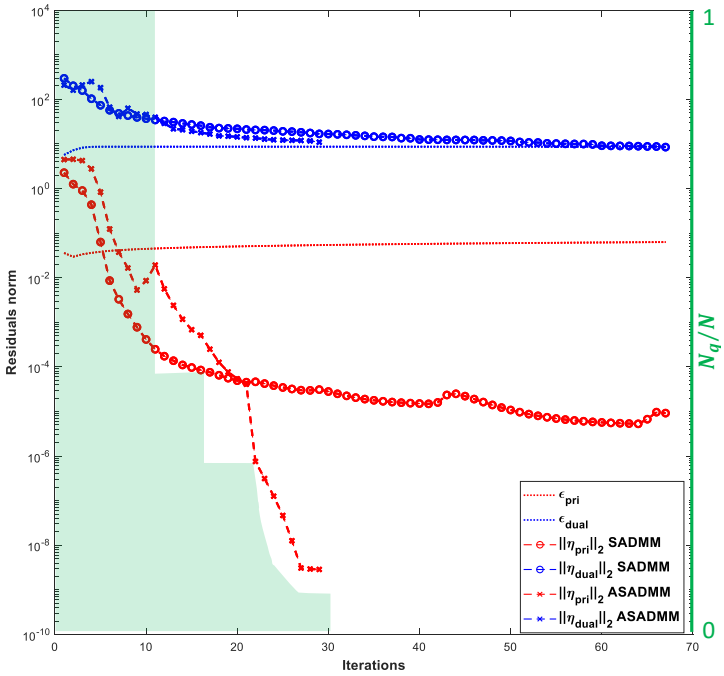

Figure 3.6: SADMM and ASADMM Convergence Rate

Chapter 4

Automatic Hyperparameters Tuning

When employing compressed sensing algorithms for image reconstruction, tuning regularization parameters is crucial to balance data fidelity and prior knowledge. However, as demonstrated in previous chapters, this often involves an empirical grid search over predefined parameter sets. This is a process that hinders the direct implementation of developed methods on a variety of scenes, particularly ones much different from those considered during tuning. To overcome this challenge, this chapter introduces a heuristic method for automatically tuning hyperparameters under scene sparsity priors. The method exploits the soft thresholding applied to back-projection images to set hyperparameter values based on required scene sparsity. Integrated as a sub-routine within a FISTA-inspired algorithm originally proposed for coherently reconstructing scenes observed with partially synchronized distributed sensors, the proposed method efficiently reconstructs the image and corrects clock mismatch errors. Moreover, leveraging the model structure, an FFT-based algorithm implementation is proposed, reducing complexity, running time, and memory requirements compared to direct implementation. Consequently, the modified algorithm provides an effective approach to jointly reconstruct scene images and address clock mismatch errors.

4.1 Introduction

Technology advances in digital signal processing, antenna design, and electronic integration, have attracted considerable attention to the research on Multiple-Input Multiple-Output (MIMO) radars [87]. Real-time imaging applications in surveillance, assisted living, smart buildings, and robotic motion planning offer interesting avenues where

MIMO radars are expected to excel [88, 89] as radar imaging helps to identify and characterize complex objects in the scene [90]. The resolution of radar images in the range and cross-range directions is related to the bandwidth of the transmitted pulse and the size of the radar aperture respectively. Along with the use of wide-band radar waveforms and the transition towards the millimeter-wave frequency spectrum, spatially distributed antenna arrays can be utilized to realize a large physical aperture in order to achieve high image resolution [46]. However, distributed radar sensors feature many challenges that include the establishment of centralized/collaborative coordination of sensor transmissions and precise synchronization among sensors [91].

As far as distributed sensing is concerned, images reconstructed using conventional matched filtering approaches suffer in general from quality degradation due to non-uniform sensor distribution [92]. Alternatively, radar imaging based on the inverse problem and CS methods provide improved performance by incorporating prior information about the scene such as sparsity and smoothness [93]. The advantages of the sparsity-driven regularization methods include increased image quality and robustness to limitations in data quantity [94]. Nevertheless, when considering radar imaging with distributed sensors at high frequencies, the main challenge is the coherence problem due to the ambiguities in antenna positions and difficulties in precisely synchronizing the clocks [95]. While modern positioning systems and time synchronization protocols provide quite accurate location and coarse timing, the remaining errors are still beyond the required high resolution and affect the quality of the reconstructed image resulting in a blurred/unfocused image [96].

The works in [46, 95, 97, 98] have considered these problems within a CS framework. By modeling the position error and the clock synchronization error as shift kernels in the image domain, variations of image blind deconvolution algorithms based on ℓ_1-norm minimization are used to jointly reconstruct the radar image and the shift kernel exploiting the sparsity of both. Such modeling and reconstruction provide very interesting results due to the capability of the model to capture the nature of the error and the powerful algorithms used for image reconstruction such as FISTA [84]. However, when using FISTA and similar regularized optimization algorithms, an empirical search is usually conducted to find a suitable combination of regularization parameters that yield the desired performance. Moreover, when considering clock synchronization mismatch, the models do not account for the reciprocal relation between the distributed sensor pairs leaving the reconstruction algorithm with more parameters than necessary to estimate, thereby increasing the overall complexity and possible reconstruction.

In this chapter, we consider the problem of clock mismatch between the distributed

sensors using the model formulation and FISTA-based reconstruction algorithm introduced in [95]. Building on that work, we propose a modified imaging algorithm that allows for the automatic selection of regularization parameters based on the reconstructed image using the conventional back-projection method, albeit, blurred and influenced by artifacts. Further, we incorporate the system features and introduce an efficient FFT based implementation of the algorithm that exploits the model structure to improve the algorithm running time and reduce its memory requirements compared to its direct implementation.

The chapter is organized as follows. In Section 4.2, we revise the system model and clocks mismatch error formulation. Section 4.3 introduces the subroutine for regularization parameters auto-selection to be used with the FISTA-based algorithm introduced in [95] and provides a reduced complexity implementation for the whole recovery algorithm based on FFT. Subsequently, we examine the performance of our method in Section 4.4 and show an example of image reconstruction. Finally, we conclude the chapter in Section 4.5 and provide some final remarks.

4.2 System Model

We consider using Q distributed radar sensors to observe a two-dimensional scene of size N_c cells containing K static targets. Each radar sensor contains a ULA of N_r receiving antennas and a single transmitting antenna only. We also consider a TDM model in which only one sensor transmits at a time and all the sensors receive the reflections from the scene due to this single transmission. Under this model, we denote with index $m = 1, \ldots, M$ all the transmitter/receiver pairs combinations where $M = Q^2 N_r$. The model presented is based on [95] and is presented here for completeness.

To illuminate the scene, a transmitting antenna emits a pulse $s(t)$ with a bandwidth BW; this pulse propagates through the scene and gets reflected off the targets to the multiple receiving antennas. When considering the transmission related to the m^{th} transmitter/receiver pair, the reflected signal is

$$r_m(t) = \sum_{k}^{K} a_m^k s(t - \tau_m^k) x^k, \tag{4.1}$$

where x_k is the reflectivity of the target k, a_m^k and τ_m^k denote, respectively, the signal attenuation and the delay due to the propagation between the transmitting and receiving antennas of the m^{th} pair reflected by the k^{th} target. Assuming a free space propagation

model, the signal attenuation and delay can be expressed as

$$a_m^k = \frac{1}{{d_{m,Tx}^k}^2 {d_{m,Rx}^k}^2} \quad \text{and} \quad \tau_m^k = \frac{d_{m,Tx}^k + d_{m,Rx}^k}{c},$$

where $d_{m,Tx}^k$ and $d_{m,Rx}^k$ are the distances between the target k and transmitting and receiving antennas pertinent to the m^{th} pair respectively, and c is the speed of light.

When considering a transmitter/receiver antenna pair not belonging to the same sensor, it is extremely difficult to have their clocks perfectly synchronized, especially at higher frequencies. As a result, the received reflected signal in (4.1) will be delayed or advanced according to the relative drift/ mismatch between the clocks of the corresponding sensors In the case of clocks among the sensors of the m^{th} pair with a mismatch error ϵ_m, the received signal is equivalent to a convolution of the signal $r_m(t)$ with a delta function shifted with this error. The received signal in time and frequency domains becomes

$$\begin{aligned} y_m(t) &= r_m(t) * \delta(t - \epsilon_m) \\ &= \left(\sum_k^K a_m^k s(t - \tau_m^k) x^k \right) * \delta(t - \epsilon_m), \\ Y_m(\omega) &= R_m(\omega) e^{-j\omega\epsilon_m} \\ &= \left(\sum_k^K a_m^k S(\omega) e^{-j\omega\tau_m^k} x^k \right) e^{-j\omega\epsilon_m} \end{aligned} \tag{4.2}$$

where ω is the angular frequency, $R(\omega)$ and $S(\omega)$ are the frequency spectrum of $r(t)$ and $s(t)$ respectively.

The observed scene is discretized considering a fine grid of N_c cells such that a single cell can have a single target only and the reflectivity of all scene cells is collected in the vector $\mathbf{x} \in \mathbb{C}^{N_c \times 1}$. If there is no synchronization error between the m^{th} transmitter/receiver pair, the N_s sampled frequency-domain received signal in matrix form is

$$\mathbf{R}_m = \mathbf{A}_m \mathbf{x}, \tag{4.3}$$

where $\mathbf{A}_m \in \mathbb{C}^{N_s \times N_c}$ incorporate the transmitted pulse $S(\omega)$ and the propagation coef-

ficient $a_m^k e^{-j\omega\tau_m^k}$, i.e it can be expressed as

$$\mathbf{A}_m = \begin{bmatrix} a_m^1 e^{-j\omega_1\tau_m^1} S(\omega_1) & \cdots & a_m^{N_c} e^{-j\omega_1\tau_m^{N_c}} S(\omega_1) \\ a_m^1 e^{-j\omega_2\tau_m^1} S(\omega_2) & \cdots & a_m^{N_c} e^{-j\omega_1\tau_m^{N_c}} S(\omega_2) \\ \vdots & \ddots & \vdots \\ a_m^1 e^{-j\omega_{N_s}\tau_m^1} S(\omega_{N_s}) & \cdots & a_m^{N_c} e^{-j\omega_{N_s}\tau_m^{N_c}} S(\omega_{N_s}) \end{bmatrix}.$$

Following the model presented in [95], the frequency domain received signal with synchronization error in equation (4.2) can be rearranged and written as

$$Y_m(\omega) e^{j\omega\epsilon_m} = R_m(\omega). \tag{4.4}$$

Using (4.3) and (4.4), the vector contains the frequency domain received signal with synchronization error $\mathbf{Y}_m$ satisfies

$$\mathbf{D}_{\mathbf{Y}_m} \mathbf{F} \mathbf{z}_m = \mathbf{R}_m = \mathbf{A}_m \mathbf{x}, \tag{4.5}$$

where $\mathbf{D}_{\mathbf{Y}_m}$ is a diagonal matrix with $\mathbf{Y}_m$ on the diagonal, $\mathbf{F}$ is the discrete Fourier transform matrix, and $\mathbf{z}_m$ is the discrete vector of the time domain advance $\delta(t + \epsilon_m)$. With the assumption that $\mathbf{Y}_m$ does not contain any zero frequency components, also assuming noise-free measurements, (4.5) can be written as

$$\begin{bmatrix} \mathbf{D}_{\mathbf{Y}_m}^{-1} \mathbf{A}_m & -\mathbf{F} \end{bmatrix} \begin{bmatrix} \mathbf{x} \\ \mathbf{z}_m \end{bmatrix} = \mathbf{0} \tag{4.6}$$

where $\mathbf{0}$ of dimensions $N_s \times 1$ is a zero vector.

When considering all the measurements from all M transmitter/receiver pairs in the presence of noise, the complete model equation based on (4.6) is

$$\begin{bmatrix} \tilde{\mathbf{A}}_1 & -\mathbf{F} & \emptyset & \emptyset & \cdots & \emptyset \\ \tilde{\mathbf{A}}_2 & \emptyset & -\mathbf{F} & \emptyset & \cdots & \emptyset \\ \vdots & \vdots & \vdots & \vdots & \ddots & \vdots \\ \tilde{\mathbf{A}}_M & \emptyset & \emptyset & \emptyset & \cdots & -\mathbf{F} \end{bmatrix} \begin{bmatrix} \mathbf{x} \\ \mathbf{z}_1 \\ \mathbf{z}_2 \\ \vdots \\ \mathbf{z}_M \end{bmatrix} = \begin{bmatrix} \mathbf{n}_1 \\ \mathbf{n}_2 \\ \vdots \\ \mathbf{n}_M \end{bmatrix} \tag{4.7}$$

where $\tilde{\mathbf{A}}_m = \mathbf{D}_{\mathbf{Y}_m}^{-1} \mathbf{A}_m$, $\emptyset$ is matrix of all zeros of dimension $N_s \times N_s$, and $\mathbf{n}_m$ is the frequency domain additive noise to the measurements related to the m^{th} pair. The model indicates that both the scene reflectivity values $\mathbf{x}$ and the true time shifts $\mathbf{z}_m$,

ideally, lie in the null space of the matrix in the left-hand side of (4.7).

4.3 Image Recovery

4.3.1 Solution Model

Using (4.7), the goal is to recover both the radar scene and the true time shifts jointly. The problem is ill-posed when $MN_s < N_c + MN_s$ and a unique solution does not exist. Since $\mathbf{z}_m$ is 1-sparse signal (shift kernel) and $\mathbf{x}$ is sparse by assumption, as formulated in [95], both the parameters can be recovered by finding the solution of the following optimization problem

$$\begin{aligned} \min_{\mathbf{x},\mathbf{z}_1,\mathbf{z}_2,\cdots,\mathbf{z}_M} \lambda_x \left\|\mathbf{x}\right\|_1 + \lambda_z \sum_{m=1}^{M} \left\|\mathbf{z}_m\right\|_1 + \left\|\mathbf{B}\ \mathbf{w} - \mathbf{b}\right\|_2^2, \\ \text{subject to:} \quad \mathbf{x} > \mathbf{0}_{N_c},\ \mathbf{z}_m > \mathbf{0}_{N_s},\ \mathbf{1}^T\mathbf{z}_m = 1,\ \forall m, \end{aligned} \tag{4.8}$$

where λ_x and λ_z are the regularization parameters on the ℓ_1 norm of the scene reflectivity and time shifts respectively,

$$\mathbf{B} = \begin{bmatrix} \tilde{\mathbf{A}}_1 & -\mathbf{F} & \emptyset & \emptyset & \cdots & \emptyset \\ \tilde{\mathbf{A}}_2 & \emptyset & -\mathbf{F} & \emptyset & \cdots & \emptyset \\ \vdots & \vdots & \vdots & \vdots & \ddots & \vdots \\ \tilde{\mathbf{A}}_M & \emptyset & \emptyset & \emptyset & \cdots & -\mathbf{F} \\ \mathbf{1}_{N_C}^T & \mathbf{0}_{N_s}^T & \mathbf{0}_{N_s}^T & \mathbf{0}_{N_s}^T & \cdots & \mathbf{0}_{N_s}^T \end{bmatrix}, \mathbf{b} = \begin{bmatrix} \mathbf{0} \\ \mathbf{0} \\ \vdots \\ \mathbf{0} \\ C \end{bmatrix}, \tag{4.9}$$

and $\mathbf{w} = \begin{bmatrix} \mathbf{x}^T & \mathbf{z}_1^T & \mathbf{z}_2^T & \cdots & \mathbf{z}_M^T \end{bmatrix}^T$. The last row of the matrix $\mathbf{B}$ is to apply a soft constraint on the sum of the reflectivity image to equal a pre-determined constant C to avoid the trivial solution of all zeros. Here, $\mathbf{1}$ and $\mathbf{0}$ are vectors of all ones and zeros. The hard constraints in (4.8) are to ensure that both $\mathbf{x}$ and $\mathbf{z}_m$ are non-negative in addition to a scaling constraint to ensure that $\mathbf{z}_m$ is 1-sparse for each m.

4.3.2 FISTA Parameters Auto-selection

The problem in (4.8) is a convex sparse recovery problem for which a FISTA-inspired algorithm has been proposed in [95]. The algorithm requires the regularization parameters λ_x and λ_z as inputs; however, these quantities vary from one scenario to another, motivating an auto-selection procedure valid for a plethora of scenarios. In this context, we consider a subroutine PAS which returns the vector λ containing the regularization

Algorithm 4 FISTA for distributed unsynchronized radar imaging with parameters auto-selection

Input: $\{\mathbf{A}_m\}_{m=1}^{M}$ and $\{\mathbf{Y}_m\}_{m=1}^{M}$

Initialize:

$\mathbf{w}^0 = \mathbf{u}^0 = \begin{bmatrix}\mathbf{0}_{N_c}^T & \mathbf{z}_0^T\end{bmatrix}^T$, $t^0 = 1$

$\hat{\lambda}, C \leftarrow PAS(\{\mathbf{A}_m\}_{m=1}^{M}, \{\mathbf{Y}_m\}_{m=1}^{M})$

set $\mathbf{B}$ and $\mathbf{b}$ as in (4.9)

while stopping criteria **do**

1. $\mathbf{v}^j \leftarrow \mathbf{w}^{j-1} + \alpha\mathbf{B}^H(\mathbf{b} - \mathbf{B}\mathbf{w}^{j-1})$
2. $\tilde{\mathbf{v}}^j \leftarrow \mathcal{T}(\mathbf{v}^j, \alpha\lambda)$
3. $\tilde{\mathbf{u}}^j \leftarrow \mathbf{P}_{\mathbb{R}_+}(\tilde{\tilde{\mathbf{v}}}^j)$
4. $\mathbf{u}^j \leftarrow \mathbf{E}_{rp}(\tilde{\mathbf{u}}^j)$
5. $t^j \leftarrow \frac{1+\sqrt{1+4(t^{j-1})^2}}{2}$
6. $\mathbf{w}^{j-1} \leftarrow \frac{t^{j-1}-1}{t^j}(\mathbf{u}^j - \mathbf{u}^{j-1})$

end while

parameters

$$\hat{\lambda} = \begin{bmatrix} \hat{\lambda}_x \mathbf{1}_{N_C} \\ \hat{\lambda}_z \mathbf{1}_{N_s} \\ \hat{\lambda}_z \mathbf{1}_{N_s} \\ \vdots \\ \\ \hat{\lambda}_z \mathbf{1}_{N_s} \end{bmatrix}. \tag{4.10}$$

Algorithm 4 summarizes the steps to recover the radar image solving (4.8). The algorithm is initialized with a zero vector for the image part of $\mathbf{w}$, while $\mathbf{z}_0$ is a vector of dimensions $MN_s \times 1$ comprising the shift kernels. $\mathbf{z}_0$ contains M time-domain Dirac deltas (at zero lag) realizing a shift kernel equivalent to no mismatch error for all the M transmitter/receiver pairs. The function $\mathcal{T}(.)$ at step 2 is the element-wise soft-thresholding operator while $\mathbf{P}_{\mathbb{R}_+}(.)$ at step 3 represents the projection onto the non-negative real orthant followed by a normalization. Finally, $\mathbf{E}_{rp}$ ensures that the $\mathbf{z}$ components belonging to a reciprocal transmitter/receiver pair are a flipped version of each other. The parameters auto selection subroutine PAS relies on the blurred image reconstructed from back-projection, i.e. multiplication with the adjoint matrix. Considering step (1)

of Algorithm 4, we can write this step as $\mathbf{v}^j \leftarrow D_\alpha(\mathbf{w}^{j-1})$ where

$$D_\alpha(x) = (\mathbf{I} - \alpha \mathbf{B}^H \mathbf{B})x + \alpha \mathbf{B}^H \mathbf{b}. \tag{4.11}$$

Accordingly, the soft thresholding operator step is $\tilde{\mathbf{v}}^j \leftarrow \mathcal{T}(D_\alpha(\mathbf{w}^{j-1}), \alpha\lambda)$. Now, let $\mathbf{x}^*$ be the optimum solution of the imaging problem with K-sparsity, $D_\alpha(\mathbf{x}^*)$ can be sorted as

$$[D_\alpha(\mathbf{x}^*)]_1 \geq [D_\alpha(\mathbf{x}^*)]_2 \geq \cdots \geq [D_\alpha(\mathbf{x}^*)]_{N_c}.$$

Then, due to the thresholding operator $\mathcal{T}(.)$, the following holds

$$\begin{aligned} \left|\left[D_\alpha(\mathrm{x}^*)\right]_i\right| &\geq \alpha\lambda \Rightarrow i \in \{1, 2, \cdots, K\} \\ \left|\left[D_\alpha(\mathrm{x}^*)\right]_i\right| &< \alpha\lambda \Rightarrow i \in \{K+1, K+2, \cdots, N_c\}, \end{aligned} \tag{4.12}$$

which implies that

$$\lambda_{\text{opt}} \in \left[\left|\left[D_\alpha(\mathbf{x}^*)\right]_K\right|/\alpha, \left|\left[D_\alpha(\mathbf{x}^*)\right]_{K+1}\right|/\alpha\right]. \tag{4.13}$$

From (4.12) and (4.13), we notice that if we have an approximation of $\mathbf{x}^*$ in terms of sparsity and global magnitude order only (corresponding entries do not matter since we can sort them), say $\hat{\mathbf{x}}$ with L-sparsity $\geq K$, we can set $\hat{\lambda}$ to $\left|\left[D_\alpha(\hat{\mathbf{x}})\right]_L\right|/\alpha$ and obtain a good image reconstruction.

We claim that in our scenario such approximation is possible from the image reconstructed through the adjoint matrix. Since we consider a single transmitter antenna at each sensor, the monostatic contributions of transmitter/receiver pairs of which both antennas belong to the same sensor will provide a certain relative energy level of all targets that is proportionally related to the true relative targets' reflectivity levels. Additionally, even in the presence of ghost targets and blurring effects, the back-projection image still has a high-energy focus in a few locations due to the sparse nature of the scene itself. As a result, it can be made more sparse by applying a threshold β under which the back-projection entries are set to zero. One way to specify β is to set it so it nullifies the entries lower than a threshold.

In a few words, by appropriate scaling and thresholding of the back-projection image, we can obtain an approximate $\hat{\mathbf{x}}$ sufficient to set the regularization parameters for FISTA reconstruction. Algorithm 5 summarizes the steps of PAS subroutine. It is worth noting that P is the power of the transmitted pulse.

Algorithm 5 PAS subroutine for FISTA parameters auto-selection

Input: $\{\mathbf{A}_m\}_{m=1}^{M}$ and $\{\mathbf{Y}_m\}_{m=1}^{M}$
Set:

$$\mathbf{A} \leftarrow \begin{bmatrix}\mathbf{A}_1^T & \mathbf{A}_2^T & \cdots & \mathbf{A}_M^T\end{bmatrix}^T$$
$$\mathbf{Y} \leftarrow \begin{bmatrix}\mathbf{Y}_1^T & \mathbf{Y}_2^T & \cdots & \mathbf{Y}_M^T\end{bmatrix}^T$$

1. $\hat{\mathbf{x}} \leftarrow \frac{1}{MP}\mathbf{A}^H\mathbf{Y}$
2. $C \leftarrow \|\hat{\mathbf{x}}\|_1$
3. $[\hat{\mathbf{x}}]_i \leftarrow 0$ (if $[\hat{\mathbf{x}}]_i < \max(\hat{\mathbf{x}})/\beta$)
4. $\hat{\mathbf{x}}_s \leftarrow \text{sort}(\hat{\mathbf{x}}, \text{descend})$
5. $l_s \leftarrow \{\max(i) : [\hat{\mathbf{x}}_s]_i \neq 0\}$
6. $\hat{\mathbf{w}} \leftarrow \begin{bmatrix}\hat{\mathbf{x}}^T & \mathbf{z}_0^T\end{bmatrix}^T$
7. $\hat{\lambda}_x \leftarrow \left|\left[D_\alpha(\hat{\mathbf{w}})\right]_{l_s}\right|/\alpha$
8. $\hat{\lambda}_z \leftarrow \left|\left[D_\alpha(\hat{\mathbf{w}})\right]_{N_c+M}\right|/\alpha$

Output: C, $\hat{\lambda}_x$, $\hat{\lambda}_z$

4.3.3 Reduced Complexity Implementation

The matrix $\mathbf{B}$ in (4.9) has the dimension $MN_s \times (N_c + MN_s)$ which is already a large matrix and grows even larger when increasing the number of transmitter/receiver pairs M, number of samples N_s (e.g. when using a pulse with a larger bandwidth), or the size of the scene N_c. This affects the performance of the algorithm wherein each iteration includes a multiplication with the matrix $\mathbf{B}^H\mathbf{B}$ in step 1 causing a significant increase in execution time. More importantly, it requires a noticeably large memory size to store the matrix $\mathbf{B}$ and other variables which is critical when dealing with radar sensors offering limited resources. To this end, noticing that the big portion of the matrix $\mathbf{B}$ is nothing but the Discrete Fourier Transform (DFT) matrix, also that the matrix $\mathbf{B}^H\mathbf{B}$ needed for step 1 is symmetric, in this section we provide an implementation of the algorithm using FFT which significantly reduces the memory requirements and enhance the algorithm running time.

Let us consider the block partitioned matrix $\mathbf{B}$

$$\mathbf{B} = \begin{bmatrix} \tilde{\mathbf{A}} & \mathcal{F} \\ \mathbf{1}_{N_c}^T & \emptyset \end{bmatrix} \tag{4.14}$$

where

$$\mathcal{F} = \begin{bmatrix} -\mathbf{F} & \emptyset & \cdots & \emptyset \\ \emptyset & -\mathbf{F} & \cdots & \emptyset \\ \vdots & \vdots & \ddots & \vdots \\ \emptyset & \emptyset & \cdots & -\mathbf{F} \end{bmatrix} \text{ and } \tilde{\mathbf{A}} = \begin{bmatrix} \tilde{\mathbf{A}}_1 \\ \tilde{\mathbf{A}}_2 \\ \vdots \\ \tilde{\mathbf{A}}_M \end{bmatrix}$$

When considering step 1 of Algorithm (4), it can be rewritten as

$$\mathbf{v}^j \leftarrow \mathbf{w}^{j-1} - \alpha \mathbf{B}^H \mathbf{B} \mathbf{w}^{j-1} + \alpha \mathbf{B}^H \mathbf{b} \tag{4.15}$$

Using (4.14) and (4.15), we can write

$$\begin{aligned} \mathbf{B}\mathbf{w}^{j-1} &= \begin{bmatrix} \tilde{\mathbf{A}}\mathbf{x}^{j-1} \\ \sum \mathbf{x}^{j-1} \end{bmatrix} + \begin{bmatrix} \mathcal{F}\mathbf{z}^{j-1} \\ 0 \end{bmatrix} \\ \mathbf{B}^H \mathbf{b} &= \begin{bmatrix} \mathrm{C}\mathbf{1}_{N_c} \\ \mathbf{0} \end{bmatrix} \end{aligned} \tag{4.16}$$

where

$$\mathbf{w}^{j-1} = \begin{bmatrix} \mathbf{x}^{j-1} \\ \mathbf{z}^{j-1} \end{bmatrix}, \quad \text{and } \mathcal{F}\mathbf{z}^{j-1} = \begin{bmatrix} -\mathrm{fft}(\mathbf{z_1}^{j-1}) \\ -\mathrm{fft}(\mathbf{z_2}^{j-1}) \\ \vdots \\ -\mathrm{fft}(\mathbf{z_M}^{j-1}) \end{bmatrix}.$$

Similarly, from (4.15) and (4.16) we can write

$$\begin{aligned} \mathbf{B}^H \mathbf{B} \mathbf{w}^{j-1} &= \begin{bmatrix} \tilde{\mathbf{A}}^H & \mathbf{1}_{N_c} \\ \mathcal{F}^H & \mathbf{0} \end{bmatrix} \left(\begin{bmatrix} \tilde{A}\mathbf{x}^{j-1} \\ \sum \mathbf{x}^{j-1} \end{bmatrix} + \begin{bmatrix} \mathcal{F}\mathbf{z}^{j-1} \\ 0 \end{bmatrix} \right) \\ &= \begin{bmatrix} \tilde{\mathbf{A}}^H \tilde{\mathbf{A}} \mathbf{x}^{j-1} + \sum \mathbf{x}^{j-1} \\ \mathcal{F}^H \tilde{\mathbf{A}} \mathbf{x}^{j-1} \end{bmatrix} + \begin{bmatrix} \tilde{\mathbf{A}}^H \mathcal{F}\mathbf{z}^{j-1} \\ \mathcal{F}^H \mathcal{F}\mathbf{z}^{j-1} \end{bmatrix} \end{aligned} \tag{4.17}$$

where

$$\mathcal{F}^H \tilde{\mathbf{A}} \mathbf{x}^{j-1} = \begin{bmatrix} \text{ifft}(\tilde{\mathbf{A}}_1 \mathbf{x}^{j-1}) \\ \text{ifft}(\tilde{\mathbf{A}}_2 \mathbf{x}^{j-1}) \\ \vdots \\ \text{ifft}(\tilde{\mathbf{A}}_M \mathbf{x}^{j-1}) \end{bmatrix}$$

which finally reduces step 1 of Algorithm 4 to

$$\mathbf{v}^j \leftarrow \mathbf{w}^{j-1} - \alpha \begin{bmatrix} \tilde{\mathbf{A}}^H \tilde{\mathbf{A}} \mathbf{x}^{j-1} + \sum \mathbf{x}^{j-1} + \tilde{A}^H \mathcal{F} \mathbf{z}^{j-1} - C\mathbf{1}_{N_c} \\ \mathcal{F}^H \tilde{\mathbf{A}} \mathbf{x}^{j-1} + N_s \mathbf{z}^{j-1} \end{bmatrix} \tag{4.18}$$

Thus the computation is significantly reduced by the use of FFT, while only the matrices $\tilde{\mathbf{A}}^H \tilde{\mathbf{A}}$, and $\tilde{\mathbf{A}}$ need to be stored.

4.4 Numerical Analysis

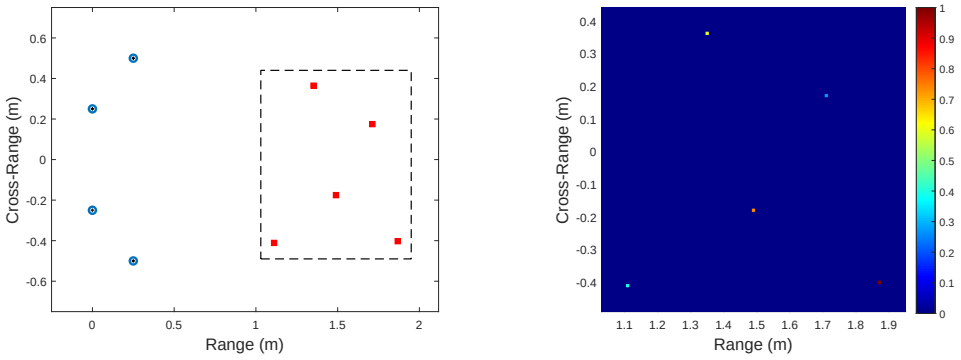

(a) (b)

Figure 4.1: (a) Scenario layout; (b) Reflectivity ground-truth

In this section, the performance of our proposed method for automatic parameter selection is evaluated and FISTA is implemented using our compact formula (4.18) of the update step. We run our simulations considering a synthetic radar scene in which a small Region of Interest (ROI) containing $K = 5$ static targets is examined. Using a fine grid with cells of size 0.01 m $\times$ 0.01 m, our ROI consists of $Nc = 94 \times 93 = 8742$ cells. To observe the scene, 4 radar sensors with 2 antennas each (1 transmitting and 1 receiving) are used. Figure 4.1 shows the layout of the distributed sensors and the true reflectivity image of the ROI. Considering a single sensor transmission at a time, our scenario has $M = 16$ transmitter/receiver pairs. A LFM with a sweeping bandwidth BW = 3 GHz is used for transmission at all sensors and the received signal is sampled

at the Nyquist frequency. The received signal is corrupted with white Gaussian noise and has a Peak Signal-to-Noise Ratio (PSNR) of 20 dB.

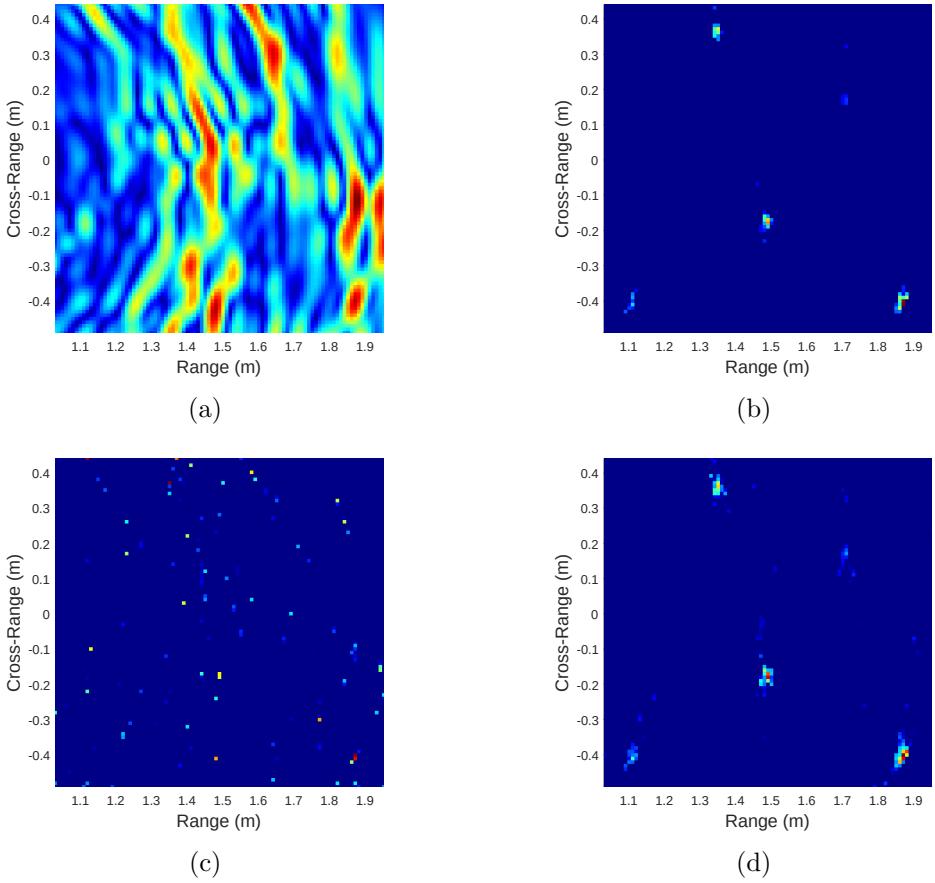

Figure 4.2: Image reconstruction by (a) Adjoint matrix, (b) FISTA with auto-selected parameters $\hat{\lambda}$, (c) and (d) FISTA with mismatched parameters $2\hat{\lambda}$ and $\hat{\lambda}/2$, respctively.

We considered a maximum mismatch error between the clocks of the sensor $T_{\max} = 1.33$ ns which is equivalent to the time of 20 samples. As mentioned in section 4.3.2, a couple of reciprocal transmitter/receiver pairs will have the reverse time error with respect to each other (delay/advance), while a transmitter/receiver pair of antennas belonging to the same sensor does not experience any mismatch error.

Along with the image reconstructed by the adjoint matrix Figure 4.2(a), we show the reconstructed image of the scene using the FISTA algorithm with the regularization parameters calculated through our method in Figure 4.2(b). Additionally, we show the reconstruction using a slightly scaled version of the parameters, namely $0.5\hat{\lambda}$ and $2\hat{\lambda}$ Figure 4.2(c) and Figure 4.2(d) respectively. It can be seen that running FISTA with auto-selected parameters $\hat{\lambda}$ gives better image reconstruction in comparison with using other slightly higher/lower parameters. When using a higher regularization parameter,

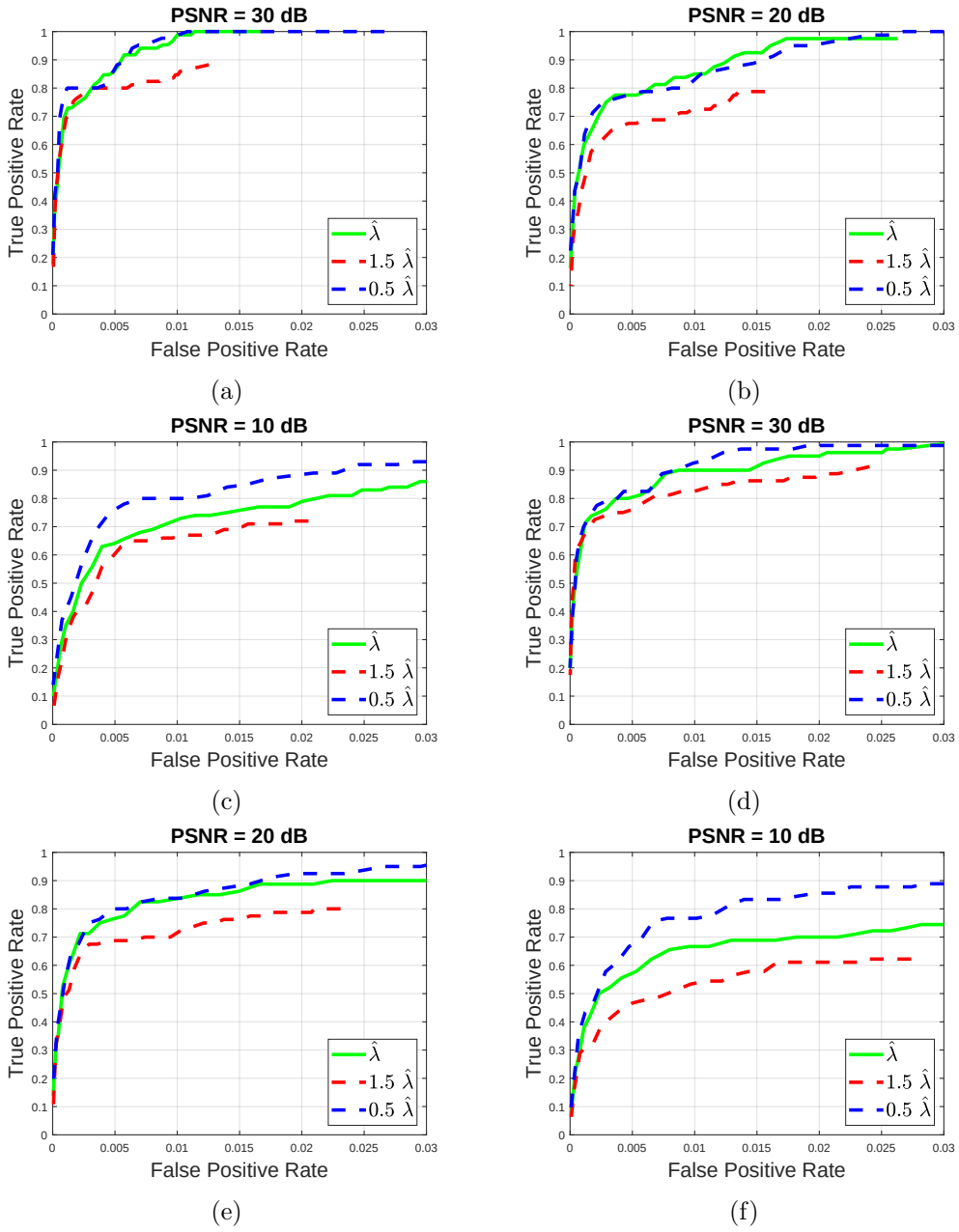

Figure 4.3: ROC curves for image reconstruction using our calculated $\hat{\lambda}$ versus $1.5\hat{\lambda}$ and $\hat{\lambda}/2$ at different PSNR levels. The maximum mismatch error T_{max} is equivalent to 5 samples (Top row) and 25 samples (Bottom row).

the reconstructed image becomes sparser and more ghost targets are introduced as in Figure 4.2(c). On the other hand, using a lower parameter, results in an unfocused image along with a concentrated region of ghost targets too as in Figure 4.2(d).

In order to assess the performance of our method at different PSNR levels and different mismatch errors, in Figure 4.3 we calculate the Receiver Operating Characteristic (ROC) curves for image reconstruction using $\hat{\lambda}$, $1.5\hat{\lambda}$ and $\hat{\lambda}/2$ at PSNR level of 10, 20, and 30 dB for maximum mismatch errors $T_{\max}$ equivalent to 5 and 25 samples. Each curve is the average performance over 30 realizations of noise and mismatch error.

From the curves, we note that while using $1.5\hat{\lambda}$ instead of $\hat{\lambda}$ lowers the detection performance at all PSNR levels, using $\hat{\lambda}/2$ provides a comparable detection performance to using $\hat{\lambda}$ at high PSNR and even better performance at low PSNR levels. This can be justified by looking to the reconstructed images in Figure 4.2(b) and Figure 4.2(d) and recalling the nature of ROC curves being a measure of true target detection versus false alarms after a thresholding step. Accordingly, since a lower regularization parameter allows for a higher magnitude and blurred reconstructed image, targets will remain detectable after thresholding unlike the focused image reconstructed using higher parameters.

4.5 Conclusion

In this chapter, we introduced a method for efficiently implementing a FISTA-based algorithm for radar imaging with distributed unsynchronized sensors. This efficiency enhancement is achieved through two aspects: 1) automatic hyperparameter tuning, and 2) reduced complexity implementation based on FFT. The automatic parameter tuning relies on exploiting the structure of the blurred image of the scene reconstructed by the adjoint matrix (BP image) during the soft thresholding step. The BP image provides an upper bound for the scene sparsity degree, allowing for setting the regularization parameters accordingly. The FFT-based implementation offers a compact and storage-efficient implementation of the algorithm, reducing computation overhead. Both parameter auto-selection and reduced complexity implementation pave the way for applying such algorithms in real-time scenarios rather than relying on post-processing after collecting measurements.

Part II

Point Clouds Detection

Chapter 5

Distributed Detection of Aspect-Dependent Targets

In this chapter, we tackle the challenge of detecting aspect-dependent fluctuating targets observed with distributed mmWave radar sensors. Our objective is to enhance the quality of point cloud detections by devising a detector that jointly considers the processed signals from all sensors and accounts for variations in RCS due to aspect-dependent fluctuations of the targets. To achieve this, we derive a detector based on the Generalized Likelihood Ratio Test (GLRT), aiming to estimate the fluctuation parameters of the targets at each sensor using multiple chirps. The resulting joint test is a weighted sum of individual tests applied to the square law detector output of each sensor, with weights proportional to the local SNR at each sensor. These weights contrast significantly due to variations in aspect angles and path losses for a single Cell Under Test (CUT). Through Monte-Carlo simulations, we validate the performance of the proposed detector, demonstrating its superiority over conventional detection methods that employ non-coherent integration of chirps and aggregation of tests from all sensors.

5.1 Introduction

The emergence of MIMO mmWave radar sensors has received tremendous interest in recent years, especially for indoor sensing applications [55]. Such applications include human detection and activity recognition [99], vital signs monitoring [14], and real-time tracking of multiple individuals [100], to name a few. Additionally, driven by the availability and affordability of such sensors, employing widely distributed sensing systems has drawn attention in the majority of applications due to the advantages that are allowed by such architectures [38]. In particular, the use of distributed sensors

enables the capture of highly fluctuating and aspect angle-dependent targets. This results in a higher detection of such targets in addition to improving system robustness by providing redundancy in the events of occlusion or sensor failures [39, 41, 42].

Typically, detections by multiple widely distributed sensors are fused in the data domain after processing, rather than implementing a joint detection scheme. While data domain fusion allows for the use of simpler detection algorithms at each sensor, joint detection can potentially offer improved detection performance by appropriately weighting the data received from the different sensors and leveraging more the ones with a higher available SNR [44, 101]. Even though the optimum detector in the Neyman-Pearson sense for fluctuating targets observed with multistatic radars has long existed in the literature [102–104], to the best of our knowledge, the corresponding sub-optimal GLRT detector and the analysis of its performance versus the aspect angle dependence of the RCS have not been explicitly introduced, especially for indoor sensing environments. The optimum detector performs the Likelihood Ratio Test (LRT) assuming perfect knowledge of the expected average local SNR available to each sensor which is impractical. Thus, an estimation of the average received power at each sensor is required for the implementation of the detector.

Accordingly, in this chapter, we analytically devise the GLRT detector for fluctuating targets observed by widely distributed mmWave sensors each transmits multiple chips (pulses). Due to the angular diversity, the targets feature an aspect-dependent RCS that can vary significantly with respect to different sensors. We formulate the detection problem taking this into account and utilize Maximum Likelihood Estimation (MLE) in the derivation of the detector to achieve the optimum weighting in the GLRT sense. We evaluate the performance of the proposed detector using Monte-Carlo simulations and show that it outperforms the conventional detectors which employ non-coherent integration of multiple chirps and integrate the data from multiple sensors equally [105]. The proposed detector realizes higher gain in detection performance in the cases of higher variance of the RCS with respect to different sensors and achieves asymptotically the performance of the optimum LRT detector in extreme scenarios of RCS variation.

Throughout this chapter, vectors are denoted in lowercase bold font, while matrices are in uppercase bold. $\mathbf{I}_L$ is the identity matrix of size $L \times L$ and $\mathbf{0}_N$ is a vector of all zeros of size $N \times 1$. The superscripts $.^T$ and $.^H$ denote, respectively, the transpose and the complex conjugate transpose of a vector or a matrix. The operators $|.|$ and $\|.\|_2$ are used for the matrix determinant and the Frobenius norm, respectively. The symbol $\otimes$ is used for the Kronecker product.

5.2 System and Signal Model

We consider a widely distributed radar system with Q mmWave MIMO radar sensors, each having N_{tx} and N_{rx} transmitting and receiving antenna elements, respectively. Assume that $\mathbf{p}_q = [x_q, y_q, z_q]^T$ denotes the absolute position of the q^{th} radar sensor, where x_q, y_q, and z_q represents the absolute Cartesian coordinates, with $q = 1, 2, \ldots, Q$. In this case, a target with absolute position $\mathbf{p}_s = [x_s, y_s, z_s]^T$ and absolute velocity $\mathbf{v}_s = [v_{xs}, v_{ys}, v_{zs}]^T$, will have a relative distance R_q, azimuth θ_q, and elevation ϕ_q with the q^{th} radar sensor. The target received signal can be expressed as

$$\mathbf{x}_q = \alpha_q \mathbf{s}_q(\theta_q, \phi_q) + \mathbf{w}_q \in \mathbb{C}^{N_{tx}N_{rx}\times 1} \tag{5.1}$$

where α_q indicates the complex value of the reflected signal at the q^{th} radar sensor which comprises path losses and target RCS, and fluctuates from pulse to pulse, $\mathbf{w}_q$ denotes the interference signal that can include both clutter and thermal noise. In this chapter, we assume $\mathbf{w}_q \sim \mathcal{CN}(\mathbf{0}, \sigma_{\mathbf{w}}^2 \mathbf{I})$ contains only receiver thermal noise which has a flat Power Spectral Density (PSD) with $P(f) = k_B T_0$, where k_B is the Boltzmann constant and T_0 is the effective noise temperature. Moreover, the signal steering vector is,

$$\mathbf{s}_q(\theta_q, \phi_q) = \mathbf{a}_q(\theta_q, \phi_q) \otimes \mathbf{b}_q(\theta_q, \phi_q),$$

where the spatial transmit and receive steering vectors are defined respectively as

$$\mathbf{a}_q(\theta, \phi) = \begin{bmatrix} e^{-j\mathbf{k}^T(\theta,\phi)\mathbf{p}_{q,1}} \\ e^{-j\mathbf{k}^T(\theta,\phi)\mathbf{p}_{q,2}} \\ \vdots \\ e^{-j\mathbf{k}^T(\theta,\phi)\mathbf{p}_{q,N_{tx}}} \end{bmatrix}, \quad \mathbf{b}_q(\theta, \phi) = \begin{bmatrix} e^{-j\mathbf{k}^T(\theta,\phi)\mathbf{p}_{q,1}} \\ e^{-j\mathbf{k}^T(\theta,\phi)\mathbf{p}_{q,2}} \\ \vdots \\ e^{-j\mathbf{k}^T(\theta,\phi)\mathbf{p}_{q,N_{rx}}} \end{bmatrix},$$

and $\mathbf{k}(\theta, \phi) = \frac{2\pi}{\lambda}[\cos\theta\cos\phi, \sin\theta\cos\phi, \sin\phi]^T$ is the wave-number vector with θ and ϕ are azimuth and elevation angles, respectively. $\mathbf{p}_{q,nt}$ and $\mathbf{p}_{q,nr}$ are the locations of the q^{th} radar transmit and receive array elements, respectively. At the fusion center, the received signals can be stacked by $\mathbf{x} = [\mathbf{x}_1^T, \mathbf{x}_2^T, ..., \mathbf{x}_Q^T]^T$ and $\mathbf{w} = [\mathbf{w}_1^T, \mathbf{w}_2^T, ..., \mathbf{w}_Q^T]^T$, and $\boldsymbol{\alpha} = [\alpha_1, \alpha_2, ..., \alpha_Q]^T$. By defining the steering matrix $\mathbf{S} \in \mathbb{C}^{QN_{tx}N_{rx}\times Q}$ as,

$$\mathbf{S} = \begin{bmatrix} \mathbf{s}_1(\theta_1, \phi_1) & \mathbf{0}_{N_{tx}N_{rx}} & \cdots & \mathbf{0}_{N_{tx}N_{rx}} \\ \mathbf{0}_{N_{tx}N_{rx}} & \mathbf{s}_2(\theta_2, \phi_2) & \cdots & \mathbf{0}_{N_{tx}N_{rx}} \\ \vdots & \vdots & \ddots & \vdots \\ \mathbf{0}_{N_{tx}N_{rx}} & \mathbf{0}_{N_{tx}N_{rx}} & \cdots & \mathbf{s}_Q(\theta_Q, \phi_Q) \end{bmatrix}.$$

The stacked received signal of M chirps (pulses) in one Coherent Processing Interval (CPI) reflected from a certain range CUT can be obtained by

$$\mathbf{X} = \mathbf{S}\boldsymbol{A} + \mathbf{W} \in \mathbb{C}^{\Omega \times M} \tag{5.2}$$

where the matrix $\mathbf{X} = [\mathbf{x}^{(1)}\mathbf{x}^{(2)} \cdots \mathbf{x}^{(M)}]$ collects the received signal of M chirps having the received signal at the m^{th} chirp obtained by

$$\mathbf{x}^{(m)} = \mathbf{S}\boldsymbol{\alpha}^{(m)} + \mathbf{w}^{(m)}, \tag{5.3}$$

$\boldsymbol{A} = [\boldsymbol{\alpha}^{(1)}, \boldsymbol{\alpha}^{(2)}, \cdots, \boldsymbol{\alpha}^{(M)}]$ represents the fluctuation of the amplitude of the signal from pulse to pulse, $\mathbf{W} = [\mathbf{w}^{(1)}, \mathbf{w}^{(2)}, \cdots, \mathbf{w}^{(M)}]$ is the aggregate matrix of thermal noise for all pulses, $\Omega = QN_{tx}N_{rx}$, and $m = 1, \cdots, M$.

The reflected signal amplitudes are assumed to fluctuate from pulse to pulse at each sensor. We consider a Rayleigh fluctuation model (Swerling II) of the amplitudes of the reflected signals at the q^{th} sensor which is equivalent to its complex value being distributed as $\alpha_q \sim \mathcal{CN}(0, \sigma^2_{\alpha_q})$.

Let $\mathcal{H}_0$ represent the null hypothesis that a target is absent, and $\mathcal{H}_1$ represent the alternative hypothesis that a target is present in the CUT. The detection problem can be cast as the following binary hypothesis test

$$\begin{cases} \mathcal{H}_0 : & \mathbf{X} = \mathbf{W} \\ \mathcal{H}_1 : & \mathbf{X} = \mathbf{S}\boldsymbol{A} + \mathbf{W} \end{cases} \tag{5.4}$$

In the next section, we provide the corresponding detector based on GLRT.

5.3 GLRT Detector Derivation

In order to derive the GLRT test, the Probability Density Function (PDF) of the collection of the received signals from multiple chirps $\mathbf{X}$ under the null and the alternative hypotheses are to be evaluated. We first simplify the PDFs for a single chirp, then since the received signals from consecutive chirps are independent, the PDF of $\mathbf{X}$ is the

multiplication of the PDFs of the single chirps. Under the null hypothesis, the received signal contains only the noise that is modeled as a central complex white Gaussian noise and has the PDF

$$p(\mathbf{x} \mid \mathcal{H}_0) = \frac{1}{\sqrt{\pi^{2\Omega}\,|\mathbf{C_{ww}}|}} \exp\left(-\frac{1}{2}\mathbf{x}^H \mathbf{C}_{\mathbf{ww}}^{-1}\mathbf{x}\right) \tag{5.5}$$

where $\mathbf{C_{ww}} = \sigma_{\mathbf{w}}^2 \mathbf{I}_\Omega$. Similarly, under the alternative hypothesis, the received signal has the PDF

$$p\left(\mathbf{x} \mid \mathcal{H}_1\right) = \frac{1}{\sqrt{\pi^{2\Omega}\,|\mathbf{C_{xx}}|}} \exp\left(-\frac{1}{2}\mathbf{x}^H \mathbf{C}_{\mathbf{xx}}^{-1}\mathbf{x}\right) \tag{5.6}$$

where in this case, from (5.3), the covariance matrix of the received signal is: $\mathbf{C_{xx}} = \mathbf{S}\mathbf{C}_{\alpha\alpha}\mathbf{S}^H + \mathbf{C_{ww}}$ since $\boldsymbol{\alpha}$ and $\mathbf{w}$ are independent, where $\mathbf{C}_{\alpha\alpha}$ is the covariance matrix of $\boldsymbol{\alpha}$.

Since the reflectivity coefficients with respect to each sensor are mutually independent, the covariance matrix $\mathbf{C}_{\boldsymbol{\alpha\alpha}}$ takes the form $\mathbf{C}_{\alpha\alpha} = \operatorname{diag}\left(\sigma_{\alpha_1}^2, \sigma_{\alpha_2}^2, \ldots, \sigma_{\alpha_Q}^2\right)$ which leads to a block diagonal structure of the covariance matrix $\mathbf{C_{xx}}$ with the q^{th} block that has the dimensions $\zeta \times \zeta$ defined as

$$[\mathbf{C_{xx}}]_q = \sigma_{\alpha_q}^2 \mathbf{s}_q \mathbf{s}_q^H + \sigma_{\mathbf{w}}^2 \mathbf{I}_\zeta \tag{5.7}$$

Under the alternative hypothesis (5.6), the log-likelihood function is

$$\mathcal{L}\left(p\left(\mathbf{x} \mid \mathcal{H}_1\right)\right) = -2\ln(\pi) - \frac{1}{2}\ln|\mathbf{C_{xx}}| - \frac{1}{2}\mathbf{x}^H \mathbf{C}_{\mathbf{xx}}^{-1}\mathbf{x} \tag{5.8}$$

where the quadratic term of the likelihood function is written and simplified using the Matrix inversion lemma as

$$\begin{aligned} \mathbf{x}^H \mathbf{C}_{\mathbf{xx}}^{-1}\mathbf{x} &= \sum_{q=1}^{Q} \mathbf{x}_q^H \left(\sigma_{\alpha_q}^2 \mathbf{s}_q \mathbf{s}_q^H + \sigma_{\mathbf{w}}^2 \mathbf{I}_\zeta\right)^{-1} \mathbf{x}_q \\ &= \sum_{q=1}^{Q} \mathbf{x}_q^H \left(\frac{1}{\sigma_{\mathbf{w}}^2}\mathbf{I}_\zeta - \frac{\sigma_{\alpha_q}^2/\sigma_{\mathbf{w}}^2}{\sigma_{\mathbf{w}}^2 + \zeta\sigma_{\alpha_q}^2}\mathbf{s}_q \mathbf{s}_q^H\right) \mathbf{x}_q. \end{aligned} \tag{5.9}$$

Similarly, using the Matrix determinant lemma, the logarithmic term can be written as

$$\begin{aligned}\ln|\mathbf{C_{xx}}| &= \ln\left(\prod_{q=1}^{Q}\left|\sigma_{\alpha_q}^2\mathbf{s}_q\mathbf{s}_q^H+\sigma_{\mathbf{w}}^2\mathbf{I}_\zeta\right|\right)\\ &= \sum_{q=1}^{Q}\ln\left(\left|\sigma_{\alpha_q}^2\mathbf{s}_q\mathbf{s}_q^H+\sigma_{\mathbf{w}}^2\mathbf{I}_\zeta\right|\right)\\ &= \ln|\mathbf{C_{ww}}|+\sum_{q=1}^{Q}\ln\left(1+\zeta\frac{\sigma_{\alpha_q^2}^2}{\sigma_{\mathbf{w}}^2}\right).\end{aligned} \tag{5.10}$$

Accordingly, considering the binary hypothesis test in (5.4), the optimum detector based on GLRT is obtained by

$$t_{\text{GLRT}} = \ln\left\{\frac{\max\limits_{\sigma_{\alpha_1}^2,\sigma_{\alpha_2}^2,\cdots,\sigma_{\alpha_Q}^2}\prod_{m=1}^{M}\left(p(\mathbf{x}^{(m)}\mid\mathcal{H}_1)\right)}{\prod_{m=1}^{M}p(\mathbf{x}^{(m)}\mid\mathcal{H}_0)}\right\}\underset{\mathcal{H}_0}{\overset{\mathcal{H}_1}{\gtrless}}\eta \tag{5.11}$$

Using (5.9) and (5.10), the GLRT in (5.11) can be expanded in terms of the received signal of all chirps and sensors as

$$\begin{aligned}t_{\text{GLRT}} &= \sum_{m=1}^{M}\left\{\mathbf{x}^{(m)^H}\left(\mathbf{C}_{\mathbf{w}}^{-1}-\hat{\mathbf{C}}_{\mathbf{xx}}^{-1}\right)\mathbf{x}^{(m)}+\ln|\mathbf{C_{ww}}|-\ln\left|\hat{\mathbf{C}}_{\mathbf{xx}}\right|\right\}\underset{\mathcal{H}_0}{\overset{\mathcal{H}_1}{\gtrless}}2\eta\\ &= \sum_{m=1}^{M}\left\{\sum_{q=1}^{Q}\mathbf{x}_q^{(m)^H}\left(\frac{\hat{\sigma}_{\alpha_q}^2/\sigma_{\mathbf{w}}^2}{\sigma_{\mathbf{w}}^2+\zeta\hat{\sigma}_{\alpha_q}^2}\mathbf{s}_q\mathbf{s}_q^H\right)\mathbf{x}_q^{(m)}-\sum_{q=1}^{Q}\ln\left(1+\zeta\frac{\hat{\sigma}_{\alpha_q^2}^2}{\sigma_{\mathbf{w}}^2}\right)\right\}\underset{\mathcal{H}_0}{\overset{\mathcal{H}_1}{\gtrless}}2\eta\\ &= \sum_{m=1}^{M}\left\{\sum_{q=1}^{Q}\left(\frac{\hat{\sigma}_{\alpha_q}^2/\sigma_{\mathbf{w}}^2}{\sigma_{\mathbf{w}}^2+\zeta\hat{\sigma}_{\alpha_q}^2}\right)\left\|\mathbf{s}_q^H\mathbf{x}_q^{(m)}\right\|_2^2-\sum_{q=1}^{Q}\ln\left(1+\zeta\frac{\hat{\sigma}_{\alpha_q^2}^2}{\sigma_{\mathbf{w}}^2}\right)\right\}\underset{\mathcal{H}_0}{\overset{\mathcal{H}_1}{\gtrless}}2\eta\end{aligned} \tag{5.12}$$

where $\hat{\mathbf{C}}_{\mathbf{xx}}$ is the estimated covariance matrix constructed by the estimated values of $\hat{\sigma}_{\alpha_q}^2$ through MLE by minimizing the negative likelihood $-\mathcal{L}\left(\prod_{m=1}^{M}\left(p\left(\mathbf{x}^{(m)}\mid\mathcal{H}_1\right)\right)\right)$ with respect to $\sigma_{\alpha_q}^2$. Note that this minimization can be

done separately for each $\sigma^2_{\alpha_q}$ since they are independent. More specifically,

$$\begin{aligned}\hat{\sigma}^2_{\alpha_q} &= \min_{\sigma^2_{\alpha_q}} \left\{ -\mathcal{L}\left(\prod_{m=1}^{M} p\left(\mathbf{x}^{(m)} \mid \mathcal{H}_1 \right) \right) \right\} \\ &= \min_{\sigma^2_{\alpha_q}} \left\{ \sum_{m=1}^{M} \mathbf{x}_q^{(m)^H} \left(\frac{\sigma^2_{\alpha_q}/\sigma^2_{\mathbf{w}}}{\sigma^2_{\mathbf{w}} + \zeta\sigma^2_{\alpha_q}} \mathbf{s}_q \mathbf{s}_q^H \right) \mathbf{x}_q^{(m)} - \ln\left(1 + \zeta \frac{\sigma^2_{\alpha_q}}{\sigma^2_{\mathbf{w}}} \right) \right\}\end{aligned} \tag{5.13}$$

Solving for $\sigma^2_{\alpha_q}$, yields the solution

$$\hat{\sigma}^2_{\alpha_q} = \frac{\frac{1}{M}\sum_{m=1}^{M} \left\| \mathbf{s}_q^H \mathbf{x}_q^{(m)} \right\|_2^2 - \zeta\sigma^2_{\mathbf{w}}}{\zeta^2} \tag{5.14}$$

which is the estimation of signal power at the q^{th} sensor. The MLE estimate above requires knowledge of the noise power that is estimated using secondary data in adjacent cells free of a target $\mathbf{X}_{sec}$ as $\sigma^2_{\mathbf{w}} = \text{tr}\left[\frac{1}{M}\sum_{m=1}^{M} \mathbf{X}_{sec}\mathbf{X}_{sec}^H \right] / \Omega$.

It is noted from (5.12) that the GLRT test is a weighted sum of the square output of the matched filter of different sensors where the weights are proportional to the local SNRs available at the sensors, as suggested in the literature. In the sequel, the performance of the proposed detector is analyzed numerically.

5.4 Numerical Analysis

In this section, we evaluate the proposed GLRT detector numerically using Monte Carlo simulations. The detector's performance is demonstrated through the use of ROC curves. Our proposed detector is compared to the conventional detector for fluctuating targets, which comprises square-law detectors at each sensor, with their output being non-coherently integrated [105]. Throughout this section, we consider distributed sensors, each equipped with $N_{tx} = 2$ transmitting antennas and $N_{rx} = 3$ receiving antennas for the different configurations and scenarios considered. We also considered the Radio Frequency (RF) parameters of the sensors that match the operating parameters for TI IWR6843ISK radar [106].

First, in Figure 5.1, with $Q = 4$ sensors, an average post-processing $\text{SNR}_{\text{post}} = 13$ dB, and $M = 3Q$ chirps, we show the performance of the GLRT detector for three cases of variance in aspect angle dependence of the fluctuating targets. In addition to the ROC of the conventional detector, we show the ROC of the optimum LRT detector for multistatic radars [102] which assumes perfect knowledge of the local SNR at each

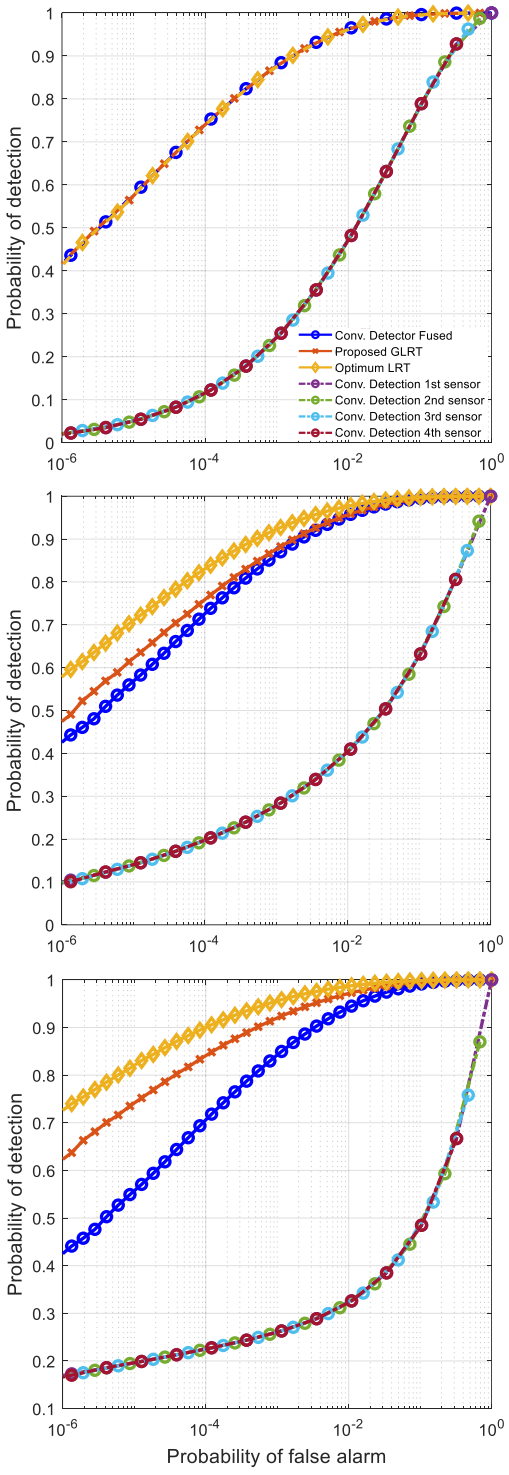

Figure 5.1: ROC curves for the proposed GLRT detector compared with conventional and optimum LRT detectors where $Q = 4$, $M = 3Q$, $\text{SNR}_{post} = 13$ dB for a fluctuating target with **Top:** isotropic RCS, **Middle:** Aspect-dependent RCS with maximum variation 10 dB, **Bottom:** Aspect-dependent RCS with maximum variation 20 dB.

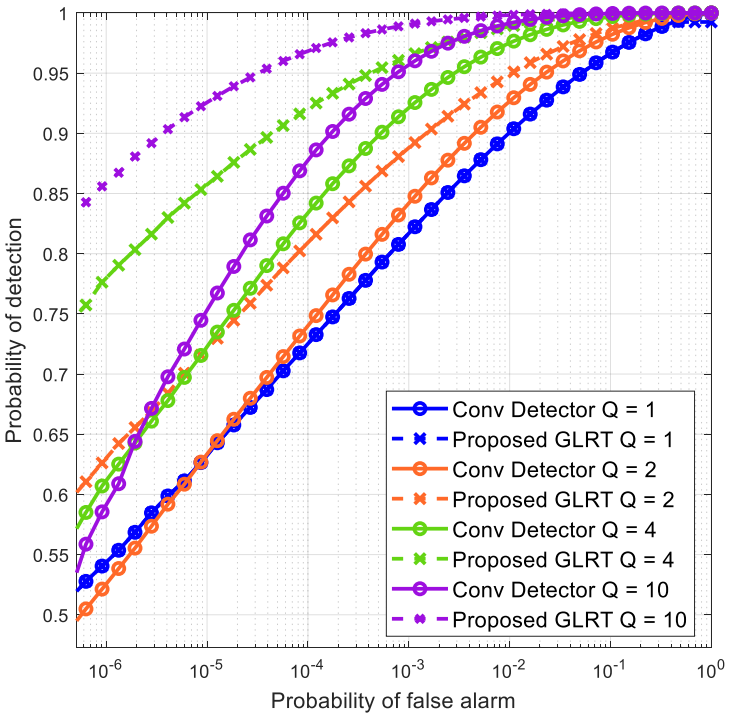

Figure 5.2: ROC curves of the proposed GLRT detector versus the number of distributed sensors, $\text{SNR}_{post} = 13$ dB, $M = 3Q$.

sensor. The target in Figure 5.1(a) is assumed to be fluctuating with the same average power $\sigma_{\alpha_q^2}$ with respect to all sensors (isotropic). Accordingly, as expected, all three detectors manifest the same performance since the optimum test weights the output of the matched filters of each sensor equally which is equivalent to the conventional detector that applies no weighting. On the other hand, in Figure 5.1(b) and Figure 5.1(c), the RCS is assumed aspect-dependent with its value varying in a range of 10 dB and 20 dB, respectively. The depicted performance suggests that the proposed detector is crucial when RCS varies dramatically with aspect angle. Moreover, Figure 5.1(c) shows that the proposed detector may achieve asymptotically the performance of the optimum detector which assumes perfect knowledge of local SNR in extreme cases of RCS aspect variance. We also included the detection performance of individual sensors with no fusion; in the figure, this is clearly inferior since the total SNR comes from the integration of all sensors.

Figure 5.2 illustrates the performance of the proposed detector versus the number of distributed sensors while keeping the post-processing SNR identical, and the number of integrated chirps $M = 3Q$. Needless to mention, the proposed detector does not bring any gain in performance with respect to the conventional one in the case of $Q = 1$ since

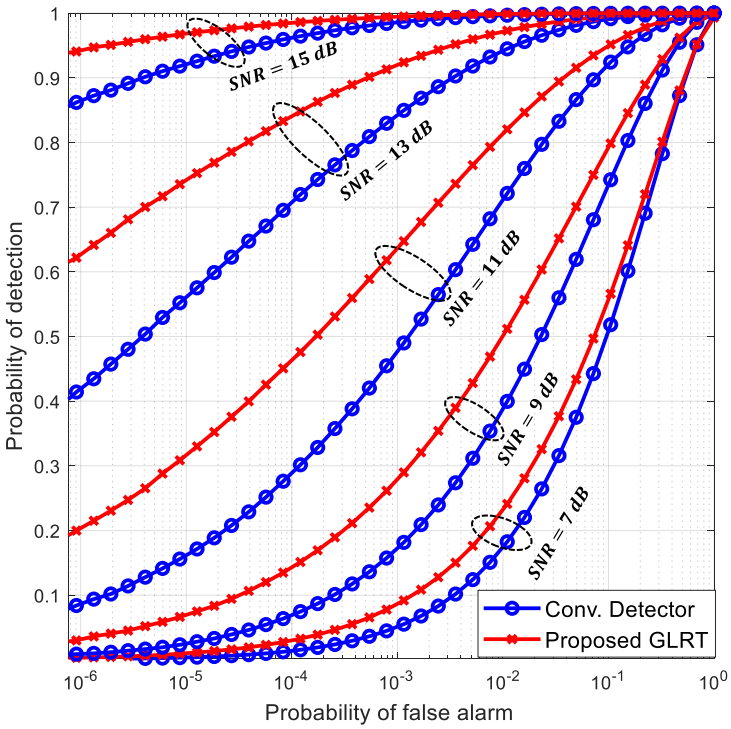

Figure 5.3: ROC curves of the proposed GLRT detector versus different values of post-processing SNR, $Q = 4$, $M = 3Q$

no angle diversity is exploited. Likewise, it can be also anticipated that the larger the number of sensors, the higher gain is obtained by the proposed detector relying on more measurements with high average power and weighing the unfavorable ones less.

Similarly, the performance of the detector versus different values of SNR_{post} and different number of chirps M while keeping $Q = 4$ is depicted in Figure 5.3 and Figure 5.4, respectively. It can be observed that the proposed detector provides the highest gain in the mid-range of SNR values. This can be attributed to the fact that, at very low SNR values, most of the received signals from different sensors are inadequate for detection. Also, for very high SNR values, all the received signals from different sensors can be highly reliable for detection. This makes weighting in both cases of high and low SNR not bring excessive gain in performance. On the other hand, increasing the number of chirps enhances the estimation of the received signal power in each sensor which leads to better performance of the proposed detector. Note that as seen in Figure 5.4, a few chirps as low as the number of sensors is sufficient to realize a performance gain with the proposed detector.

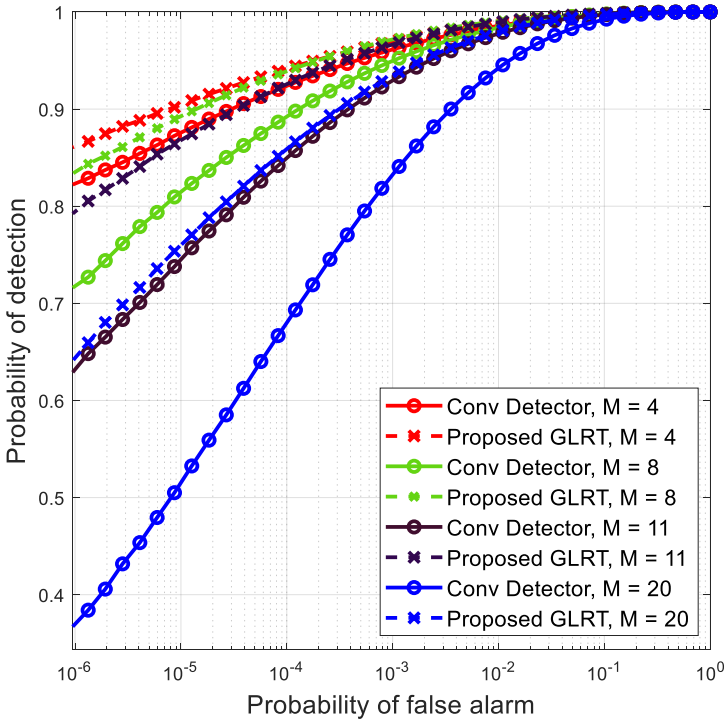

Figure 5.4: ROC curves of the proposed GLRT detector versus the number of integrated chirps, $\text{SNR}_{post} = 13$ dB, $Q = 4$

5.5 Conclusion

In this chapter, we developed a GLRT detector for aspect-dependent fluctuating targets observed by widely distributed MIMO radar sensors. Leveraging the received signal from multiple chirps, we estimated the average received signal power at each sensor using MLE, which was then utilized in the likelihood ratio test to derive the GLRT detector. The resulting detector is a weighted sum of individual tests at each sensor, with weights proportional to the local SNR values that vary significantly due to differences in RCS across various aspect angles and path losses towards each sensor.

Through Monte-Carlo simulations, we evaluated the performance of the proposed detector and demonstrated its superiority over conventional detectors that employ non-coherent integration of processed chirps and equal aggregation of tests from each sensor's received signal. Our simulations revealed that in scenarios where the RCS of targets significantly differs, the proposed detector asymptotically achieves optimal performance with perfect knowledge of local SNR values. Additionally, we conducted simulations to analyze the proposed detector's performance concerning post-processing SNR, the number of distributed sensors, and the number of integrated chirps, providing valuable insights for practical implementation and system optimization.

Chapter 6

Occlusion-Informed Detection

Employing mmWave radar systems with high-angular resolution in occlusion-prone scenarios often results in sparse signal returns along range profiles. In extreme cases, only one target return may be observed, as the resolution grid size becomes significantly smaller than the targets, causing portions of the targets to consistently occupy the full area of a test cell and occluding the region beyond it. Leveraging this structure, we propose two detectors to enhance the detection of non-occluded targets in such scenarios, thereby providing accurate high-resolution point clouds. The first method employs multiple hypothesis testing over each range profile where the range cells within are considered mutually occluding. The second is formulated based on binary hypothesis testing for each cell, considering the distribution of the signal in the other cells within the same range profile. Numerical analysis demonstrates the superior performance of the latter method over both the classic detection and the former method, especially in low SNR scenarios. Our work showcases the potential of occlusion-informed detection in imaging radars to improve the detection probability of non-occluded targets and reduce false alarms in challenging indoor environments.

6.1 Introduction

Over the past few years, there has been a surge of interest in mmWave MIMO radar sensors, especially for their applications in indoor sensing. These applications include tasks such as human detection and activity recognition, monitoring vital signs, fall detection, and real-time tracking of multiple individuals simultaneously, as demonstrated in [99],[14], [107], and [100], respectively. Advancements in mmWave sensor manufacturing technology have made such tasks possible. This development has led to the production of affordable single-chip radar sensors incorporating a large number of an-

tenna elements, facilitating high angular resolution and resulting in the emergence of a category of imaging radars (see, for example, [16, 17]). Moreover, the optimization of various MIMO waveforms has enabled the attainment of enhanced angular performance which is an essential feature for many of the aforementioned tasks. Examples of different proposed MIMO waveforms are presented in [108–111].

When monitoring human targets in indoor environments, the detection performance, preferably of the full body, holds paramount importance for various applications. However, in typical crowded indoor settings, the likelihood of occluding human targets or substantial portions of their bodies is quite high, posing a significant challenge for achieving satisfactory performance across all these applications [24, 112–114].

In the realm of automotive perception, occlusion remedies involve multi-modal fusion, where occlusion scenarios are modeled by combining radar measurements with other sensors like stereo cameras, as seen in [115], or LIDAR, as demonstrated in [116]. On the other hand, within indoor applications, several studies have proposed distributed radar sensor architectures that enhance detection capabilities of occluded targets significantly through the exploitation of spatial diversity [39, 42, 53, 117].

While distributed sensors are essential to detect occluded targets, further measures can be taken to combat occlusion. In the context of tracking multiple individuals with distributed sensors, occlusion events concerning one sensor can lead to the division of a single track into multiple tracks. A solution, proposed in [118, 119], involves overcoming this issue by fusing track information instead of detection points in the fusion center. On another note, to better account for the capture of the Doppler falling signatures, while limiting occlusion events, the authors in [120] analyzed different sensor placements and showed that wall-mounting of distributed sensors at a low level is favorable to optimize the extraction of both range and micro-Doppler information necessary to detect falling events. While the placement of sensors to minimize occlusion is also considered by the authors in [24], their proposed gait recognition classifier is adjusted to make decisions based on features expected to be least affected by the occlusion. Similarly, in [112], the authors employed an architecture featuring separate transmitting and receiving antennas for vital sign monitoring. Using this bi-static setup, they determined the angular and distance separation of multiple targets to minimize mutual occlusion, resulting in effective vital sign monitoring with the transmission of a single beam or steered multiple beams.

The studies mentioned above effectively tackle detection limitations arising from occlusion and propose methods to generate high-resolution detection point clouds. However, to the best of our knowledge, no study explicitly leverages the structure of in-

dividual range profile signals under occlusion in the hypothesis testing formulation of the detection problem. This structure is inherently sparse, particularly when utilizing high-angular resolution systems, and incorporating it could significantly enhance the detection capabilities of non-occluded targets, as occlusion would be evident across each angular bin of the test grid. A significant body of literature exists on exploiting scene sparsity in radar image reconstruction (see, for example, [121–128]), which is often motivated by the typical low number of targets in the scene in addition to the properties of electromagnetic backscattering, including occlusion phenomenon [121, 123]. However, these methods rely on compressive sensing theory and involve solving inverse problems which usually require hyperparameter tuning and results in iterative algorithms, rendering them computationally and time expensive, unsuitable for real-time applications in many cases as shown in Chapter 2.

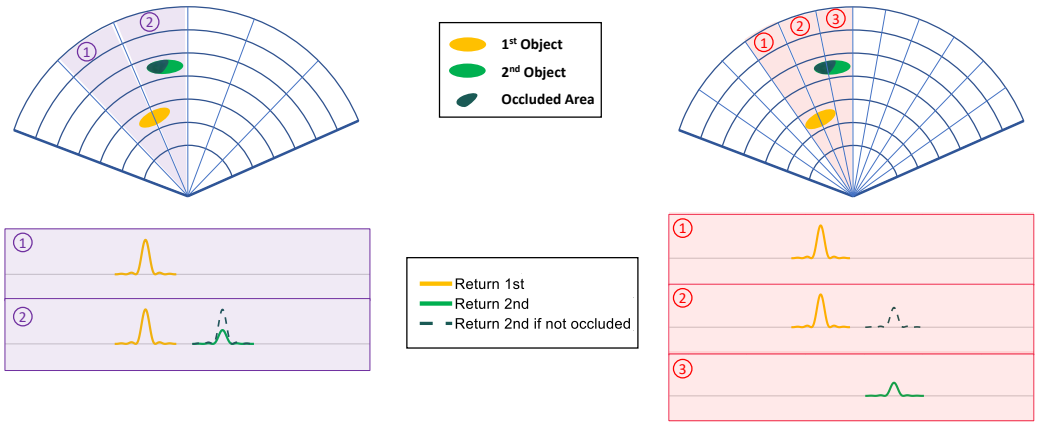

Figure 6.1: 2D Range-Azimuth grid map illustrating the sparsity of range profiles relative to targets' size in an occlusion-prone sensing environment. Two targets in the scene, with one occluding part of the other, are observed by two sensors with different angular resolutions, depicted by the corresponding angular grid sizes. **Left:** Sensor with low angular resolution ($\delta\theta_1$) relative to targets' size. **Right:** Sensor with high angular resolution ($\delta\theta_2 = 0.5\ \delta\theta_1$) relative to targets' size.

In this chapter, we demonstrate that leveraging the sparse structure in a hypothesis testing-based formulation provides a statistical detector that enhances the detection performance for non-occluded targets observed by a single sensor, resulting in accurate high-resolution point clouds. This improved detection at the sensor level would aggregate across a network of sensors, leading to an overall enhancement in detection at a low computational cost. We capitalize on the phenomenon that in a sensing system susceptible to occlusion, conducting detection over a dense angular grid yields limited return responses across multiple range cells within the same angular bin. Consequently,

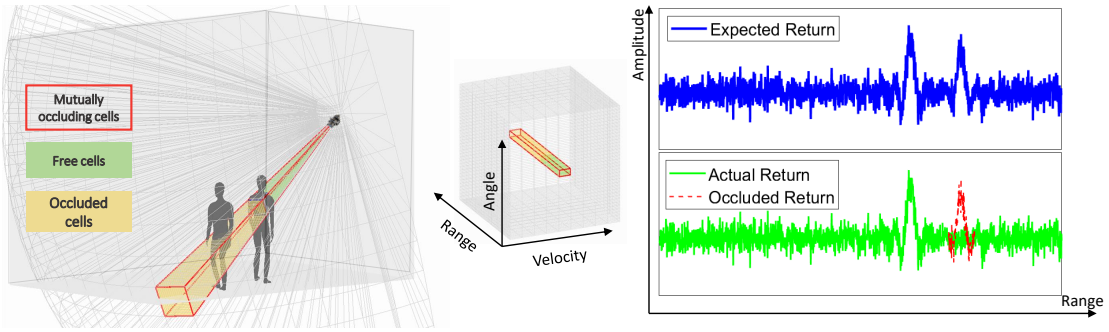

Figure 6.2: 3D Demonstration of a full occlusion scenario over a range profile in an indoor environment observed with a mmWave sensor featuring high angular resolution. **Left:** Layout of the scene with the detection grid showing the sensor's view and highlighted group of mutually occluding cells. **Middle:** Corresponding radar cube. **Right:** Expected and actual signal returns in the group of highlighted cells.

we design detectors to enhance the probability of detection versus false alarms for fully observed target areas. These detectors assume complete occupancy of an angular resolution cell, implying full occlusion of any potential object that may exist behind the occupied cell within each range profile. This assumption can be justified considering system parameters such as angular resolution and transmission frequency relative to target size.

Figure 6.1 presents a schematic illustrating the relationship between system parameters and the sparsity of range profiles in sensing under occlusion. The figure depicts a 2D elevation cut of a range-angle detection grid map from two sensors. The sensor on the right is assumed to have double the number of antenna elements, resulting in half the angular resolution compared to the sensor on the left. Both sensors observe the same scene and operate at the same frequency, indicating that the transmitted waves from both possess identical scattering/penetration characteristics. As a result, the occlusion in the scene will be consistent for both sensors. However, due to the higher angular resolution of the sensor on the right, detection tests are conducted on a finer grid. Consequently, the associated responses over range profiles are expected to be more sparse since targets are dispersed on different angular bins. The figure highlights the angular bins containing targets under each system, with their ideal range profiles depicted below the corresponding grid map.

The sparsity of range profiles arises from both the occlusion phenomenon and the size of the angular grid relative to the target size. If occlusion does not occur, all targets would induce a response in the range profile of each angular bin. Similarly, if the sensor's angular resolution does not permit detection cells significantly smaller than

the target size, a single range profile would contain multiple responses from targets over a wider angle range, even if parts are occluded. Ultimately, when using an imaging radar, angular bins are anticipated to be fully occupied by a portion of the target at the respective location, leading to sparse range profiles, as they consist of a group of mutually occluding cells.

Similarly, Figure 6.2 illustrates the same concept in an indoor scenario involving human targets, where detection is conducted over a 3D detection grid map. The figure highlights one range profile consisting of mutually occluding cells situated on the same azimuth and elevation angle. The presence of a target (or a portion thereof) in one of these cells closer to the sensor would obstruct targets that may exist in any other cell within the same group. In such instances, the reception of echoes of the transmitted wave from potential targets in those cells is physically impeded. Henceforth, throughout the chapter, we will refer to this scenario as a "full occlusion" scenario.

Accordingly, leveraging the sparse structure of range profiles, we introduce two detectors based on distinct formulations of hypothesis testing. The first approach utilizes multiple hypothesis testing, framing the detection problem to closely match the full occlusion scenario. This involves deciding that the presence of a target will be in only one cell of each range profile, based on the assumption of full occlusion. On the other hand, the second approach is constructed using binary hypothesis testing. Here, the alternative and null hypotheses for each cell are established with consideration for the likelihood of the signal in the remaining cells within the same group of mutually occluding cells. For each of these formulations, we derive both Maximum A Posteriori (MAP) and Maximum Likelihood (ML) detectors. The MAP detector assumes prior knowledge of the probability model and values associated with targets' presence in different cells and utilizes this information in decision-making. On the other hand, the ML detector lacks such knowledge and assumes equal probabilities of targets arriving in the group of mutually occluding cells. While the multiple hypothesis formulation represents the straightforward, intuitive method, the binary formulation exhibits superior performance, as will be demonstrated in our numerical simulations.

The contributions of this chapter are summarized as follows:

1. Identification and modeling of range profile structure under occlusion, utilizing probabilistic models of target presence within the detection grid cells.

2. Development of corresponding detectors using hypothesis testing, accommodating both knowledge of the generating probabilistic models and the lack thereof.

3. Performance evaluation of the proposed detectors, demonstrated through ROC

curves obtained numerically via Monte Carlo simulations. These simulations are based on signal generation from defined models and evaluated under various model parameters, SNR values, and sizes of range profiles.

4. Implementation of the proposed detectors on scenario-based simulated data, where a realistic indoor scenario is modeled in 3D, and the radar signal is generated using ray-tracing simulations.

Notations Throughout this chapter, lowercase bold font is used to denote vectors. $\mathbf{I}_N$ represents the identity matrix of size $N \times N$, and $\mathbf{0}_N$ is a vector of all zeros of size $N \times 1$. The superscripts $(.)^T$ and $(.)^H$ denote, respectively, the transpose and the complex conjugate transpose of a vector or a matrix. The operators $|.|$, $\otimes$, $\Re$, and $det(.)$ are used for the absolute value operator, Kronecker product, the real part of a complex value, and the matrix determinant, respectively. With $p(x)$, we denote the probability density function of an observation x from a random variable X, where the random variable subscript is omitted for simplicity. We define the set of natural numbers from 1 to N as $\{N\} = \{1, 2, \ldots, N\}$. Accordingly, a vector with subscript $\{N\}$, e.g., $\mathbf{x}_{\{N\}}$, denotes the stacked vectors $[\mathbf{x}_1^T, \mathbf{x}_2^T, \cdots, \mathbf{x}_N^T]^T$. To shorten equations, we contract the exponential component of a Gaussian PDF for a random vector $\mathbf{x}$ with a mean μ and variance σ^2 using the notation $e_{\sigma^2}(\mathbf{x}, \mu) = \exp\left(\frac{-(\mathbf{x}-\mu)^H(\mathbf{x}-\mu)}{\sigma^2}\right)$.

6.2 System Model

We consider a mmWave MIMO radar sensor having N_{tx} and N_{rx} transmitting and receiving antenna elements, respectively. Assume that $\mathbf{r}_s = [x_s, y_s, z_s]^T$ denotes the absolute position of the sensor, where x, y, and z represent the absolute Cartesian coordinates. In this case, a target with absolute position $\mathbf{r}_t = [x_t, y_t, z_t]^T$ will have a relative distance R_t, azimuth θ_t, and elevation ϕ_t with respect to the sensor. Following appropriate range processing (either through FFT or matched filter), the target processed signal at the range cell—specifically the CUT—corresponding to R_t can be expressed as

$$\mathbf{x}_t = \alpha_t \mathbf{s}(\theta_t, \phi_t) + \mathbf{w} \in \mathbb{C}^{N_{tx}N_{rx} \times 1}. \tag{6.1}$$

Here, $\alpha_t = \sqrt{\frac{p_{tx}G_{tx}G_{rx}\lambda^2\sigma_t}{(4\pi)^3 R^4}}$ represents the amplitude of the reflected signal, encompassing path loss and target RCS, where λ denotes the transmitted signal's wavelength, p_{tx} is the transmit power, G_{tx} and G_{rx} denote the transmit and receive antenna gains, and σ_t is the RCS of the target at the CUT. Additionally, $\mathbf{w}$ denotes the interference signal,

ideally encompassing both clutter and thermal noise, though, in this chapter, we assume $\mathbf{w} \sim \mathcal{CN}(\mathbf{0}, \sigma_{\mathbf{w}}^2\mathbf{I})$ contains only receiver thermal noise. Moreover, the signal steering vector is

$$\mathbf{s}(\theta_t, \phi_t) = \mathbf{a}(\theta_t, \phi_t) \otimes \mathbf{b}(\theta_t, \phi_t), \tag{6.2}$$

where the spatial transmit and receive steering vectors are defined respectively as

$$\mathbf{a}(\theta, \phi) = \begin{bmatrix} e^{-j\mathbf{k}^T(\theta,\phi)\mathbf{r}_{s,1}} \\ e^{-j\mathbf{k}^T(\theta,\phi)\mathbf{r}_{s,2}} \\ \vdots \\ e^{-j\mathbf{k}^T(\theta,\phi)\mathbf{r}_{s,N_{tx}}} \end{bmatrix}, \mathbf{b}(\theta, \phi) = \begin{bmatrix} e^{-j\mathbf{k}^T(\theta,\phi)\mathbf{r}_{s,1}} \\ e^{-j\mathbf{k}^T(\theta,\phi)\mathbf{r}_{s,2}} \\ \vdots \\ e^{-j\mathbf{k}^T(\theta,\phi)\mathbf{r}_{s,N_{rx}}} \end{bmatrix},$$

and $\mathbf{k}(\theta, \phi) = \frac{2\pi}{\lambda}[\cos\theta\cos\phi, \sin\theta\cos\phi, \sin\phi]^T$ is the wave-number vector with λ being the wavelength of the transmitted wave, θ and ϕ are the azimuth and elevation angles, respectively, and $\mathbf{r}_{s,n_{tx}}$ and $\mathbf{r}_{s,n_{rx}}$ are the locations of the radar transmit and receive antenna elements, respectively.

Since our focus is on designing a detector for scenarios involving full occlusion, it is crucial to model the probability of signal returns at each cell under such conditions. These probabilities can be derived by establishing a probability model for the presence of targets in each cell. Consequently, we outline the essential probability components required for the subsequent formulation of the problem. We assume each range profile encompasses a group of N mutually occluding cells. We denote P_k as the probability of the presence of a target at the k^{th} cell, where $k = 1, \ldots, N$, representing the target space probability. Accordingly, the probability of having no target present at any of the N cells is given by

$$P_0 = \prod_{k=1}^{N} (1 - P_k)\,. \tag{6.3}$$

Under the full occlusion assumption over a range profile, among the potential targets in the group of N cells, only one return will be reflected to the radar sensor. As a result, we can express the signal space probabilities of receiving returns at a specific cell based on the probabilities in the target space. Let ρ_k denote the probability of receiving a

return from a target located at the k^{th} cell, then

$$\begin{cases} \rho_0 = P_0 \\ \rho_1 = P_1 \\ \vdots \\ \rho_k = P_k \prod_{i=1}^{i=k-1} (1 - P_i) \end{cases} \tag{6.4}$$

where ρ_0 represents the probability of having no return in any of the cells, and $\sum_{k=0}^{N} \rho_k = 1$. Another useful probability in subsequent calculations is the probability of having a signal return from the k^{th} cell given that a certain n^{th} cell, especially the CUT, has no target return. Denoting this probability as $\rho_{k/\tilde{n}}$, we can compute it using Bayes' theorem as

$$\rho_{k/\tilde{n}} = \frac{\rho_{\tilde{n}/k}\ \rho_k}{\rho_{\tilde{n}}} \tag{6.5}$$

Since $\rho_{\tilde{n}} = 1 - \rho_n$, and by occlusion assumption $\rho_{\tilde{n}/k} = 1$, the probabilities of having a signal return at the k^{th} cell given that a certain n^{th} cell has no return is given by

$$\rho_{k/\tilde{n}} = \frac{\rho_k}{1 - \rho_n}, \quad \forall\ k, n \in \{N\}, k \neq n. \tag{6.6}$$

The aforementioned probabilities in the signal space will be incorporated into the design of the detectors and the evaluation of their performance in the next sections.

6.3 Occlusion-Informed Detector Design

In this section, we will present two formulations of the detection problem under the assumption of full occlusion across a group of cells. First, we will frame the problem as a multiple-hypothesis testing scenario, in line with our assumption that a single target return is expected in all cells. Second, we will approach the problem as a binary hypothesis testing situation at the CUT, taking into account the signal distribution in the other cells. In both cases, we will develop the MAP and ML detectors. The MAP detector assumes that knowledge of the probability model and values is available and utilizes this information for detection. In contrast, the ML detector lacks such knowledge and assumes equal probabilities of events [129].

6.3.1 Multiple Hypothesis Testing Design

Casting the problem as an M-ary detection problem is supposed to be a closer match under the assumption of full occlusion where we expect a single echo return in one of

N cells in the range profile. Accordingly, we consider $M = N + 1$ hypotheses over the entire group of cells modeled as

$$\mathcal{H}_k : \mathbf{x}_{\{N\}} = \mu_k + \mathbf{w}_{\{N\}} \quad \forall\ k \in \{N\} \tag{6.7}$$

where $\mathbf{x}_{\{N\}}$ is the stacked vector of all the processed signals at the group of N cells, $\mathbf{w}_{\{N\}}$ is a stacked vector of the noise, and μ_k is a vector of size $LN \times 1$ defined as

$$\begin{aligned} \mu_k &= [\mathbf{0}_L^T \dots \mathbf{s}_k^T \dots \mathbf{0}_L^T]^T \qquad && \forall\ k \in \{N\} \\ \mu_k &= \mathbf{0}_{LN} && k = 0 \end{aligned} \tag{6.8}$$

where $L = N_{tx}\ N_{rx}$. The construction of μ_k in (6.8) for $k \neq 0$ ensures that it contains zero elements everywhere except for elements with indices in the range of $[L(k-1)+1, Lk]$ that are populated by $\mathbf{s}_k$, where $\mathbf{s}_k = \alpha_k \mathbf{s}$, and $\mathbf{s}$ is the normalized steering vector towards the k^{th} cell. Please note that we have dropped the dependence on θ_k and ϕ_k. This is due to our assumption that the group of mutually occluding cells lies at the same azimuth and elevation angle.

By considering the signal space probabilities defined in (6.4), the optimum decision rule which minimizes the average error probability is the one that decides that $\mathbf{x}_{\{N\}}$ is generated according to $\mathcal{H}_k$ if $\rho_k p\left(\mathbf{x}_{\{N\}}|\mathcal{H}_k\right) = \max\limits_j \left\{\rho_j\ p\left(\mathbf{x}_{\{N\}}|\mathcal{H}_j\right)\right\}$ [129].

Recalling the Gaussian PDF notation $e_{\sigma^2}(\mathbf{x}, \mu)$, the hypotheses formulation in (6.7) leads to the following likelihood

$$p\left(\mathbf{x}_{\{N\}}|\mathcal{H}_k\right) = \zeta e_{\sigma_{\mathbf{w}}^2}\left(\mathbf{x}_{\{N\}}, \mu_k\right), \tag{6.9}$$

where $\zeta = 1/(\pi^{LN} det(\sigma_{\mathbf{w}}^2 \mathbf{I}_{LN}))$. This likelihood can be simplified based on the signal model (6.1) as

$$p\left(\mathbf{x}_{\{N\}}|\mathcal{H}_k\right) = \begin{cases} \zeta e_{\sigma_{\mathbf{w}}^2}\left(\mathbf{x}_{\{\bar{N}\}}, \mathbf{0}_{L(N-1)}\right) & k = 0 \\ \zeta e_{\sigma_{\mathbf{w}}^2}\left(\mathbf{x}_{\{\bar{N}\}}, \mathbf{0}_{L(N-1)}\right) \cdot \exp\left(\dfrac{2\Re\{\mathbf{s}_k^H \mathbf{x}_k\} - \mathbf{s}_k^H \mathbf{s}_k}{\sigma_{\mathbf{w}}^2}\right) & k \in \{N\} \end{cases} \tag{6.10}$$

Accordingly, the optimum M-ary MAP detector under full occlusion formulation is the

following

$$\begin{aligned}&\text{Decide } \mathcal{H}_k \text{ if } \Gamma_k^{\text{MAP}} = \max_j \{\Gamma_j^{\text{MAP}}\} \quad \forall\ j \in \{\{N\}, 0\}\\ &\text{where}\\ &\Gamma_j^{\text{MAP}} = \rho_j\ p\left(\mathbf{x}_{\{N\}}|\mathcal{H}_j\right)/e_{\sigma_{\mathbf{w}}^2}\left(\mathbf{x}_{\{\bar{N}\}}, \mathbf{0}_{L(N-1)}\right).\end{aligned} \tag{6.11}$$

The test (6.11) assumes the knowledge of the mean of signals $\mathbf{s}_j = \alpha_j \mathbf{s}$ where is $\mathbf{s}$ is the known steering vector and α_j is the target's RCS, often unknown. In this context, the corresponding GLRT detector is used wherein $\hat{\alpha}_j$ is estimated for each cell through MLE of the likelihood function under each hypothesis $\mathcal{H}_j$. The estimation results in $\hat{\alpha}_j = \mathbf{s}^H \mathbf{x}_j$ leading to $\hat{\mathbf{s}}_j = \mathbf{s}^H \mathbf{x}_j \mathbf{s}$ and a corresponding GLRT detector $\Gamma_j^{\text{MAP}} = \rho_j \exp\left(|\mathbf{s}^H \mathbf{x}_j|^2/\sigma_{\mathbf{w}}^2\right)$ for $j = 1, \ldots, N$.

The ML equivalent detector is obtained by assuming equal probabilities of signal returns at all cells, namely, $\rho_j = \rho_i\ \forall j, i \in \{N\}, j \neq i$. This simply translates to the following decision rule

$$\begin{aligned}&\text{Decide } \mathcal{H}_k \text{ if } \Gamma_k^{\text{ML}} = \max_j \{\Gamma_j^{\text{ML}}\} \quad \forall\ j \in \{\{N\}, 0\}\\ &\text{where}\\ &\Gamma_j^{\text{ML}} = \begin{cases} 1 & j = 0 \\ \exp\left(|\mathbf{s}^H \mathbf{x}_j|^2/\sigma_{\mathbf{w}}^2\right) & j \in \{N\}. \end{cases}\end{aligned} \tag{6.12}$$

Note that in both (6.11) and (6.12), the noise power $\sigma_{\mathbf{w}}^2$ is assumed to be known, which is typically estimated using secondary cells in practice. Moreover, from (6.12), it is evident that the resulting ML detector is equivalent to implementing a classic square law detector on the signal after angle match filtering at each cell. It then decides on the target presence at the cell with the maximum value of such a test among all the cells related to the same range profile. Accordingly, from now on, we will refer to this detector as the MAX detector.

6.3.2 Binary Hypothesis Testing Design

In this section, we approach the detector design problem through binary hypothesis testing, where tests are formulated for each cell by considering the distribution of the processed signal across all the N cells within the same range profile. First, let us define the simple binary hypothesis without occlusion modeling for an arbitrary cell k. The

range processed signal under $\mathcal{H}_0$ and $\mathcal{H}_1$ can be expressed as

$$\begin{cases} \mathcal{H}_1 : \mathbf{x}_k = \alpha_k \mathbf{s} + \mathbf{w}_k \\ \mathcal{H}_0 : \mathbf{x}_k = \mathbf{w}_k \end{cases} \tag{6.13}$$

This formulation leads to the classical GLRT detector

$$\exp\left(\frac{|\mathbf{s}^H \mathbf{x}_k|^2}{\sigma_{\mathbf{w}}^2}\right) \underset{\mathcal{H}_0}{\overset{\mathcal{H}_1}{\gtrless}} \eta. \tag{6.14}$$

Now, we formulate the signal model under both hypotheses given the assumption of full occlusion across the range profile containing N cells. To account for signals from cells other than the CUT, we introduce a superscript n indicating the index of the CUT. Specifically, $\mathcal{H}_1^{(n)}$ and $\mathcal{H}_0^{(n)}$ represent the alternative and null hypotheses, respectively, when the n^{th} cell is the CUT. Thus, the detection problem under occlusion can be framed as testing the following hypotheses

$$\begin{cases} \mathcal{H}_1^{(n)} : (\mathbf{x}_n = \ \mathbf{s}_n + \mathbf{w} \ , \mathbf{x}_k = \mathbf{w}) \quad \forall \ k \in \{N\} \setminus n \\ \mathcal{H}_0^{(n)} : \begin{cases} (\mathbf{x}_n = \ \mathbf{w} \ , \mathbf{x}_k = \mathbf{w}) \quad \forall \ k \in \{N\} \setminus n \\ \quad \text{(OR)} \\ (\mathbf{x}_n = \ \mathbf{w} \ , \mathbf{x}_k = \mathbf{w}, \ \mathbf{x}_j = \mathbf{s}_j + \mathbf{w}) \\ \quad \forall \ k \in \{N\} \setminus \{n, j\} \end{cases} \end{cases} \tag{6.15}$$

The formulation above indicates that under the alternative hypothesis, the CUT contains a signal due to the presence of a target at that cell, while all the other $N-1$ cells will only contain noise. Conversely, under the null hypothesis, the CUT contains only noise, while all the other cells may also contain only noise, or at most one of them may contain a target obstructing the signal of potential targets in other cells, including the CUT.

To derive the detector based on the above formulation, we need to express the likelihoods under each of the hypotheses. Let $\mathbf{x}_{\{\bar{N}\}}$ represent the stacked measurements of the signal related to all cells other than the CUT, where $\{\bar{N}\} := \{N\} \setminus n$, and the size of this set is $N-1$. Therefore, the likelihood under the alternative hypothesis can be formulated as follows

$$p\left(\mathbf{x}_n | \mathcal{H}_1^{(n)}\right) = p\left(\mathbf{x}_n = \mathbf{s}_n + \mathbf{w}, \mathbf{x}_{\{\bar{N}\}} = \mathbf{w}_{\{\bar{N}\}}\right), \tag{6.16}$$

where $\mathbf{w}_{\{\bar{N}\}}$ is the stacked vector of all $(N-1)$ vectors modeling the noise at the cells

other than CUT distributed as $\mathbf{w}_{\{\bar{N}\}} \sim \mathcal{CN}\left(0, \sigma_{\mathbf{w}}^2 \mathbf{I}_{L(N-1)}\right)$. Consequently, (6.16) can be expressed as

$$p\left(\mathbf{x}_n | \mathcal{H}_1^{(n)}\right) = \zeta e_{\sigma_{\mathbf{w}}^2}\left(\mathbf{x}_n, \mathbf{s}_n\right) \cdot e_{\sigma_{\mathbf{w}}^2}\left(\mathbf{x}_{\{\bar{N}\}}, \mathbf{0}_{L(N-1)}\right) \tag{6.17}$$

where $\zeta = 1/(\pi^{LN} det(\sigma_{\mathbf{w}}^2 \mathbf{I}_{LN}))$. Similarly, the likelihood under the null hypothesis can be expressed as

$$p\left(\mathbf{x}_n | \mathcal{H}_0^{(n)}\right) = p\left(\mathbf{x}_n = \mathbf{w}, \left[\mathbf{x}_{\{\bar{N}\}} = \mathbf{w} \text{ (OR) } \mathbf{x}_{\{\bar{N}\}} = \mu_1 + \mathbf{w} \ldots \text{(OR)} \quad \mathbf{x}_{\{\bar{N}\}} = \mu_N + \mathbf{w}\right]\right), \tag{6.18}$$

where μ_k is as defined in (6.8). The likelihood in (6.18) is the joint probability density function of the vector $\mathbf{x}_n$ given it contains noise only and the stacked vector $\mathbf{x}_{\{\bar{N}\}}$ modeled as a Gaussian mixture of signals with the different means μ_k weighted by the probabilities of signal returns at the k^{th} cell defined in (6.6). Consequently, (6.18) can be written as

$$p\left(\mathbf{x}_n | \mathcal{H}_0^{(n)}\right) = \zeta e_{\sigma_{\mathbf{w}}^2}\left(\mathbf{x}_n, \mathbf{0}_L\right) \cdot \sum_{\substack{k=0 \\ k \neq n}}^{N} \rho_{k/\tilde{n}} \; e_{\sigma_{\mathbf{w}}^2}\left(\mathbf{x}_{\{\bar{N}\}}, \mu_k\right). \tag{6.19}$$

Using the likelihoods obtained in (6.16), and (6.18), we derive the detector which is characterized by testing the likelihood ratio Λ of the signal in the CUT given the signals of all other $\bar{N}$ cells against a threshold η as follows

$$\Lambda(\mathbf{x}_n | \mathbf{x}_{\{\bar{N}\}}) = \frac{p\left(\mathbf{x}_n | \mathcal{H}_1^{(n)}\right)}{p\left(\mathbf{x}_n | \mathcal{H}_0^{(n)}\right)} \underset{\mathcal{H}_0^{(n)}}{\overset{\mathcal{H}_1^{(n)}}{\gtrless}} \eta \tag{6.20}$$

By plugging (6.17) and (6.18) into (6.20), the ratio test $\Lambda(\mathbf{x}_n|\mathbf{x}_{\{\bar{N}\}})$ becomes

$$\begin{aligned}\Lambda(\mathbf{x}_n|\mathbf{x}_{\{\bar{N}\}}) &= \frac{e_{\sigma^2_{\mathbf{w}}}\left(\mathbf{x}_n, \mathbf{s}_n\right) \cdot e_{\sigma^2_{\mathbf{w}}}\left(\mathbf{x}_{\{\bar{N}\}}, \mathbf{0}_{L(N-1)}\right)}{e_{\sigma^2_{\mathbf{w}}}\left(\mathbf{x}_n, \mathbf{0}_L\right) \cdot \sum_{\substack{k=0\\k\neq n}}^{N} \rho_{k/\tilde{n}}\ e_{\sigma^2_{\mathbf{w}}}\left(\mathbf{x}_{\{\bar{N}\}}, \mu_k\right)} \\ &= \frac{e_{\sigma^2_{\mathbf{w}}}\left(\mathbf{x}_n, \mathbf{s}_n\right) \cdot e_{\sigma^2_{\mathbf{w}}}\left(\mathbf{x}_{\{\bar{N}\}}, \mathbf{0}_{L(N-1)}\right)}{e_{\sigma^2_{\mathbf{w}}}\left(\mathbf{x}_n, \mathbf{s}_n\right) \cdot e_{\sigma^2_{\mathbf{w}}}\left(\mathbf{x}_{\{\bar{N}\}}, \mathbf{0}_{L(N-1)}\right)} \cdot \frac{\exp\left(\frac{2\Re\{\mathbf{s}_n^H\mathbf{x}_n\}-\mathbf{s}_n^H\mathbf{s}_n}{\sigma^2_{\mathbf{w}}}\right)}{\left[\rho_{0/\tilde{n}} + \sum_{\substack{k=1\\k\neq n}}^{N} \rho_{k/\tilde{n}} \exp\left(\frac{(2\Re\{\mathbf{s}_k^H\mathbf{x}_k\}-\mathbf{s}_k^H\mathbf{s}_k)}{\sigma^2_{\mathbf{w}}}\right)\right]} \\ &= \frac{\exp\left(\frac{2\Re\{\mathbf{s}_n^H\mathbf{x}_n\}-\mathbf{s}_n^H\mathbf{s}_n}{\sigma^2_{\mathbf{w}}}\right)}{\left[\rho_{0/\tilde{n}} + \sum_{\substack{k=1\\k\neq n}}^{N} \rho_{k/\tilde{n}} \exp\left(\frac{(2\Re\{\mathbf{s}_k^H\mathbf{x}_k\}-\mathbf{s}_k^H\mathbf{s}_k)}{\sigma^2_{\mathbf{w}}}\right)\right]}\end{aligned} \tag{6.21}$$

Accordingly, this test is the optimum MAP test given that we know the probabilities $\rho_{k|\tilde{n}}$ and α_n. Assuming the former are known, the latter can be estimated through MLE as discussed in the previous section. By substituting the MLE estimate in (6.21), the attained detector (6.20) is

$$\Lambda^{\text{MAP}}(\mathbf{x}_n|\mathbf{x}_{\{\bar{N}\}}) = \frac{\exp\left(\frac{|\mathbf{s}^H\mathbf{x}_n|^2}{\sigma^2_{\mathbf{w}}}\right)}{\rho_{0/\tilde{n}} + \sum\limits_{\substack{k=1\\k\neq n}}^{N} \rho_{k/\tilde{n}} \exp\left(\frac{|\mathbf{s}^H\mathbf{x}_k|^2}{\sigma^2_{\mathbf{w}}}\right)} \underset{\mathcal{H}_0^{(n)}}{\overset{\mathcal{H}_1^{(n)}}{\gtrless}} \eta \tag{6.22}$$

Note that in (6.22), we have assumed that the noise power $\sigma^2_{\mathbf{w}}$ is known, which is typically estimated using secondary cells in practice. The selection of cells suitable for noise estimation can be further explored in an extended version of this work.

The corresponding ML detector can be obtained by assuming equal probabilities of return at all cells, with $\rho_{k/\tilde{n}}\ \forall k \in \{N\}$, and is given by

$$\Lambda^{\text{ML}}(\mathbf{x}_n|\mathbf{x}_{\{\bar{N}\}}) = \frac{\exp\left(\frac{|\mathbf{s}^H\mathbf{x}_n|^2}{\sigma^2_{\mathbf{w}}}\right)}{\frac{1}{N}\left[1 + \sum_{\substack{k=1\\k\neq n}}^{N} \exp\left(\frac{|\mathbf{s}^H\mathbf{x}_k|^2}{\sigma^2_{\mathbf{w}}}\right)\right]} \underset{\mathcal{H}_0^{(n)}}{\overset{\mathcal{H}_1^{(n)}}{\gtrless}} \eta. \tag{6.23}$$

Accordingly, the resulting tests in (6.22) and (6.23) suggest that the optimal detectors under the full occlusion assumption correspond to the classic test performed at the CUT (6.13), normalized by a weighted sum of the tests from other cells within the same range profile.

6.4 Numerical Analysis

In this section, we evaluate the performance of the proposed detectors on two fronts. Firstly, we model the signal after the angle processing block as input to the detector, employing the full occlusion model presented earlier. We demonstrate the performance of the derived detectors through ROC curves and compare them with the classic detector. Secondly, we simulate a real indoor scenario observed with a FMCW system operating in the mmWave band. This system has multiple transmitting and receiving antennas operating in a TDM scheme, thereby realizing a MIMO radar system. Unlike the model-based case, scenario-based simulations consider the complete standard signal processing chain, starting from the reflected signal and concluding with the detection stage. We then compare the output of the detectors accordingly.

6.4.1 Model-based ROC Assessment

Here, we evaluate the proposed detectors by numerical analysis using Monte Carlo simulations. We demonstrate the performance of these proposed detectors through ROC curves. The detectors are implemented on a set of N test cells, assumed to mutually occlude under a full occlusion scenario. Given this assumption, signal returns are generated so that in each realization, only one out of the N cells contains a target return. The presence or absence of a return at each cell follows a particular signal space probability model, derived from the assumed probability model in the target space, as described in (6.4). Throughout the various Monte Carlo realizations, two sets of signals are generated to represent the null and alternative hypotheses at a predefined CUT. Subsequently, the different detectors are applied, and ROC curves are constructed by sorting the test output relative to each hypothesis and calculating the corresponding probability of false alarm and probability of detection.

To illustrate the signal generation process based on a specific probability model, Figure 6.3 presents an example of probabilities in the target space P_k (a) and signal space ρ_k (b) at each cell, along with the corresponding events of signal returns under the null and alternative hypotheses in (c) and (d), respectively. This is a simplified case for enhanced visualization with a limited number of Monte Carlo runs ($K_{MC} = 10^3$) and a small range profile size of $N = 32$ cells. In this particular example, the probability model for target presence follows a linearly increasing pattern, with the lowest probability assigned to the cell closest to the sensor and the highest to the farthest cell, set at 0.25. Additionally, CUT is arbitrarily selected as cell index $n = 23$, indicated by a cross in (a) and (b), and outlined by a red rectangle in (c) and (d).

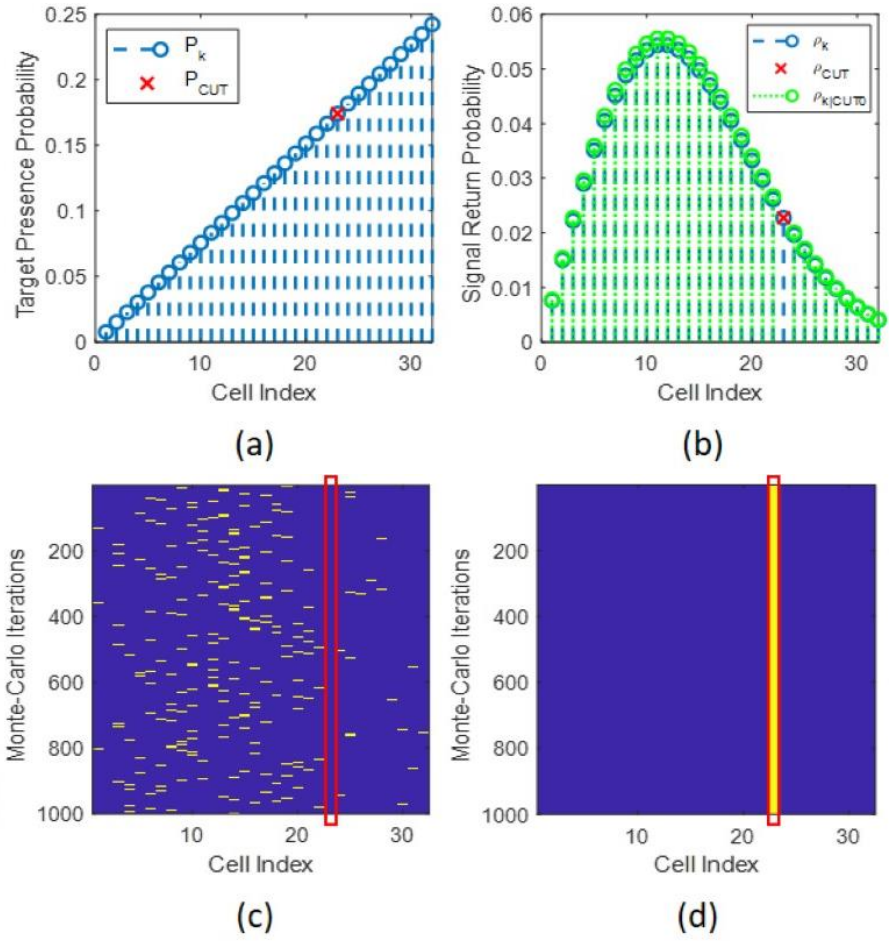

Figure 6.3: Illustration of signal generation in all cells under null and alternative hypotheses for a certain CUT n (highlighted with the red rectangle) given a probability model in the target space for $N = 32$, $n = 23$, $K_{MC} = 10^3$. (a) Probabilities of targets presence P_k, (b) Probabilities of receiving a signal return (marginal ρ_k, and conditioned on no return in CUT $\rho_{k|\tilde{n}}$), (c) Monte-Carlo realizations of signal return events under $\mathcal{H}_0^{(n)}$, (d) Monte-Carlo realizations of signal return events under $\mathcal{H}_1^{(n)}$.

As shown in the figure, the chosen probability model in the target space leads to a higher probability of returns in the signal space for cells located in the middle. In our analysis, we considered two probability models additionally: one with an equal probability of target presence at all cells and another with a linearly decreasing model where the closest cell has the highest probability of target presence. Under each probability model, ranges of the maximum probability of the target's presence in a cell are evaluated.

We evaluate the performance of the MAP and ML detectors derived according to binary and multiple hypothesis testing, presented in equations (6.11), (6.12), (6.22), and (6.23). All our subsequent simulations entail $K_{MC} = 10^8$ Monte Carlo runs for ro-

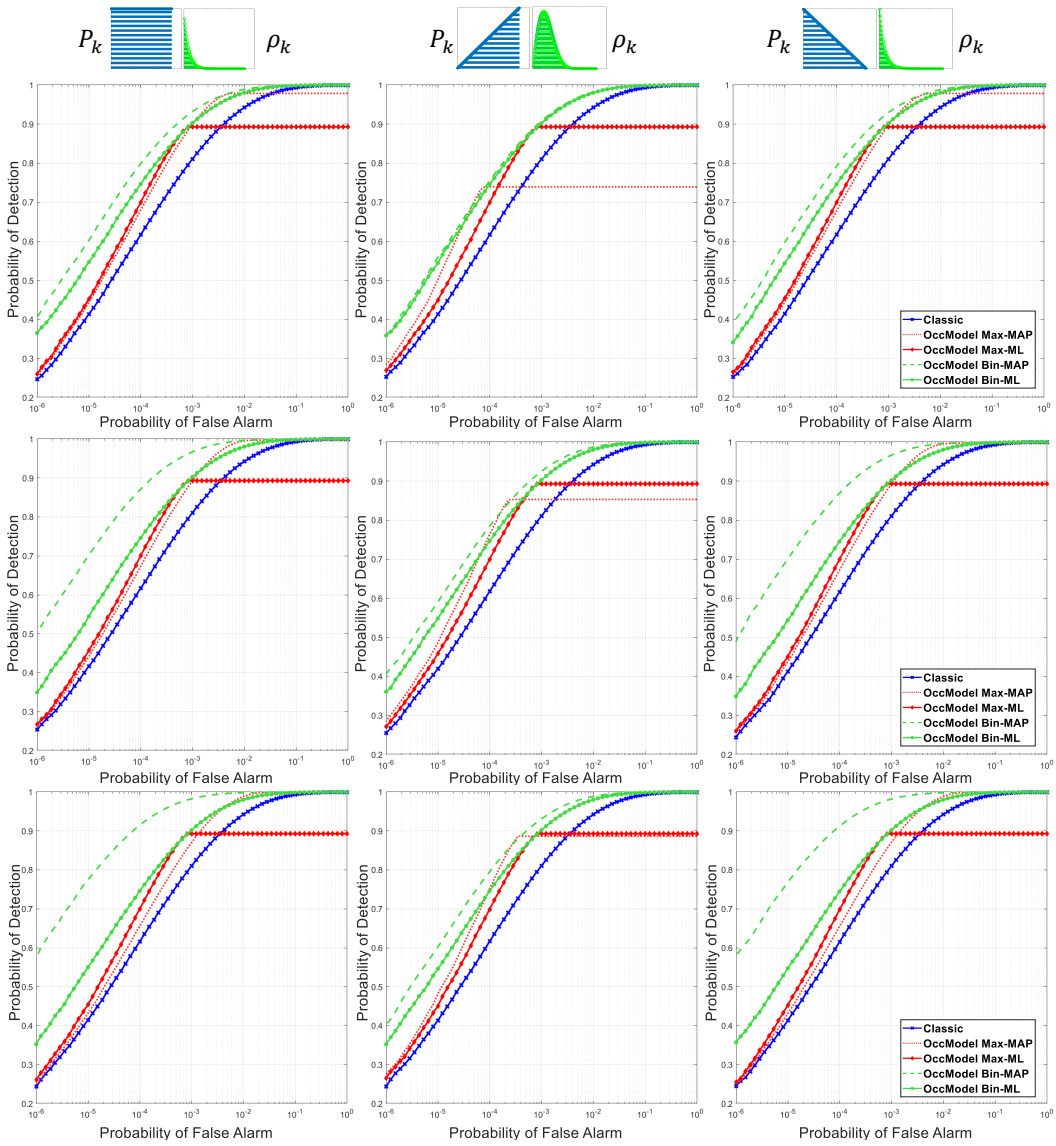

Figure 6.4: ROC curves of proposed detectors compared against classic detector for $N = 128$ cells and SNR $= 10$ dB, for different models of the probability of targets arrival in resolution cells and different values of maximum probability of target presence p_{max} at cells. **Left column:** equal probability, **Middle column:** linearly increasing, **Right column:** linearly decreasing. **Top row:** $p_{max} = 0.1$, **Middle row:** $p_{max} = 0.5$, **Bottom row:** $p_{max} = 0.9$

bust assessment. Comparisons are made against the classic detector (6.14). Figure 6.4 showcases this assessment when a fixed SNR of 10 dB is maintained at the CUT, and for a range profile size of $N = 128$. The columns represent different probability models—equal probabilities, linearly increasing, and decreasing probabilities—while rows denote varying maximum probabilities of target presence in a cell $(P_k)_{\max} = (0.1, 0.5,$ and $0.9)$ from top to bottom. From the figure, several key observations emerge:

- Detectors derived from binary hypothesis formulation under full occlusion consistently outperform the classic detector.
- The MAX detector shows superior detection capability up to a certain probability of false alarm. However, its performance saturates beyond this threshold due to the non-linear maximum operator, particularly noticeable in low SNR scenarios.
- The performance of MAP detectors is scenario-dependent and therefore would lack the Constant False Alarm Rate (CFAR) property.
- MAP detectors demonstrate maximum performance improvement when closer cells have a higher probability of target presence, suggesting a greater likelihood of occlusion for more distant targets.
- While the highest performance gain is provided by binary MAP detectors, the corresponding ML detector still consistently outperforms the classic detector.

Building on the observations mentioned earlier, our subsequent analysis narrows down to the performance evaluation of ML detectors, given their practical applicability. This analysis seeks to assess their performance concerning the size of the range profile N and the SNR levels.

In Figure 6.5, we observe the performance of the detectors across different numbers of mutually occluding cells, specifically $N = 16, 32, 64,$ and 128, assessed at SNR levels of $8, 10,$ and 13 dB. The figure highlights that the detection performance gain is significant with a lower number of occluding cells. Additionally, it demonstrates a decrease in the upper-bound probability of detection for the MAX detector as N increases, especially noticeable at low SNR levels. However, at high SNR levels, the performance gain difference diminishes, with gains of approximately 10% achieved at a false alarm probability of 10^{-6} for an SNR level of 13 dB.

Likewise, Figure 6.6 depicts the detector's performance as SNR varies across different values of N. It becomes evident that the higher the SNR, the more significant the gain of ML detectors compared to the classic one. Moreover, at high SNR values, the MAX

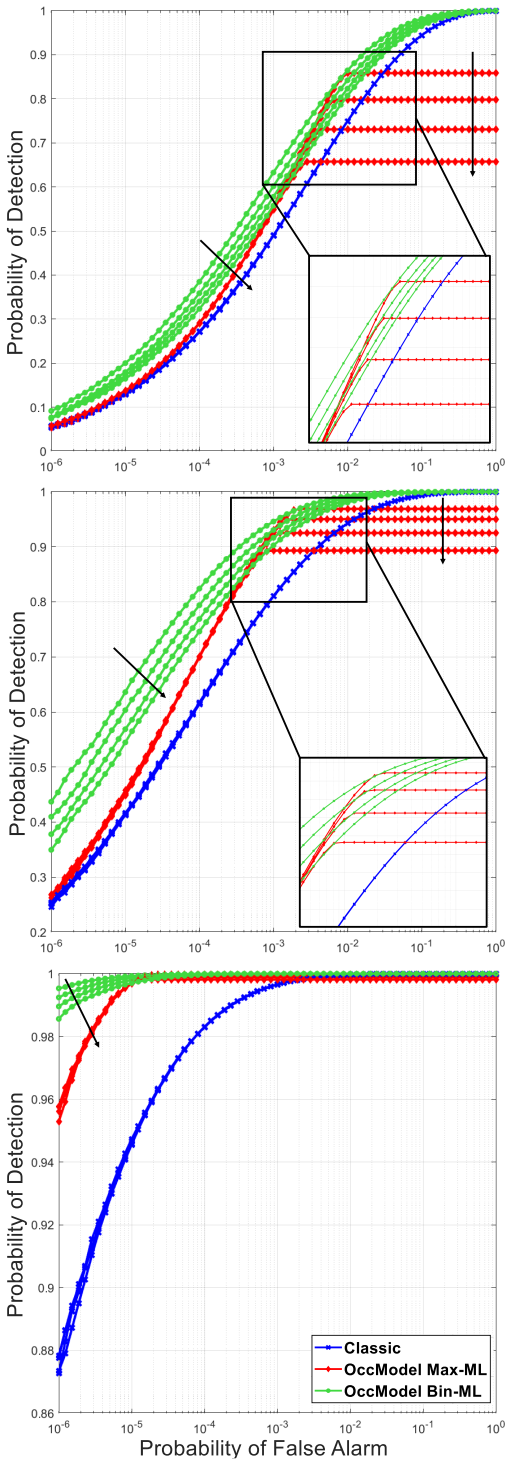

Figure 6.5: ROC curves of proposed ML occlusion-informed detectors compared to classic detector varying the number of mutually occluding cells $N = 16, 32, 64, 128$ (the arrows indicate the direction of increasing N) at different SNR levels. **Top:** 8 dB, **Middle:** 10 dB, **Bottom:** 13 dB.

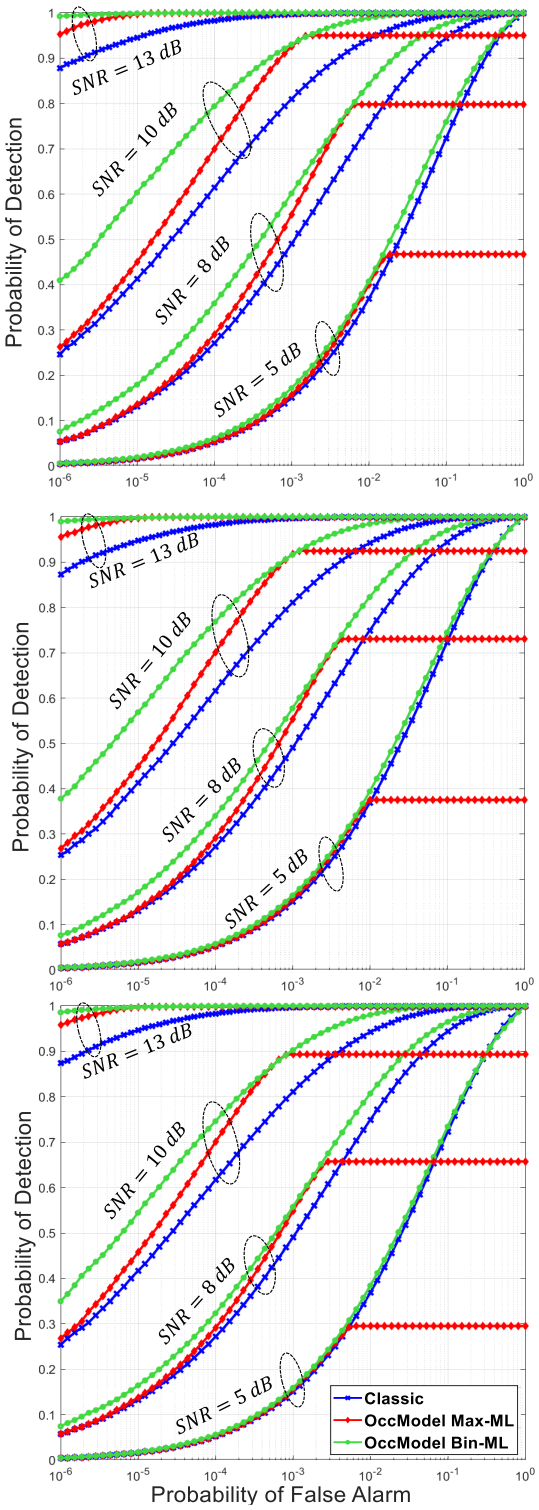

Figure 6.6: ROC curves of proposed ML occlusion-informed detectors compared to classic detector varying SNR at different numbers of mutually occluding cells. **Top:** $N = 32$, **Middle:** $N = 64$, **Bottom:** $N = 128$.

detector achieves a higher detection probability bound, but this decreases significantly at low SNR levels, rendering its use unfeasible.

6.4.2 Scenario-based Simulations

In the previous section, we evaluated detectors' performance based on a defined signal model and specific parameters such as SNR, number of mutually occluding cells, and probability of target presence at individual range cells. This section presents a simulation of a dynamic indoor scenario where multiple human objects move within the scene along predetermined trajectories, resulting in various occlusions, including self-occlusions and inter-object occlusions. We observe this scenario using an FMCW radar sensor equipped with multiple antenna elements for both transmitting and receiving. We generate the radar signal based on a ray-tracing algorithm in tandem with the system parameters. Following this, we process the received signal through a typical radar signal processing chain. After range and angle processing, we apply the classic detector, the detector from (6.23) (abbreviated as ML-Occ), and that from (6.12) (abbreviated as ML-Max), and subsequently compare their performance. In the following subsections, we will elaborate on the modeling of the scenario and targets, the radar signal generation and processing, and finally, the evaluation of the proposed detectors against a classic detector.

Scenario Description and Modelling

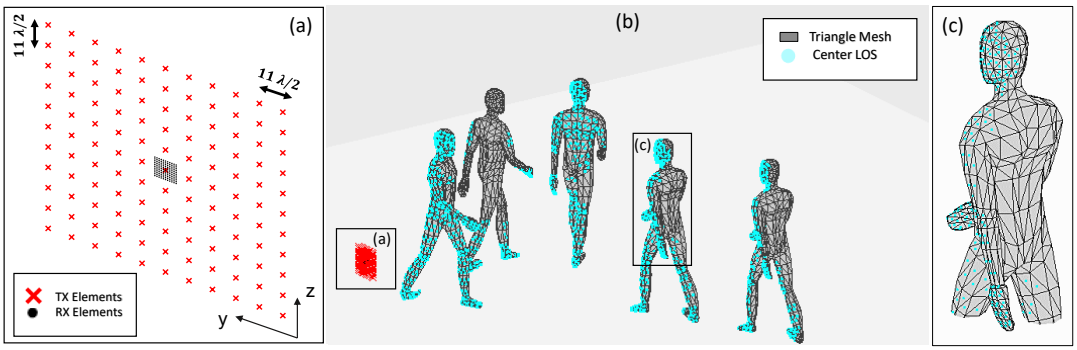

Figure 6.7: Simulation scenario and modeling: (a) Configuration of 121 × 121 TX-RX antennas for the radar sensor, (b) Snapshot of a single time frame of the scenario depicting human targets modeled using triangle batches, highlighting the origin points of triangle batches with LOS, (c) Close-up view of a single human object.

We consider a scenario where five human targets are walking in an indoor environment along different trajectories. The scenario is designed using 3D models of actual-size human objects animated in Blender software [130]. Spanning five seconds at a frame

rate of 20 frames/second, it results in a total of 100 graphical frames. Each 3D model consists of a high-resolution mesh of many constituent triangle batches, resulting in an average triangle surface area of 0.001 m^2. These triangle batches serve as scattering surfaces, defined by an origin vector and two side vectors. Consequently, we utilize a ray-tracing algorithm to identify triangles that have a Line of Sight (LOS) to each transmitting/receiving antenna pair and to quantify the reflected rays. The primary objective of radar ray-tracing is to determine the ray paths from the transmitter to the receiver antenna elements and calculate their amplitude and distance, essential for the generation of the radar signal.

Ray-casting is the fundamental operation employed in ray tracing, involving the calculation of ray-triangle intersections. When a ray intersects a triangle, an intersection point is identified, leading to the generation of new rays for the next bounce. Accordingly, ray tracing starts by assigning rays to each transmit antenna element, calculating intersections with the triangles (if any), and assigning new ray sources for each of the intersection points. Subsequently, the new rays are bounced back in some directions, and a new path is established for the rays that have a LOS intersecting with the receiving antenna.

Consequently, the algorithm outputs a set of rays for each triangle for each transmit and receive antenna pair. The length of each ray represents the relative travel distance of the transmitted electromagnetic wave, reflecting off the target and reaching the receiving antenna element. Meanwhile, the amplitude of the scattered radar wave is determined by the radar equation considering the RCS of the triangle and the corresponding path length to account for attenuation. Ideally, the RCS calculation should account for the number of reflected rays from each triangle, its surface orientation relative to the transmit/receive element pair, and the Normalized RCS [131] given the surface's material. For simplicity, we modeled the RCS of each triangle based on the relative aspect angles (azimuth and elevation) of its normal vector from the origin point, modulating a maximum preset RCS value $\sigma_{\max} = 0.01$ m^2. Figure 6.7 shows a snapshot of a single time frame depicting the human 3D models and the constituent triangle meshes in (b), highlighting the origin points of the triangles with LOS to the antenna configuration of the sensor located at the $y - z$ plane with its center placed at coordinates $(0, 0, 1)$ (a), and a close-up to one of the human objects for enhanced visualization in (c).

Radar Signal Generation

We employ an FMCW MIMO radar sensor operating in a TDM fashion to observe the described scenario. The operating parameters and sensor characteristics for generating

Central Frequency (f_c)	70 (GHz)
Effective Sweeping Bandwidth (BW)	1 (GHz)
Effective Chirp Duration (T_{chirp})	5.124 (µs)
ADC Sampling Frequency (f_s)	2.5 (MHz)
Transmitter Power (p_{Tx})	13 (dBm)
Receiver Noise Figure (F)	12 (dB)
Number of TX Elements (N_{Tx})	121
Number of RX Elements (N_{Rx})	121

Table 6.1: FMCW Radar System Parameters

the radar signal are detailed in Table 6.1. As shown in Figure 6.7. (a), the sensor comprises a 121-element transmitting planar array with an inter-element spacing of $11\lambda/2$, and a 121-element planar receiving array spaced at $\lambda/2$. By assigning each element of the transmitting array to transmit at different time slots, a resulting uniform planar virtual array is achieved leading to an angular resolution of approximately 1.165° in both azimuth and elevation. This low angular resolution promotes cell-level occlusion, thereby encouraging the application of our derived detector as it assumes that each resolution cell encompasses a limited scattering area, resulting in one or few backscattered echoes over a certain range profile.

Accordingly, we simulate the sampled received IF signal (indexed by time samples n_s) at each receiving antenna (n_{RX}), resulting from a backscattered wave due to the signal transmitted by the n_{TX} element, as follows

$$y(n_s, n_{Tx}, n_{Rx}) = \sum_{r=1}^{N_{rays}} A(p_{Tx}, d_r, \sigma_r)[\ \exp(-j2\pi(\mu\tau n_s/f_s + f_c\tau n_s/f_s))\exp(\mathbf{k}(\theta_r, \phi_r)^T(\mathbf{r}_{n_{Tx}} + \mathbf{r}_{n_{Rx}}))\ ]. \tag{6.24}$$

Here, N_{rays} represents the total number of rays traced from the transmitter element to the scene and back to the receiver element. $A(.)$ denotes the amplitude of the scattered wave which depends on the transmitted power p_{TX}, the two-way length of a ray d_r, and the associated triangle RCS σ_r. Additionally, $\mu = BW/T_c$ denotes the slope of the chirp, while $\tau = d_r/c$ is the associated time delay and c is the speed of light in vacuum. Finally, $\mathbf{k}$ is the wave number defined in Section 6.2, θ_r and ϕ_r are the relative azimuth and elevation angles of the normal vector of the surface associated with the traced ray for the sensor, respectively, and $\mathbf{r}_{n_{Tx}}$ and $\mathbf{r}_{n_{Rx}}$ are the coordinate vectors of the transmitting and receiving antenna elements, respectively.

Consequently, for each graphical frame, we have 121×121 channels, each having a

$N_s = T_{chirp} f_s = 128$ time samples. The simulated raw data is then organized in a 2D matrix, with the time samples at the first dimension and the channel data at the second dimension. Lastly, we add the thermal noise to all the channels as a white Gaussian noise with power $p_{noise} = (k_B\ T\ BW\ F)$, where k_B is Boltzmann constant, T is the absolute room temperature, and F is the receiver noise figure.

Radar Signal Processing

Number of Range FFT Bins	256
Number of Azimuth Bins	275
Number of Elevation Bins	121
CA-CFAR PFA (Classic/Max) Detector	10^{-6}
CA-CFAR PFA (OccML) Detector	10^{-7}
CA-CFAR number of training cells	12
CA-CFAR number of guard cells	2

Table 6.2: Radar Signal Processing and Detection Parameters

To process the radar signal, we begin by acquiring the 2D matrix of the raw signal at each frame. We then proceed with a standard signal processing chain, involving range FFT and angle processing using steering vectors. Finally, the detection performance of the three detectors needs to be compared. Initially, we apply the range FFT on the first dimension of the raw data matrix, choosing the grid size to be a power of two that yields a size of half of the range resolution offered by the system's bandwidth.

Subsequently, angle processing is conducted over a Field of View (FOV) of 160° on the azimuth dimension and 70° in elevation. These FOVs were chosen to reduce computational complexity, considering the dimensions of the observed scene. The number of angular bins in azimuth and elevation is similarly set to achieve a grid step size that is half of the angular resolution in both dimensions. Angle processed signal is acquired by multiplying each channel by the corresponding steering vector, as defined in (6.2), for all the angles within the FOVs.

After angle processing, we apply the tests outlined in Section 6.3 to each range profile, along with a classic test simplified to a square-law detector. To determine the threshold corresponding to the desired probability of false alarms, we utilize Cell Averaging (CA)-CFAR to estimate the local noise level at each CUT from neighboring secondary cells. Anticipating superior performance of the OCC-ML detector based on ROC curves from the previous section, we set a lower required Probability of False Alarm (PFA)) for the CFAR applied after this specific test. Table 6.2 summarizes the processing parameters used in the chain.

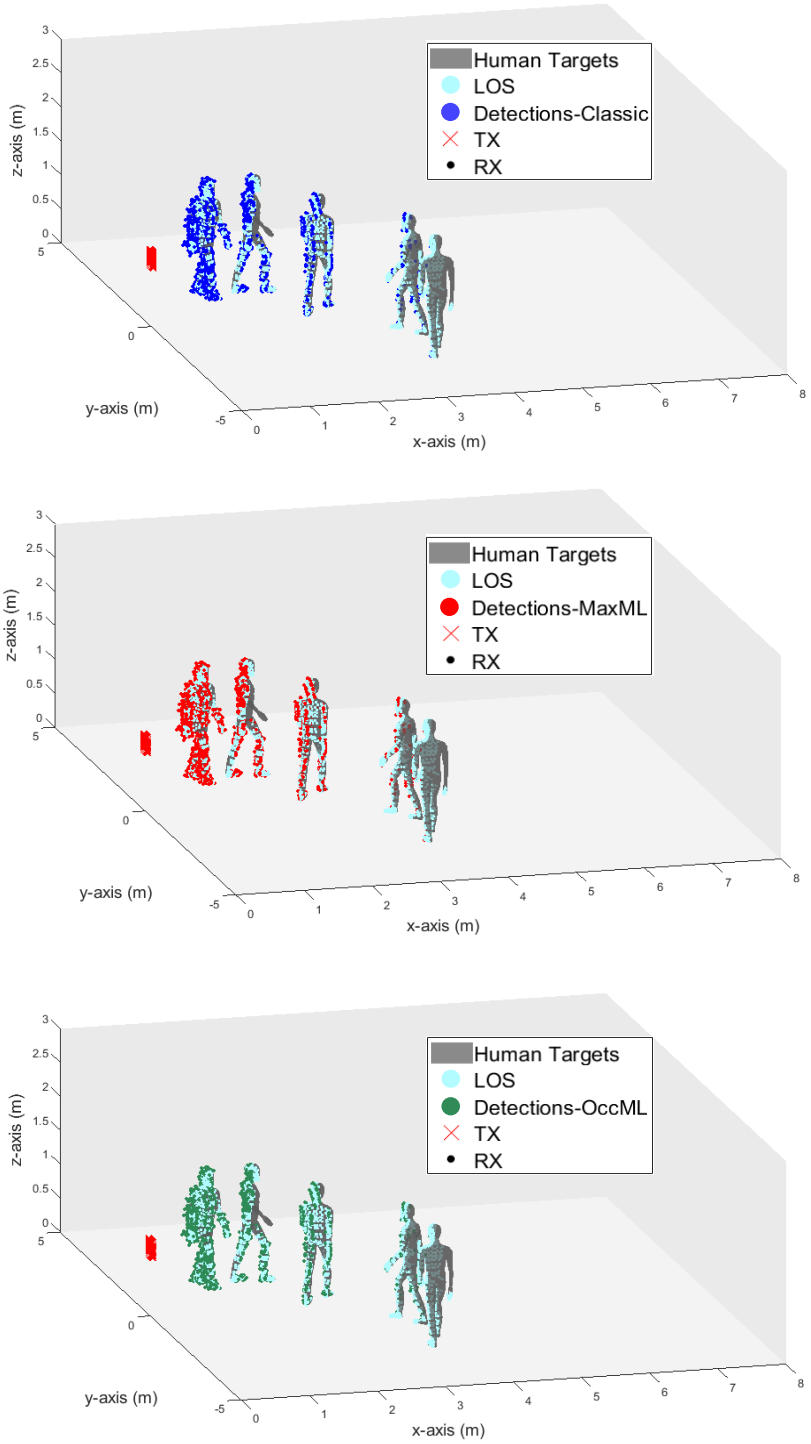

Figure 6.8: Single time frame snapshot of point cloud detection. **Top:** Classic detector output, **Middle:** Max-ML detector output, **Bottom:** Occ-ML detector output.

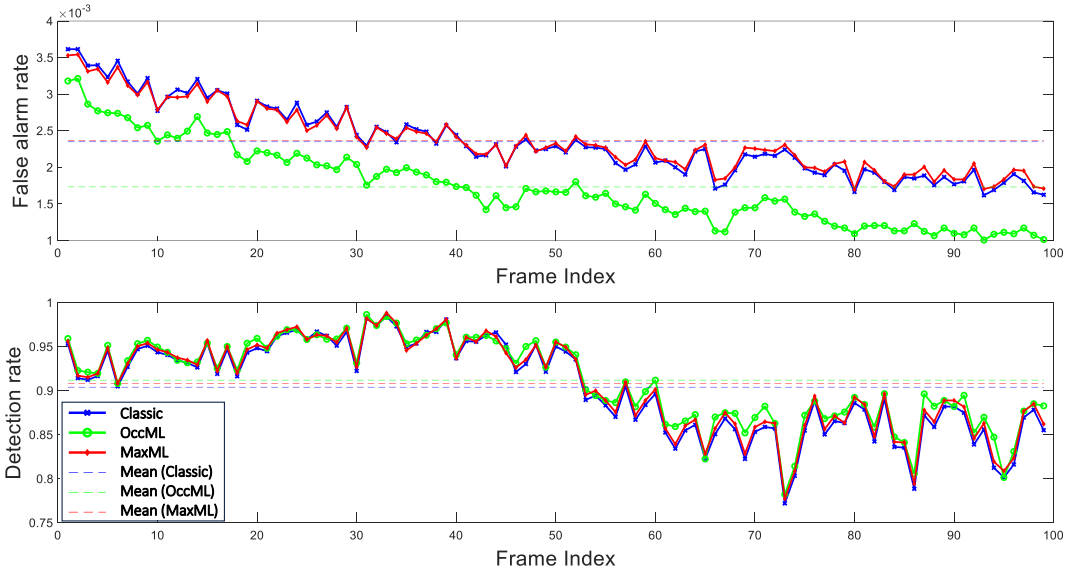

Figure 6.9: Detection performance versus time frames. **Top:** False alarms rate. **Bottom:** Detection rate.

Performance Evaluation

To assess the performance of different implemented detectors, we establish a ground truth grid for each frame. The ground truth grid matches the size of the range-angle grid of the processed signal and has entries of one at the cells that correspond to the location of origin of triangles with LOS rays. Similarly, we construct a grid for each detector, where the locations of detected targets are also marked as one. Subsequently, performance is evaluated by computing the Detection Rate (DR) and False Alarm Rate (FR) using the formulas

$$DR = \frac{TP}{TP + FN}, \qquad FR = \frac{FP}{FP + TN}, \tag{6.25}$$

where TP, FN, FP, and TN represent the counts of true positives, false negatives, false positives, and true negatives, respectively, calculated with respect to the obtained ground truth grid. The values of DR and FR versus frame are illustrated in Figure 6.9.

The figure shows that the detection rate of all three detectors remains nearly equal across all frames, despite the OccML detector being configured to achieve a lower false alarm rate which is achieved consistently. This performance aligns with the analytical analysis presented in Section 6.4.1. It is important to highlight that the analytical model-based simulations were conducted for specific SNR values, demonstrating varying

performance at each value. In contrast, in this realistic scenario-based simulation, each target has a different SNR level that also changes over time, still, the OccML detector exhibits superior performance. On the other hand, the Max detector does not consistently improve detection performance on average. This observation aligns with the findings from the ROC curves presented in the model-based analysis. For certain SNR values and ranges of PFA values, the MaxML detector outperforms the classic detector, whereas for other SNR values and PFA ranges, the opposite holds true. Additionally, even though the assumption of a single echo per range profile might not hold for all range profiles, on average, the proposed OccML detector enhances detection performance.

It is also important to acknowledge that the assessment is based on a single experiment, involving only one noise realization across all channels. Consequently, it may not fully reflect the asymptotic performance obtained through the analytical analysis and illustrated via ROC curves, which considered multiple Monte Carlo realizations. Another limitation arises from the dimensions of the detection grid, which inherently sets a minimum false alarm rate that can be evaluated, higher than the required PFA input to CA-CFAR algorithms. The lower limit of this assessment can be inferred by examining the extremes of the counts in the false alarm rate formula in (6.25).

6.5 Conclusion

In this chapter, we introduced a novel approach to enhance the detection performance of mmWave MIMO sensors with high angular resolution capability, particularly in indoor environments, by leveraging the sparsity of range profiles under full occlusion scenarios. Full occlusion refers to situations where, among multiple targets within a group of mutually occluding cells, the sensor only receives the signal reflected from one target obstructing all others. To achieve this goal, we presented two detection methods based on two distinct formulations: multiple hypothesis testing and binary hypothesis testing. Under both formulations, MAP and ML tests are derived where the former knows the probabilities of target arrivals at the cells, and the latter assumes equal probabilities.

The numerical analysis demonstrated that, for a low required probability of false alarm, all the proposed methods outperformed a classic detector which does not account for this sparse structure, providing a higher probability of detection. However, at higher probabilities of false alarms, especially in low SNR scenarios, detectors derived from our multiple hypotheses formulation exhibited an upper limit on the probability of detection that could not be exceeded. In contrast, detectors based on our binary hypothesis formulation significantly outperformed the classic detector, especially when

knowledge of the probability of target presence in the cells was available. While obtaining such knowledge is often impractical and parameter-dependent, the ML binary detector consistently outperformed the classic detector under all probability models. We further demonstrated the performance of the proposed detectors on realistically simulated data for an indoor scenario where the radar signal is generated using ray tracing and the full standard signal processing chain is implemented.

Chapter 7

Conclusion

In this thesis, we studied the generation of two radar image representations obtainable by a system of distributed mmWave radar sensors, alongside the associated signal processing blocks. Our focus was twofold: first, on jointly creating reflectivity images leveraging CS algorithms, and second, on generating enhanced radar point clouds via statistical detection techniques applied to processed radar signals.

The first part of this thesis introduced algorithms for joint reflectivity image reconstruction, accompanied by methods for accelerating these algorithms and automatically selecting regularization parameters. In the second part, we proposed a detector tailored to accommodate aspect-dependent variations in the RCS of targets observed by distributed sensors. Additionally, we devised a detector that accounts for occlusions induced over individual range profiles, with the aim of enhancing detection performance compared to conventional methods.

This chapter serves to summarize the contributions made in each part, offering a synthesis of the key findings and insights gained. Furthermore, it outlines potential avenues for future research, suggesting ways to extend or deepen the contributions presented in this thesis.

7.1 Summary of Contributions

In Part I, our focus was on developing algorithms for jointly reconstructing a high-resolution global image of a scene observed with distributed sensors, eliminating the need for a fusion step. The joint reconstruction can be achieved through coherent or non-coherent processing of the received signal from all sensors. Apart from the challenges posed by coherent processing (discussed in Section 1.3.1), it is not feasible unless targets exhibit isotropic scattering behavior or are observed over a very small angu-

lar extent. This limitation arises from the non-coherence of target complex reflectivity across sensors.

Accordingly, in Chapter 2, we proposed an algorithm for non-coherent joint reconstruction of global scene images observed by widely distributed radar sensors. This algorithm leverages the ADMM optimization framework. The problem is formulated by imposing a sparsity prior on a defined global image, representing an aggregate view of the scene. Subsequently, we introduced two formulations based on CADMM and SADMM to mathematically define the relationship between individual sensor images and the global image. These formulations yielded two iterative algorithms, adaptable for implementation in a hybrid parallel scheme that harnesses computational power at the sensor and a central processing unit. They offer a trade-off between image quality and processing time, with SADMM demonstrating slower convergence but producing superior image quality, particularly under limited measurements or signal bandwidth.

While these algorithms offer high-quality image reconstruction, they often suffer from slow convergence and long processing times, as expected with iterative algorithms. Consequently, in Chapter 3, we proposed a heuristic method to accelerate the convergence of these algorithms. This method involves learning the support of the image during iterations and focusing the reconstruction on the scene support accordingly. The acceleration method not only reduces processing time but also lowers computational complexity by reducing the problem size over iterations. However, these advantages come with a slight degradation in reconstruction quality, a trade-off that is desirable in many applications.

Throughout Chapters 2 and 3, it has been demonstrated that when employing regularized optimization methods for image reconstruction, an empirical search for the hyperparameters balancing the data-fidelity term and the prior knowledge is often necessary. Accordingly, in the final chapter of Part I, Chapter 4, we introduced a method to automatically tune hyperparameters in image reconstruction methods based on regularized optimization. This method is applicable to reconstruction techniques that utilize scene sparsity as prior knowledge. By leveraging the structure of the back-projection image during the soft thresholding step, which acts as an upper bound for scene sparsity, the method allows for setting regularization parameters according to the desired sparsity level of the scene. Implemented within a FISTA-based algorithm initially proposed for coherent scene imaging with partially synchronized distributed sensors, this approach provides an efficient means to jointly reconstruct the scene image and correct clock mismatch errors. Additionally, we presented an efficient implementation of the algorithm based on FFT, which includes automatic hyperparameter tuning, eliminating the need for empirical parameter searches.

In Part II, we shifted focus to another block of radar signal processing: the detector, with the aim of improving radar point cloud representations. In this part, we did not consider signal processing prior to the detection block. However, we assumed that the processing results in range-angle images, which serve as the input to the detector. Accordingly, targets in the scene are directly modeled as an impulse with appropriate reflectivity in the cell under test corresponding to their location over a range-angle grid map on which the detectors are applied. Our objective was to enhance detection performance and consequently improve the quality of radar point clouds using distributed sensors.

In Chapter 5, we addressed the challenge of detecting aspect-dependent fluctuating targets observed with distributed mmWave radar sensors. Our approach involved jointly considering the processed signals from all sensors to design a GLRT detector that leverages the correlation of the received signal over multiple chirps. By estimating the average received signal power at each sensor, the resulting detector becomes a weighted sum of individual tests at each sensor. These weights are proportional to the local SNR values, which vary significantly due to differences in RCS across various aspect angles and path losses towards each sensor. The derived detector offers improved detection performance compared to directly integrating received signals without prior weighting, as typically done in joint detection.

Lastly, in Chapter 6, we introduced a novel approach to enhance the detection performance of mmWave sensors with high angular resolution capability by leveraging the sparsity of range profiles under full occlusion scenarios over individual range profiles. Full occlusion refers to situations where, among multiple targets within a group of mutually occluding cells, the sensor only receives the signal reflected from one target obstructing all others. Leveraging this structure, we propose two detectors to enhance the detection of non-occluded targets in such scenarios, thereby providing accurate high-resolution point clouds. The first method employs multiple hypothesis testing over each range profile where the range cells within are considered mutually occluding. The second is formulated based on binary hypothesis testing for each cell, considering the distribution of the signal in the other cells within the same range profile. Under both formulations, MAP and ML tests are derived where the former knows the probabilities of target arrivals at the cells, and the latter assumes equal probabilities. Through model-based analysis, we demonstrated the superior detection performance through ROC curves of the proposed detectors over classical detectors not accounting for occlusions over individual range profiles, even when the ML version of the proposed detector is considered. We further demonstrated the performance of the proposed detectors on realistically sim-

ulated data for an indoor scenario where the radar signal is generated using ray tracing, and the full standard signal processing chain is implemented for this simulation.

7.2 Future Work

The various studies presented in this thesis indicate several avenues for extension and further analysis. Below are some areas of investigation and development that can build upon the presented work.

Multistatic Sensors Configuration In most algorithms presented in this thesis, the distributed radar systems follow a mono-static configuration, typically implemented through a TDM scheme. In this scheme, the received signals at each sensor are the echoes reflected off the scene due to its own transmission. While this simplifies the signal model and processing, it does not fully exploit the system's capabilities achievable with bistatic or multistatic configurations. In these configurations, each sensor's received signal results from the reflection of the transmitted signal by all sensors. Consequently, richer information about the illuminated scene can be harnessed.

Exploring Different Priors and Formulations in ADMM Imaging The jointly distributed reconstruction algorithms based on ADMM presented in Chapters 2 and 3 provide a groundwork for similar reconstruction methods. Utilizing the same concept of a single variable representing the global image, other reconstruction methods can be developed to further exploit prior knowledge of the scene such as block sparsity, for example. A direct extension would be employing different priors on the global image and varying constraint formulations that establish relationships between global and local images.

Integration of Aspect-dependent and Occlusion-informed Detectors The detectors proposed in Chapters 5 and 6 were developed independently, with each focusing on modeling different parameters in the hypothesis testing formulation. Integrating both aspect-dependent target behavior and occlusion over range profiles in the formulation of a single detector could lead to performance improvements by leveraging the strengths of both detectors.

Occlusion-Informed Detector Under Partial Occlusions Extending the occlusion-informed detector presented in Chapter 6 to consider partial occlusions, where cells are not fully occupied by targets, would broaden its applicability beyond radar systems

with very high angular resolution. This extension could enhance detection performance without imposing excessive constraints on system parameters.

Analytical Formulation of PFA and Threshold for the Proposed Detectors The performance evaluation of the detectors developed in Part II has primarily relied on numerical assessments, either through ROC analysis using Monte Carlo simulations or within defined dynamic scenarios. This was because deriving an analytical formulation for the PFA and the corresponding threshold under the proposed detectors is not straightforward due to the composite nature of the proposed hypotheses. Nonetheless, an effort to derive or approximate these formulas would offer a more rigorous analysis of the proposed detectors, enabling assessment across various parameters of the scenario boundaries.

Bibliography

[1] S. Pisa, E. Pittella, and E. Piuzzi, "A survey of radar systems for medical applications," *IEEE Aerospace and Electronic Systems Magazine*, vol. 31, no. 11, pp. 64–81, Nov. 2016. [Online]. Available: http://ieeexplore.ieee.org/document/7771668/

[2] A. Singh, S. U. Rehman, S. Yongchareon, and P. H. J. Chong, "Multi-Resident Non-Contact Vital Sign Monitoring Using Radar: A Review," *IEEE Sensors Journal*, vol. 21, no. 4, pp. 4061–4084, Feb. 2021, conference Name: IEEE Sensors Journal. [Online]. Available: https://ieeexplore.ieee.org/document/9249383

[3] M. T. Bevacqua, S. Di Meo, L. Crocco, T. Isernia, and M. Pasian, "Millimeter-Waves Breast Cancer Imaging via Inverse Scattering Techniques," *IEEE Journal of Electromagnetics, RF and Microwaves in Medicine and Biology*, vol. 5, no. 3, pp. 246–253, Sep. 2021, conference Name: IEEE Journal of Electromagnetics, RF and Microwaves in Medicine and Biology. [Online]. Available: https://ieeexplore.ieee.org/document/9325514

[4] Y. Zhao, A. Yarovoy, and F. Fioranelli, "Angle-Insensitive Human Motion and Posture Recognition Based on 4D Imaging Radar and Deep Learning Classifiers," *IEEE Sensors Journal*, vol. 22, no. 12, pp. 12 173–12 182, Jun. 2022. [Online]. Available: https://ieeexplore.ieee.org/document/9775722/

[5] J. Lien, N. Gillian, M. E. Karagozler, P. Amihood, C. Schwesig, E. Olson, H. Raja, and I. Poupyrev, "Soli: ubiquitous gesture sensing with millimeter wave radar," *ACM Transactions on Graphics*, vol. 35, no. 4, pp. 142:1–142:19, Jul. 2016. [Online]. Available: https://dl.acm.org/doi/10.1145/2897824.2925953

[6] Z. Xia, Y. Luomei, C. Zhou, and F. Xu, "Multidimensional Feature Representation and Learning for Robust Hand-Gesture Recognition on Commercial Millimeter-Wave Radar," *IEEE Transactions on Geoscience and*

Remote Sensing, vol. 59, no. 6, pp. 4749–4764, Jun. 2021. [Online]. Available: https://ieeexplore.ieee.org/document/9153890/

[7] B. Gonzalez-Valdes, Y. Alvarez, S. Mantzavinos, C. M. Rappaport, F. Las-Heras, and J. A. Martinez-Lorenzo, "Improving Security Screening: A Comparison of Multistatic Radar Configurations for Human Body Imaging," *IEEE Antennas and Propagation Magazine*, vol. 58, no. 4, pp. 35–47, Aug. 2016. [Online]. Available: http://ieeexplore.ieee.org/document/7494667/

[8] D. Sheen, D. McMakin, and T. Hall, "Three-dimensional millimeter-wave imaging for concealed weapon detection," *IEEE Transactions on Microwave Theory and Techniques*, vol. 49, no. 9, pp. 1581–1592, Sep. 2001, conference Name: IEEE Transactions on Microwave Theory and Techniques. [Online]. Available: https://ieeexplore.ieee.org/document/942570

[9] L. Ding, S. Wu, P. Li, and Y. Zhu, "Millimeter-Wave Sparse Imaging for Concealed Objects Based on Sparse Range Migration Algorithm," *IEEE Sensors Journal*, vol. 19, no. 16, pp. 6721–6728, Aug. 2019, conference Name: IEEE Sensors Journal. [Online]. Available: https://ieeexplore.ieee.org/document/8695109

[10] J. R. Gallion and R. Zoughi, "Millimeter-Wave Imaging of Surface-Breaking Cracks in Steel With Severe Surface Corrosion," *IEEE Transactions on Instrumentation and Measurement*, vol. 66, no. 10, pp. 2789–2791, Oct. 2017. [Online]. Available: http://ieeexplore.ieee.org/document/8017506/

[11] S. Z. Gurbuz and M. G. Amin, "Radar-based human-motion recognition with deep learning: Promising applications for indoor monitoring," *IEEE Signal Processing Magazine*, vol. 36, no. 4, pp. 16–28, 2019.

[12] B. Fu, N. Damer, F. Kirchbuchner, and A. Kuijper, "Sensing Technology for Human Activity Recognition: A Comprehensive Survey," *IEEE Access*, vol. 8, pp. 83 791–83 820, 2020.

[13] M. Zoofaghari, A. Tavakoli, and M. Dehmollaian, "Reconstruction of Concealed Objects in a Corrugated Wall With a Smoothly Varying Roughness Using the Linear Sampling Method," *IEEE Transactions on Geoscience and Remote Sensing*, vol. 54, no. 6, pp. 3589–3598, Jun. 2016. [Online]. Available: http://ieeexplore.ieee.org/document/7412744/

[14] G. Beltrão, R. Stutz, F. Hornberger, W. A. Martins, D. Tatarinov, M. Alaee-Kerahroodi, U. Lindner, L. Stock, E. Kaiser, S. Goedicke-Fritz, U. Schroeder,

B. S. M. R., and M. Zemlin, "Contactless radar-based breathing monitoring of premature infants in the neonatal intensive care unit," *Scientific Reports*, vol. 12, no. 1, p. 5150, Mar. 2022.

[15] *Airport Passenger Screening Using Millimeter Wave Machines: Compliance with Guidelines*. Washington, D.C.: National Academies Press, Jan. 2017. [Online]. Available: https://www.nap.edu/catalog/24936

[16] mmWave radar sensors | TI.com. Accessed: Sep., 13, 2023. [Online]. Available: https://www.ti.com/sensors/mmwave-radar/overview.html

[17] NXP introduces advanced automotive radar one-chip family for next-gen ADAS and autonomous driving systems. Accessed: Sep., 13, 2023. [Online]. Available: https://www.nxp.com/company/about-nxp/nxp-introduces-advanced-automotive-radar-one-chip-family-for-next-gen-adas-and-autonomous-driving-systems:nw-nxp-introduces-advanced-automotive-radar-one

[18] A. Santra, S. Hazra, L. Servadei, T. Stadelmayer, M. Stephan, and A. Dubey, "Signal Processing with Deep Learning," in *Methods and Techniques in Deep Learning: Advancements in mmWave Radar Solutions*. IEEE, 2023, pp. 181–200, conference Name: Methods and Techniques in Deep Learning: Advancements in mmWave Radar Solutions.

[19] M. Amin, *Radar for Indoor Monitoring: Detection, Classification, and Assessment*. CRC Press, 2017.

[20] Y. Meng, C. Lin, J. Zang, A. Qing, and N. K. Nikolova, "General Theory of Holographic Inversion With Linear Frequency Modulation Radar and its Application to Whole-Body Security Scanning," *IEEE Transactions on Microwave Theory and Techniques*, vol. 68, no. 11, pp. 4694–4705, Nov. 2020. [Online]. Available: https://ieeexplore.ieee.org/document/9173695/

[21] M. Markel, *Radar for Fully Autonomous Driving*. Artech House, Apr. 2022.

[22] Z. Xia and F. Xu, "Time-Space Dimension Reduction of Millimeter-Wave Radar Point-Clouds for Smart-Home Hand-Gesture Recognition," *IEEE Sensors Journal*, vol. 22, no. 5, pp. 4425–4437, Mar. 2022.

[23] L. Wang and Y. Huang, "A Survey of 3D Point Cloud and Deep Learning-Based Approaches for Scene Understanding in Autonomous Driving," *IEEE Intelligent*

Transportation Systems Magazine, vol. 14, no. 6, pp. 135–154, Nov. 2022. [Online]. Available: https://ieeexplore.ieee.org/document/9565876/

[24] S. Z. Gürbüz, C. Clemente, A. Balleri, and J. J. Soraghan, "Micro-doppler-based in-home aided and unaided walking recognition with multiple radar and sonar systems," *IET Radar, Sonar and Navigation*, vol. 11, pp. 107–115, 2017. [Online]. Available: https://doi.org/10.1049/iet-rsn.2016.0055

[25] S. Z. Gurbuz and M. G. Amin, "Radar-Based Human-Motion Recognition With Deep Learning: Promising Applications for Indoor Monitoring," *IEEE Signal Processing Magazine*, vol. 36, no. 4, pp. 16–28, Jul. 2019. [Online]. Available: https://ieeexplore.ieee.org/document/8746862/

[26] X. Liu, W. Jiang, S. Chen, X. Xie, H. Liu, Q. Cai, X. Tong, T. Shi, and W. Qu, "PosMonitor: Fine-Grained Sleep Posture Recognition With mmWave Radar," *IEEE Internet of Things Journal*, vol. 11, no. 7, pp. 11 175–11 189, Apr. 2024. [Online]. Available: https://ieeexplore.ieee.org/document/10302282/

[27] B. Bhanu, "Automatic Target Recognition: State of the Art Survey," *IEEE Transactions on Aerospace and Electronic Systems*, vol. AES-22, no. 4, pp. 364–379, Jul. 1986, conference Name: IEEE Transactions on Aerospace and Electronic Systems. [Online]. Available: https://ieeexplore.ieee.org/document/4104226

[28] S. Jacobs and J. O'Sullivan, "Automatic target recognition using sequences of high resolution radar range-profiles," *IEEE Transactions on Aerospace and Electronic Systems*, vol. 36, no. 2, pp. 364–381, Apr. 2000, conference Name: IEEE Transactions on Aerospace and Electronic Systems. [Online]. Available: https://ieeexplore.ieee.org/document/845214

[29] L. Potter and R. Moses, "Attributed scattering centers for SAR ATR," *IEEE Transactions on Image Processing*, vol. 6, no. 1, pp. 79–91, Jan. 1997, conference Name: IEEE Transactions on Image Processing. [Online]. Available: https://ieeexplore.ieee.org/document/552098

[30] G. B. Hammond and J. A. Jackson, "Sar canonical feature extraction using molecule dictionaries," in *2013 IEEE Radar Conference (RadarCon13)*. IEEE, 2013, pp. 1–6.

[31] J. Verly, R. L. Delanoy, and D. E. Dudgeon, "Machine Intelligence Technology for Automatic Target Recognition," *Lincoln Laboratory Journal*, vol. 2,

no. 2, 1989, publisher: Massachusetts Institute of Technology. Lincoln Laboratory, Lexington, United States - Massachusetts. [Online]. Available: https://orbi.uliege.be/handle/2268/108207

[32] Q. Zhao and J. Principe, "Support vector machines for SAR automatic target recognition," *IEEE Transactions on Aerospace and Electronic Systems*, vol. 37, no. 2, pp. 643–654, Apr. 2001, conference Name: IEEE Transactions on Aerospace and Electronic Systems. [Online]. Available: https://ieeexplore.ieee.org/document/937475

[33] A. Krizhevsky, I. Sutskever, and G. E. Hinton, "ImageNet Classification with Deep Convolutional Neural Networks," in *Advances in Neural Information Processing Systems*, vol. 25. Curran Associates, Inc., 2012.

[34] Y. Kim, I. Alnujaim, and D. Oh, "Human Activity Classification Based on Point Clouds Measured by Millimeter Wave MIMO Radar With Deep Recurrent Neural Networks," *IEEE Sensors Journal*, vol. 21, no. 12, pp. 13 522–13 529, Jun. 2021, conference Name: IEEE Sensors Journal.

[35] Z. Yu, A. Taha, W. Taylor, A. Zahid, K. Rajab, H. Heidari, M. A. Imran, and Q. H. Abbasi, "A Radar-Based Human Activity Recognition Using a Novel 3-D Point Cloud Classifier," *IEEE Sensors Journal*, vol. 22, no. 19, pp. 18 218–18 227, Oct. 2022, conference Name: IEEE Sensors Journal.

[36] B. Wang, C. Ding, H. Chen, H. Hong, and X. Zhu, "Radar-based Human Activity Recognition with Range-distributed Time–Doppler Sparse Point Cloud and Multi-Channel PointNet," in *2023 53rd European Microwave Conference (EuMC)*, Sep. 2023, pp. 641–644.

[37] J. Yan, J. Hu, L. Sun, H. Hong, C. Gu, C. Li, and X. Zhu, "Full-Coverage Indoor SAR Imaging with a Vehicle-based FMCW Radar System," in *2018 IEEE/MTT-S International Microwave Symposium - IMS*, Jun. 2018, pp. 135–137, iSSN: 2576-7216.

[38] A. M. Haimovich, R. S. Blum, and L. J. Cimini, "MIMO Radar with Widely Separated Antennas," *IEEE Signal Processing Magazine*, vol. 25, no. 1, pp. 116–129, 2008.

[39] E. Fishler, A. Haimovich, R. Blum, L. Cimini, D. Chizhik, and R. Valenzuela, "Spatial Diversity in Radars—Models and Detection Performance," *IEEE Transactions on Signal Processing*, vol. 54, no. 3, pp. 823–838, Mar. 2006.

[40] R. L. Moses, L. C. Potter, and M. Cetin, "Wide-angle SAR imaging," in *Algorithms for Synthetic Aperture Radar Imagery XI*, vol. 5427. International Society for Optics and Photonics, 2004, pp. 164–175.

[41] T. Aittomaki and V. Koivunen, "Performance of MIMO Radar With Angular Diversity Under Swerling Scattering Models," *IEEE Journal of Selected Topics in Signal Processing*, vol. 4, no. 1, pp. 101–114, Feb. 2010.

[42] V. Chernyak, "Multisite radar systems composed of MIMO radars," *IEEE Aerospace and Electronic Systems Magazine*, vol. 29, no. 12, pp. 28–37, Dec. 2014.

[43] D. Hall and J. Llinas, "An introduction to multisensor data fusion," *Proceedings of the IEEE*, vol. 85, no. 1, pp. 6–23, Jan. 1997, conference Name: Proceedings of the IEEE. [Online]. Available: https://ieeexplore.ieee.org/document/554205

[44] P. K. Varshney, *Distributed Detection and Data Fusion*. New York, NY: Springer New York, 1997.

[45] S. Tebaldini and A. Monti Guarnieri, "On the Role of Phase Stability in SAR Multibaseline Applications," *IEEE Transactions on Geoscience and Remote Sensing*, vol. 48, no. 7, pp. 2953–2966, Jul. 2010.

[46] D. Liu, U. S. Kamilov, and P. T. Boufounos, "Coherent distributed array imaging under unknown position perturbations," *2016 4th International Workshop on Compressed Sensing Theory and its Applications to Radar, Sonar and Remote Sensing, CoSeRa 2016*, pp. 105–109, 2016.

[47] M. A. Lodhi, H. Mansour, and P. Boufounos, "Coherent radar imaging using unsynchronized distributed antennas," in *IEEE International Conference on Acoustics, Speech and Signal Processing (ICASSP)*, 2019, pp. 4320–4324.

[48] A. Murtada, R. Hu, B. S. Maysore Rama Rao, and U. Schroeder, "Widely distributed radar imaging: Unmediated ADMM based approach," *IEEE Journal of Selected Topics in Signal Processing*, vol. 17, no. 2, pp. 389–402, 2023.

[49] R. Hu, B. S. Mysore Rama Rao, A. Murtada, M. Alaee-Kerahroodi, and B. Ottersten, "Widely-distributed radar imaging based on consensus ADMM," in *2021 IEEE Radar Conference (RadarConf21)*, 2021, pp. 1–6, ISSN: 2375-5318.

[50] A. Murtada, R. Hu, M. Alaee-Kerahroodi, U. Schroeder, and B. S. Mysore Rama Rao, "Efficient radar imaging using partially synchronized distributed sensors," in *2021 IEEE Radar Conference (RadarConf21)*, 2021, pp. 1–6.

[51] A. Murtada, B. S. Mysore Rama Rao, R. Hu, and U. Schroeder, "Accelerated Consensus ADMM for Widely Distributed Radar Imaging," in *2022 IEEE Radar Conference (RadarConf22)*, Mar. 2022, pp. 1–6. [Online]. Available: https://ieeexplore.ieee.org/document/9764182

[52] A. Murtada, B. S. Mysore Rama Rao, and U. Schroeder, "Distributed Radar Imaging Based on Accelerated ADMM." arXiv, Jul., 2023 International Symposium on Computational Sensing (ISCS23). [Online]. Available: http://arxiv.org/abs/2307.08606

[53] A. Murtada, B. S. Maysore Rama Rao, and U. Schroeder, "GLRT detector for aspect-dependent fluctuating targets using distributed mmwave MIMO radar sensors," in *2023 31st European Signal Processing Conference (EUSIPCO)*, 2023.

[54] P. Vouras, K. V. Mishra, A. Artusio-Glimpse, S. Pinilla, A. Xenaki, D. W. Griffith, and K. Egiazarian, "An overview of advances in signal processing techniques for classical and quantum wideband synthetic apertures," 2022. [Online]. Available: https://arxiv.org/abs/2205.05602

[55] G. Gennarelli, F. Soldovieri, and M. Amin, "Radar for indoor surveillance: state of art and perspectives," in *Multimodal Sensing: Technologies and Applications*, vol. 11059. International Society for Optics and Photonics, 2019.

[56] H. Mansour, D. Liu, U. Kamilov, and P. Boufounos, "Sparse blind deconvolution for distributed radar autofocus imaging," *IEEE Transactions on Computational Imaging*, vol. 4, pp. 537–551, 2018.

[57] H. Mansour, D. Liu, P. T. Boufounos, and U. S. Kamilov, "Radar autofocus using sparse blind deconvolution," in *IEEE International Conference on Acoustics, Speech and Signal Processing (ICASSP)*. IEEE, 2018, pp. 1623–1627.

[58] J. Ash, E. Ertin, L. C. Potter, and E. Zelnio, "Wide-angle synthetic aperture radar imaging: Models and algorithms for anisotropic scattering," *IEEE Signal Processing Magazine*, vol. 31, no. 4, pp. 16–26, 2014.

[59] L. C. Potter and R. L. Moses, "Attributed scattering centers for sar atr," *IEEE Transactions on Image Processing*, vol. 6, no. 1, pp. 79–91, 1997.

[60] M. Liu, B. Zhang, Z. Xu, and Y. Wu, "Efficient parameter estimation for sparse SAR imaging based on complex image and azimuth-range decouple," *Sensors*, vol. 19, no. 20, p. 4549, 2019.

[61] N. Sugavanam and E. Ertin, "Interrupted SAR imaging with limited persistence scattering models," in *2017 IEEE Radar Conference (RadarConf)*, 2017-05, pp. 1770–1775, ISSN: 2375-5318.

[62] Y. Yang, G. Gui, R. Hu, X. Zhang, X. Cong, and Q. Wan, "Robust polarimetric sar imaging method with attributed scattering characterization," *IEEE Access*, vol. 7, pp. 52 414–52 426, 2019.

[63] R. Hu, R. Min, and Y. Pi, "A video-SAR imaging technique for aspect-dependent scattering in wide angle," *IEEE Sensors Journal*, vol. 17, no. 12, pp. 3677–3688, 2017.

[64] T. Sanders, A. Gelb, and R. B. Platte, "Composite SAR imaging using sequential joint sparsity," *Journal of Computational Physics*, vol. 338, pp. 357–370, 2017.

[65] Z. Wei, L. Yang, Z. Wang, B. Zhang, Y. Lin, and Y. Wu, "Wide angle SAR sub-aperture imaging based on modified compressive sensing," *IEEE Sensors Journal*, vol. 18, no. 13, pp. 5439–5444, 2018.

[66] Z. Xu, M. Liu, G. Zhou, Z. Wei, B. Zhang, and Y. Wu, "An accurate sparse SAR imaging method for enhancing region-based features via nonconvex and TV regularization," *IEEE Journal of Selected Topics in Applied Earth Observations and Remote Sensing*, vol. 14, pp. 350–363, 2021.

[67] J. Ziniel and P. Schniter, "Dynamic Compressive Sensing of Time-Varying Signals Via Approximate Message Passing," *IEEE Transactions on Signal Processing*, vol. 61, no. 21, pp. 5270–5284, Nov. 2013.

[68] N. Vaswani, "LS-CS-Residual (LS-CS): Compressive Sensing on Least Squares Residual," *IEEE Transactions on Signal Processing*, vol. 58, no. 8, pp. 4108–4120, Aug. 2010.

[69] N. Vaswani and J. Zhan, "Recursive Recovery of Sparse Signal Sequences From Compressive Measurements: A Review," *IEEE Transactions on Signal Processing*, vol. 64, no. 13, pp. 3523–3549, Jul. 2016.

[70] Z. Wei, B. Zhang, and Y. Wu, "Accurate wide angle SAR imaging based on LS-CS-residual," *Sensors (Basel, Switzerland)*, vol. 19, no. 3, p. 490, 2019.

[71] T. Scarnati and A. Gelb, "Accurate and Efficient Image Reconstruction from Multiple Measurements of Fourier samples," *Journal of Computational Mathematics*, vol. 5, no. 38, p. 797, Mar. 2021.

[72] S. Boyd, N. Parikh, E. Chu, B. Peleato, and J. Eckstein, "Distributed optimization and statistical learning via the alternating direction method of multipliers," *Foundations and Trends in Machine Learning*, vol. 3, no. 1, pp. 1–122, 2011.

[73] M. V. Afonso, J. M. Bioucas-Dias, and M. A. T. Figueiredo, "Fast image recovery using variable splitting and constrained optimization," *IEEE Transactions on Image Processing*, vol. 19, no. 9, pp. 2345–2356, 2010.

[74] ——, "An augmented lagrangian approach to the constrained optimization formulation of imaging inverse problems," *IEEE Transactions on Image Processing*, vol. 20, no. 3, pp. 681–695, 2011.

[75] H. Guven, A. Gungor, and M. Çetin, "An augmented lagrangian method for complex-valued compressed SAR imaging," *IEEE Transactions on Computational Imaging*, vol. 2, pp. 235–250, 2016.

[76] A. Güngör, M. Çetin, and H. E. Güven, "Autofocused compressive sar imaging based on the alternating direction method of multipliers," in *2017 IEEE Radar Conference (RadarConf)*, 2017, pp. 1573–1576.

[77] K. E. Dungan, C. Austin, J. Nehrbass, and L. C. Potter, "Civilian vehicle radar data domes," in *Algorithms for Synthetic Aperture Radar Imagery XVII*, vol. 7699, 2010, p. 76990P.

[78] D. C. Munson, J. D. O'brien, and W. K. Jenkins, "A tomographic formulation of spotlight-mode synthetic aperture radar," *Proceedings of the IEEE*, vol. 71, no. 8, pp. 917–925, 1983.

[79] H.-T. Tran and L. Lo Monte, "Radar tomography," in *Multidimensional Radar Imaging*, M. Martorella, Ed. Institution of Engineering and Technology, 2019, ch. 5, pp. 141–187. [Online]. Available: https://digital-library.theiet.org/content/books/10.1049

[80] C. V. Jakowatz, D. E. Wahl, P. H. Eichel, D. C. Ghiglia, and P. A. Thompson, *Spotlight-Mode Synthetic Aperture Radar: A Signal Processing Approach.* Boston, MA: Springer US, 1996.

[81] H. Griffiths and C. Baker, "FUNDAMENTALS OF TOMOGRAPHY AND RADAR," in *Advances in Sensing with Security Applications*, J. Byrnes and G. Ostheimer, Eds. Dordrecht: Springer Netherlands, 2006, pp. 171–187.

[82] M. Çetin, Ö. Önhon, and S. Samadi, "Handling phase in sparse reconstruction for SAR: Imaging, autofocusing, and moving targets," in *EUSAR 2012; 9th European Conference on Synthetic Aperture Radar*, 2012, pp. 207–210.

[83] J. R. Shewchuk *et al.*, "An introduction to the conjugate gradient method without the agonizing pain," 1994, publisher: Carnegie-Mellon University. Department of Computer Science.

[84] A. Beck and M. Teboulle, "A fast iterative shrinkage-thresholding algorithm for linear inverse problems," *SIAM journal on imaging sciences*, vol. 2, no. 1, pp. 183–202, 2009.

[85] J. Fessler and B. Sutton, "Nonuniform fast fourier transforms using min-max interpolation," *IEEE Transactions on Signal Processing*, vol. 51, no. 2, pp. 560–574, 2003.

[86] S. Varrette, P. Bouvry, H. Cartiaux, and F. Georgatos, "Management of an academic hpc cluster: The ul experience," in *Proc. of the 2014 Intl. Conf. on High Performance Computing & Simulation (HPCS 2014)*. Bologna, Italy: IEEE, July 2014, pp. 959–967.

[87] J. Li and P. Stoica, "MIMO Radar with colocated antennas," *IEEE Signal Processing Magazine*, no. September, pp. 106–114, 2007.

[88] D. L. Marks, O. Yurduseven, and D. R. Smith, "Fourier Accelerated Multistatic Imaging: A Fast Reconstruction Algorithm for Multiple-Input-Multiple-Output Radar Imaging," *IEEE Access*, vol. 5, pp. 1796–1809, 2017.

[89] G. Gennarelli, F. Soldovieri, and M. Amin, "Radar for indoor surveillance: state of art and perspectives," in *Multimodal Sensing: Technologies and Applications*, vol. 11059. International Society for Optics and Photonics, 2019, p. 1105903.

[90] T. Benoudiba-Campanini, J. Giovannelli, and P. Minvielle, "Sprite: 3-d sparse radar imaging technique," *IEEE Transactions on Computational Imaging*, vol. 6, pp. 1059–1069, 2020.

[91] A. M. Haimovich, R. S. Blum, and L. J. Cimini, "MIMO Radar with widely separated antennas," *IEEE Signal Processing Magazine*, vol. 25, no. January, pp. 116–129, 2008.

[92] D. Liu, U. S. Kamilov, and P. T. Boufounos, "Sparsity-driven distributed array imaging," *2015 IEEE 6th International Workshop on Computational Advances in Multi-Sensor Adaptive Processing, CAMSAP 2015*, pp. 441–444, 2015.

[93] L. C. Potter, E. Ertin, J. T. Parker, and M. Çetin, "Sparsity and compressed sensing in radar imaging," in *Proceedings of the IEEE*, no. 6, 2010, pp. 1006–1020.

[94] J. Yang, T. Jin, C. Xiao, and X. Huang, "Compressed sensing radar imaging: Fundamentals, challenges, and advances," *Sensors (Switzerland)*, vol. 19, no. 14, 2019.

[95] M. A. Lodhi, H. Mansour, and P. T. Boufounos, "Coherent Radar Imaging Using Unsynchronized Distributed Antennas," in *ICASSP, IEEE International Conference on Acoustics, Speech and Signal Processing - Proceedings.* IEEE, 2019, pp. 4320–4324.

[96] G. Wang and K. V. Mishra, "Performance Bounds for Displaced Sensor Automotive Radar Imaging," in *ICASSP, IEEE International Conference on Acoustics, Speech and Signal Processing - Proceedings*, vol. 2020-May. IEEE, 2020, pp. 8624–8628.

[97] H. Mansour, D. Liu, U. S. Kamilov, and P. T. Boufounos, "Sparse Blind Deconvolution for Distributed Radar Autofocus Imaging," *IEEE Transactions on Computational Imaging*, vol. 4, no. 4, pp. 537–551, 2018.

[98] H. Mansour, D. Liu, P. T. Boufounos, and U. S. Kamilov, "Radar autofocus using sparse blind deconvolution," *ICASSP, IEEE International Conference on Acoustics, Speech and Signal Processing - Proceedings*, vol. 2018-April, pp. 1623–1627, 2018.

[99] Y. Kim and T. Moon, "Human Detection and Activity Classification Based on Micro-Doppler Signatures Using Deep Convolutional Neural Networks," *IEEE Geoscience and Remote Sensing Letters*, vol. 13, no. 1, pp. 8–12, Jan. 2016.

[100] H. Cui and N. Dahnoun, "High Precision Human Detection and Tracking Using Millimeter-Wave Radars," *IEEE Aerospace and Electronic Systems Magazine*, vol. 36, no. 1, pp. 22–32, Jan. 2021.

[101] B. K. Chalise, D. M. Wong, M. G. Amin, A. F. Martone, and B. H. Kirk, "Detection, mode selection, and parameter estimation in distributed radar networks

: Algorithms and implementation challenges," *IEEE Aerospace and Electronic Systems Magazine*, pp. 1–16, 2022.

[102] E. D'Addio, A. Farina, E. Conte, and M. Longo, "Multistatic detection of radar signals for swerling models of the target," in *Optimized RADAR Processors*, A. Farina, Ed. Peter Peregrinus Ltd., 1987, pp. 143–149.

[103] E. D'Addio and A. Farina, "Overview of detection theory in multistatic radar," *IEE Proceedings F (Communications, Radar and Signal Processing)*, vol. 133, pp. 613–623(10), December 1986. [Online]. Available: https://digital-library.theiet.org/content/journals/10.1049/ip-f-1.1986.0098

[104] V. Aloisio, "Optimum detection of moderately fluctuating radar targets," *IEE Proceedings - Radar, Sonar and Navigation*, vol. 141, no. 3, p. 164, 1994.

[105] J. V. DiFranco and W. L. Rubin, *Radar Detection*. Raleigh, NC: SciTech Publishing, Apr. 2004.

[106] "IWR6843 data sheet, product information and support | TI.com."

[107] B. Erol, M. G. Amin, and B. Boashash, "Range-doppler radar sensor fusion for fall detection," in *2017 IEEE Radar Conference (RadarConf)*, 2017, pp. 0819–0824.

[108] A. Bourdoux, U. Ahmad, D. Guermandi, S. Brebels, A. Dewilde, and W. Van Thillo, "PMCW waveform and MIMO technique for a 79 GHz CMOS automotive radar," in *2016 IEEE Radar Conference (RadarConf)*, 2016, pp. 1–5.

[109] E. Raei, M. Alaee-Kerahroodi, P. Babu, and M. R. B. Shankar, "Generalized waveform design for sidelobe reduction in mimo radar systems," *Signal Processing*, vol. 206, p. 108914, 2023. [Online]. Available: https://doi.org/10.1016/j.sigpro.2022.108914

[110] M. Alaee-Kerahroodi, P. Babu, M. Soltanalian, and B. S. Maysore Rama Rao, *Signal Design for Modern Radar Systems*. Artech House, 2022.

[111] N. K. Sichani, M. Alaee-Kerahroodi, B. S. Maysore Rama Rao, E. Mehrshahi, and S. A. Ghorashi, "Antenna array and waveform design for 4d-imaging mmwave mimo radar sensors," *IEEE Transactions on Aerospace and Electronic Systems*, pp. 1–16, 2023.

[112] Z. Yang, P. H. Pathak, Y. Zeng, X. Liran, and P. Mohapatra, "Vital sign and sleep monitoring using millimeter wave," *ACM Transactions on Sensor Networks*, vol. 13, no. 2, pp. 14:1–14:32, 2017.

[113] M. Shen, K.-L. Tsui, M. A. Nussbaum, S. Kim, and F. Lure, "An indoor fall monitoring system: Robust, multistatic radar sensing and explainable, feature-resonated deep neural network," *IEEE Journal of Biomedical and Health Informatics*, vol. 27, no. 4, pp. 1891–1902, 2023.

[114] J. Pegoraro and M. Rossi, "Real-time people tracking and identification from sparse mm-wave radar point-clouds," *IEEE Access*, vol. 9, pp. 78 504–78 520, 2021.

[115] A. Palffy, J. F. P. Kooij, and D. M. Gavrila, "Detecting darting out pedestrians with occlusion aware sensor fusion of radar and stereo camera," *IEEE Transactions on Intelligent Vehicles*, vol. 8, no. 2, pp. 1459–1472, 2023.

[116] S. K. Kwon, E. Hyun, J.-H. Lee, J. Lee, and S. H. Son, "Detection scheme for a partially occluded pedestrian based on occluded depth in lidar–radar sensor fusion," *Optical Engineering*, vol. 56, no. 11, pp. 113 112–, 2017.

[117] M. Ahmadi, M. Alaee-Kerahroodi, B. S. Maysore Rama Rao, and B. Ottersten, "Subspace-based detector for distributed mmwave mimo radar sensors," in *2023 IEEE International Conference on Acoustics, Speech and Signal Processing (ICASSP)*, 2023, pp. 1–5.

[118] M. Canil, J. Pegoraro, A. Shastri, P. Casari, and M. Rossi, "ORACLE: Occlusion-resilient and self-calibrating mmwave radar network for people tracking," *IEEE Sensors Journal*, vol. 24, no. 3, pp. 3157–3171, 2024.

[119] A. Shastri, M. Canil, J. Pegoraro, P. Casari, and M. Rossi, "mmSCALE: Self-calibration of mmWave radar networks from human movement trajectories," in *2022 IEEE Radar Conference (RadarConf22)*, 2022, pp. 1–6.

[120] T. Yang, J. Cao, and Y. Guo, "Placement selection of millimeter wave FMCW radar for indoor fall detection," in *2018 IEEE MTT-S International Wireless Symposium (IWS)*, 2018, pp. 1–3.

[121] D. Liu, U. S. Kamilov, and P. T. Boufounos, "Sparsity-driven distributed array imaging," in *2015 IEEE 6th International Workshop on Computational Advances in Multi-Sensor Adaptive Processing (CAMSAP)*, 2015, pp. 441–444.

[122] V. H. Tang, A. Bouzerdoum, and S. L. Phung, "Compressive radar imaging of stationary indoor targets with low-rank plus jointly sparse and total variation regularizations," *IEEE Transactions on Image Processing*, vol. 29, pp. 4598–4613, 2020.

[123] T. Benoudiba-Campanini, J.-F. Giovannelli, and P. Minvielle, "Sprite: 3-d sparse radar imaging technique," *IEEE Transactions on Computational Imaging*, vol. 6, pp. 1059–1069, 2020.

[124] R. Hu, B. S. Maysore Rama Rao, A. Murtada, M. Alaee-Kerahroodi, and B. Ottersten, "Widely-distributed radar imaging based on consensus ADMM," in *2021 IEEE Radar Conference (RadarConf21)*, 2021, pp. 1–6.

[125] D. Kozlov and P. Ott, "Cfar detector for compressed sensing radar based on l1-norm minimisation," in *2020 28th European Signal Processing Conference (EUSIPCO)*, 2021, pp. 2050–2054.

[126] C. A. Rogers and D. C. Popescu, "Compressed sensing mimo radar system for extended target detection," *IEEE Systems Journal*, vol. 15, no. 1, pp. 1381–1389, 2021.

[127] J. Ding, M. Wang, H. Kang, and Z. Wang, "Mimo radar super-resolution imaging based on reconstruction of the measurement matrix of compressed sensing," *IEEE Geoscience and Remote Sensing Letters*, vol. 19, pp. 1–5, 2022.

[128] M. Jafri, S. Srivastava, S. Anwer, and A. K. Jagannatham, "Sparse parameter estimation and imaging in mmwave mimo radar systems with multiple stationary and mobile targets," *IEEE Access*, vol. 10, pp. 132 836–132 852, 2022.

[129] R. G. Gallager, *Stochastic Processes: Theory for Applications*, 1st ed. Cambridge University Press, 2013.

[130] blender (3.6 LTS), blender foundation. Accessed: Feb., 11, 2024. [Online]. Available: https://www.blender.org/download/

[131] C. Schüßler, M. Hoffmann, J. Bräunig, I. Ullmann, R. Ebelt, and M. Vossiek, "A realistic radar ray tracing simulator for large mimo-arrays in automotive environments," *IEEE Journal of Microwaves*, vol. 1, no. 4, pp. 962–974, 2021.